RICE UNIVERSITY

FUNCTIONALIZED NANOPARTICLES FOR BIOMEDICAL APPLICATIONS

by

ERIKA L. BRYANT

A THESIS SUBMITTED IN PARTIAL FULFILLMENT OF THE REQUIREMENTS FOR THE DEGREE

DOCTOR OF PHILOSOPY

APPROVED, THESIS COMMITTEE:

_____

Dr. W. E. Billups, Chair
Professor of Chemistry

_____

Dr. Robert H. Hauge
Professor of Chemistry

_____

Dr. Matteo Pasquali
Professor of Chemical &
Biomolecular Engineering

Houston, Texas
April 2013

ABSTRACT

Functionalization of nanoparticles often control the extent of their usage. With this in mind, I have explored methods of creating highly functionalized exfoliated graphite, by way of the Billups-Birch reduction, that can be used in the advancement of nanotechnology (i.e. biomedicine). The method explored the use of sodium as the source for the solvated electron. The results of this method produced exfoliated graphite the same size as graphene and with solubility similar to the substrates attached to it. It was further shown that functionalized graphite with a terminal carboxyl group allowed further synthesis to occur via an elimination-addition reaction after the acyl group was transformed into an acid chloride. This reaction makes it possible to create exfoliated graphite that contains any compound of interest as long as it has an oxygen or nitrogen group that is able to react with the acid chloride. Thus, these products have the potential to be used in biomedicine as drug delivery agents.

Acknowledgements

The creation of a body of work this large is an undertaking that includes numerous people. Their emotional, spiritual, physical and financial support has contributed to me reaching this point. It is hard for me to quantify the amount of help people have given me, because at that point in time, the help they gave is what I needed and I might not have reached this point without it. However, there are a group of people, that without their help, I would not be graduating. To these people I give my wholehearted thanks and understanding.

The names listed below are not in order of importance.

My Wholehearted Thanks

The Almighty
W. E. Billups, Ph. D.
Karen Bryant, D. D. S.
Robert H. Hauge, Ph. D.
John S. Hutchinson, Ph. D.
Jennifer Jamison, Ph. D.
Seiichi Matsuda, Ph. D.
Matteo Pasquali, Ph. D.
Merlyn Pulikkathara, Ph. D.
Aaron Yang, Ph. D.
AGEP

Thank You

Noe Alvarez, Ph. D.
Pedro J. Alvarez, Ph. D.
Rick Barrera, Ph. D.
Bonnie Bartel, Ph. D.
Billups Group Members
Marvin Bryant
CBEN
Theresa Chatman
Bo Chen, Ph. D.
Colvin Group Members
V. L. Colvin, Ph. D.
Naomi Duval
My Family
Blanca E. Flores
My Friends
Wenhua Guo, Ph. D.
Zerrie Hines, J. D.
Palestine Hines
Qilin Li, Ph. D.
Michael Liga
Shaily Mahendra, Ph. D.
J. T. Mayo, Ph. D.
Mary McHale, Ph. D.
Carolyn Nichol, Ph. D.
Ivana Peralta, Ph. D.
Hema Puppla
Sybil J. Rollins
Richard Tapia, Ph. D.
Nicole Wilson
William Yu, Ph. D.

TABLE OF CONTENTS

LIST OF FIGURES

LIST OF SCHEMES

LIST OF TABLES

CHAPTER 1. INTRODUCTION TO FUNCTIONALIZED NANOPARTICLES FOR BIOMEDICAL APPLICATIONS

Health is an issue that concerns all people. We are concerned with finding ways to live a long and healthy life, which can be seen in the increase of the average person's lifespan since the early 1900's (U. S. Social Security Admin. 2012). One way that people look to enhance their life is with the field of medicine. Because of growing interest in the medical field, there is an ongoing drive to improve our understanding of disease. If we are able to prevent, detect, diagnose, and treat disease, we will be able to achieve the life span that most people expect. There are procedures in place to detect, diagnose, monitor, and treat disease that our knowledge base allowed us to create, but as our understanding increases, we must modify these procedures to reflect that knowledge. Consequently, one area our knowledge base is increasing is in the area of nanoparticles.

1.1 Nanoparticles for the prevention of disease

As our understanding of nanoparticles increases we find ways that nanoparticles are useful in biomedicine. The diversity of nanoparticles is such that they are useful in the prevention, determination and treatment of disease. One of the best ways nanoparticles promote health is to maintain it. Silver nanoparticles, for example, are useful in preventing infection from occurring because of their antimicrobial properties. Due to its known antimicrobial properties, silver nanoparticles have been used in air purifiers, refrigerators, and food storage containers (to name a few) to help control the spread of bacteria (Silver Institute 2012). However, research has shown that combining

silver with titanium dioxide, which creates reactive oxygen species, forms a product that increases the efficiency of silver in killing microbes and titanium dioxide in killing viruses, as seen in Appendix 1¸ (Liga, Bryant *et al.* 2011). The increase in activity of silver coated titanium dioxide has led to researching implants coated with silver in order to decrease the risk of infection associated with hard tissue replacement (Visai, De Nardo *et al.*; Vasilev, Cook *et al.* 2009; Zhang, Zhang *et al.* 2012). By utilizing properties of nanoparticles, technology has been created that prevents disease.

1.2 Nanoparticles used to detect, diagnose and treat disease

If health cannot be maintained, then we must be able to detect, diagnose and treat disease. Nanoparticles are useful for these purposes because of their properties and size. The size of nanoparticles is important because it allows for clearance from the kidney and reticuloendothelial system (if between 10 - 100 nm), and it allows contact between the nanoparticle and the biological entity of interest (Pankhurst, Connolly *et al.* 2003; NanoSight 2012). For example, iron oxide is useful *in vivo* and *in vitro* applications, leading to the production of size appropriate and water soluble nanoparticles, as seen in Appendix 3 and 4 (Jing, Zhang *et al.* 2012; Prakash, Zhu *et al.* 2009). It is suitable for cellular labeling, detoxification of biological fluids, tissue repair, drug delivery, magnetic resonance imaging, and hyperthermia treatment. This is possible because of its superparamagnetic properties which enable it to interact with an external magnetic field, that then enables placement of the nanoparticle or allows it to resonantly respond to the field which allows the particle to heat up (Pankhurst, Connolly *et al.* 2003; Tartaj, Morales *et al.* 2003; Gupta and Gupta 2005; Mohapatra and Anand 2010). There is an

array of nanoparticles to choose from for biomedical applications. For example, gold displays potential in biomedicine for use in cancer therapy serving as a detector of protein and DNA, and as a drug delivery agent. Gold is useful because it has a very low reactivity and is biocompatible. Reports have found that gold nanoparticles lead to modification of protein structure. These observations are not fully understood; however, it is thought to hold potential importance in the context of nano-biomedicine and other therapeutic applications; an example of these observations are seen in Appendix 2 (Zhang, Neumann *et al.* 2009; Jamison, Bryant *et al.* 2011). Utilizing these and other nanoparticles, the ability to prevent, detect, diagnose, and treat disease has increased, through biomedical technology, from 50 years ago.

1.3 Nanoparticles modified for biomedical purposes

The use of graphite in the biomedical arena began with the process of creating graphite nanoplatelets or graphene. Graphene's use in biomedicine began in 2008 when Liu *et al.* showed that it is an efficient nanocarrier for drug delivery (Liu, Robinson *et al.* 2008). Since then, it has been shown that it can be used in a variety of biomedical applications, such as biological sensing and imaging. In addition to the current biomedical understanding of graphene, my research focuses on chemically functionalizing graphite for the purpose of exfoliation into graphene sheets to be potentially used in the toolbox of nano pharmacotherapeutics. Chapter 2 in this dissertation investigates the use of the Billups-Birch Reduction, which results in graphene sized exfoliated graphite whose surface is modified with different length alkanes. In addition to the modification of graphite, an addition-elimination reaction is used to attach

two moieties of different functional groups to the exfoliated graphite modified with a carboxylic group. Chapter 3 will provide detailed information on this approach. This approach provides a way to attach a wide variety of compounds to the exfoliated graphite, which expands its uses in biomedicine.

Appendix 1 is a paper titled "Virus inactivation by silver doped titanium dioxide nanoparticles for drinking water treatment." The paper has been published in Water Research (2011, 45(2), 535-54445). My contribution to this work included: selecting the particles for synthesis, synthesizing the particles and characterization of the particles via TEM, XPS, UV-Vis, and ICP-OES. Michael V. Liga tested the capability of inactivating Bacteriophage MS2 in aqueous media. We found that the MS2 inactivation rate increased by more than 5 fold and the inactivation efficiency increased with increasing silver content. This increase in efficiency has the potential to better the technology used in photocatalytic inactivation of viruses and other microorganisms.

Appendix 2 is a paper titled "Altering protein surface charge with chemical modification modulates protein–gold nanoparticle aggregation" which has been published in Journal of Nanoparticle Research (2011, 13(2), 625-636). My contribution to this work consisted of characterizing the gold nanoparticles and the coupled gold nanoparticles and protein by TEM to determine aggregation and size, perform statistical analysis with Image-Pro Plus 5.0 and use of a dynamic light scatterer to determine the hydrodynamic size of the aggregates. This paper explores regulation of protein-gold nanoparticle assembly by modifying the protein surface. We found that protein modification can be used for modulating whether nanoparticle-protein interactions result in aggregation.

Appendix 3 is a manuscript titled "One-step reverse precipitation synthesis of water-dispersible superparamagnetic magnetite nanoparticles" which has been published in the Journal of Nanoparticle Research (2012, 14, 4, 827). My contribution to the work included characterization of the nanoparticles with TEM. This paper reports a one-step method of synthesizing water dispersible, biocompatible and superparamagnetic magnetite nanoparticles. The suspension of nanoparticles in aqueous solution is important for biomedical applications, thus making these nanoparticles an important step in the path of everyday use of nanoparticles in the medical field.

Appendix 4 is a manuscript, "Bilayers as Phase Transfer Agents for Nanocrystals Prepared in Nonpolar Solvents," that has been published in ACS Nano (2009, 3(8), 2139-2146). My contribution to this work was cryo-TEM images of the nanoparticles which were discussed. This paper proved that lipid bilayers can be used to create stable aqueous dispersions with minimal exchange between free and bound surface agents, which result in little residual free organic carbon in the solution. The bilayer-nanocrystal complexes have many of the same size-dependent features as the original materials. Using lipids to increase nanoparticles solubility in water provide new paths for exploring the interface between nanoparticles and biology.

Appendix 5 is a body of work that was written as a literature review of the role nanocarriers play in breast cancer. My contribution to the work was providing references and contributing to the writing of the paper. The paper discusses the origins of breast cancer, how nanoparticles may be used to deliver drugs to treat the disease, and how nanoparticles are used to image the affected area. This work is not published.

CHAPTER 2. CHEMICAL MODIFICATION OF GRAPHITE BY REDUCTION ALKYLATION

2.1 Introduction

Graphite is a semi-metal and the most stable allotrope of carbon; it consists of connected 6 member aromatic rings (Cotton, Wilkinson *et al.* 1999). It comes in two crystal structures, hexagonal and rhombohedral (a less stable form). The forms of graphite differ by the ordering of its graphene layers, which are arranged in a hexagonal pattern (see Figure 1 below).

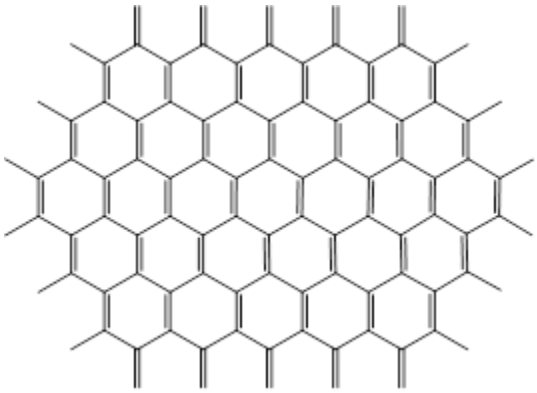

Figure 1. Graphite

The stacking of hexagonal is ABAB and ABCABC for the rhombohedral structure. As Figure 2 indicates, the hexagonal and rhombohedral structures share the same carbon layer spacing and the a-axis parameters (Cotton, 1999; Chung, 2002). The form of graphite that this dissertation will discuss is hexagonal.

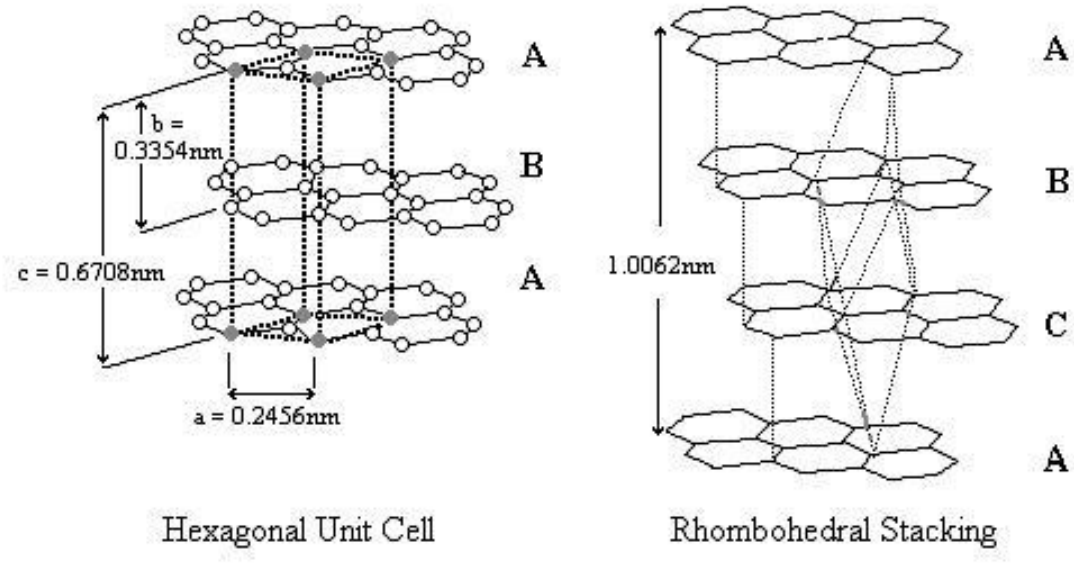

Figure 2. These images show the stacking of the layers, the unit cell and the spacing involved (Fletcher 2008).

The atoms within each layer of graphite are bonded by covalent bonds and the layers are bonded by metallic bonds. The bonding between layers occurs due to van der Waals interactions, produced by the delocalized π-orbitals. The π and σ bonds are associated with 16 energy bands (12 for σ and 4 for π), with only 8 filled. For hexagonal graphite, the energy band separating the 2 groups of 6 σ bands are separated by ~ 5eV. The π bands lie between the two groups of σ bands. All of the energy bands are coupled and the 4 π bands are strongly coupled. Graphite's Fermi level lies in the middle of the coupled π bands, which causes pockets of holes and electrons to occur (Cotton, Wilkinson *et al.* 1999; Chung 2002). Graphite's combination of metallic and covalent bonds result in graphite having diverse properties.

The distance between graphite layers (3.35 Å) is approximately equal to the sum of van der Waals radii; this indicates that the forces between layers are small. This minimum force allows for easy slippage between layers thus attributing to graphite's

softness and lubricity (Cotton, Wilkinson *et al.* 1999; Chung 2002). This in plane metallic bonding also makes graphite a good thermal conductor (Chung 2002). It has a high heat resistance and a very small thermal expansion coefficient compared to other substances (Kim, Park *et al.* 2009). The in plane metallic bonding also enables graphite to be a good electrical conductor. The thermal and electrical properties of graphite are not transferable perpendicular to the layers, due to its weak van der Waals forces (Chung 2002). These properties have, historically, fueled the interest in graphite. With the explosion of nanotechnology, there has been an increase in the interest towards graphite due to three reasons. First, the Dirac equation is used to describe the electron transport within the layers of graphite. Second, devices may be made on the nanoscale, due to its chemical and mechanical stability and ballistic transport at room temperature, which is viable for a few layers of graphite. Third, graphite is a precursor to graphene, which is considered a derivative of nanotubes and buckyballs. Because of the ability to predict the way graphite will behave in certain situations, there has been increased interest in it, especially in the nanoscale.

The renewed interest in graphite has led to exploration of the different ways that it can be exfoliated. Physical methods are used for producing graphene from graphite. One such method is the scotch tape method, in which scotch tape is applied to cleaved graphite to remove graphene layers (Novoselov, Geim *et al.* 2004). Another physical method includes expanding graphite intercalated compounds (GIC), then grinding the GIC to produce graphene layers (Fukushima, T Drzal *et al.* 2006; Kim, Park *et al.* 2009). Electrostatic deposition also produces graphene from graphite (Sidorov, Yazdanpanah *et al.* 2007). However, chemical exfoliation is a common process of producing exfoliated

graphite. Graphite oxides have been produced from exfoliated graphite by using $KMnO_4$ (Hummers and Offeman 1958; Becerril, Mao *et al.* 2008; Chandra, Bag *et al.* 2012), $K_2Cr_2O_7$ (Chandra, Sahu *et al.* 2010), $KClO_3$ (McAllister, Li *et al.* 2007; Wang, Yang *et al.* 2008), and m-CPBA(Chattopadhyay, Mukherjee *et al.* 2008). Haddon (Niyogi, Bekyarova *et al.* 2006) used a method that combined both physical (sonication) and chemical (H_2SO_4 and HNO_3) exfoliation. The Billups group at Rice University has studied other ways of exfoliating graphite without introducing oxides to the graphite; such as using benzoyl peroxide and lithium and ammonium.(Chattopadhyay, Mukherjee *et al.* 2009; Mukherjee, Kang *et al.* 2011). The study by Chattopadhyay, *et al.* (2009) was based on a previous effort by the Billups group (Liang, Sadana *et al.* 2004) where lithium and ammonia was used to reduce single wall nanotubes. The team studying single wall nanotubes went on to prove that reduction of nanotubes could be accomplished by using sodium or potassium instead of lithium (Liang, Alemany *et al.* 2005). It is known that lithium, sodium and potassium can be used for alkylation reduction, with the reactivity varying with the sample reduced. In this thesis I describe the results of using sodium and ammonia in the reduction of graphite.

2.2 Experimental

Materials

The graphite (powder, <20 μm, synthetic), sodium (cube, 99.9%), 1-iodobutane (99%), 1-iodooctane (98%), 1-iodododecane (98%), 1-iodohexadecane (95%), and ethanol (190 proof) were purchased from Sigma-Aldrich. The gas used was ultra-high purity argon and anhydrous ammonia. All materials were used as received.

Synthesis

The mole ratio for the graphite: sodium: alkyl halide used is 1:10:6. The following alkyl halides were used in the indicated amounts: 1-iodobutane (5.8 mL, 50.9 mmol), 1-iodooctane (9.0 mL, 49.8 mmol), 1-iododododecane (12.0 mL, 48.6 mmol), and 1-iodohexadecane (16 mL, 50.9 mmol).

The atmosphere in a dry ice condenser attached to a 250 mL three neck round bottom flask was removed via vacuum, flame dried until condensation of water stops, and replaced with argon gas. A dry ice and acetone mixture (-78 ^{o}C) was added to the condenser to cool the apparatus. Graphite (0.100 g, 8.3 mmol) was then added to the three neck flask; ammonia (~160 mL) was condensed into the flask and sodium (2.1 g, 91.3 mmol) was added. The mixture was stirred until all the sodium was dissolved, approximately 30 minutes, while keeping the solution at -33 ^{o}C. An alkyl halide was added to the solution and reacted for 6 hours while maintaining the temperature at -33 ^{o}C. The solution was reacted overnight until all of the ammonia evaporated. The next morning, ethanol (190 proof) was added to the product to react with any unreacted sodium. The solution was then washed with an ethanol, and water mixture and filtered with a 0.2 μm PTFE Whatman membrane. The resultant solid was dried overnight.

Characterization

The functionalized graphite was characterized by Raman spectroscopy, Fourier transform infrared spectroscopy (FTIR), thermo-gravimetric analysis (TGA), X-ray diffraction (XRD), X-ray photoelectron spectroscopy (XPS), high resolution transmission

electron microscope (HRTEM) and atomic force microscope(AFM). The TGA data was obtained with a Q-600 simultaneous DSC-TGA from TA Instruments. The samples were ramped to 100 ^{o}C and remained at that temperature for 15 min in order to remove any water that may be absorbed on the sample, and then they were ramped for 10 min to 800 ^{o}C. Raman samples were analyzed with Renishaw 1000 Raman system equipped with a 514nm laser source. FTIR spectra were acquired on a Nicolet FTIR microscope, fitted with an attenuated total reflectance (ATR) module. The JEOL 2100 field emission gun TEM operating at 100 kV imaged the samples, which were on Ted Pella's Lacey grid. The AFM images were obtained using a Digital Instruments Nanoscope IIIA in tapping mode. The XPS data was obtained with a PHI Quantera XPS with a monochromatic Al X-ray source mounted on aluminum. A Rigaku Ultima II Powder XRD was used to obtain the XRD patterns. These characterizations provide the proof that the samples were functionalized.

2.3 Results and Discussions

The Billups Birch reduction of graphite to yield alkylated exfoliated graphite (Scheme 2) proceeds through the use of a solvated electron (Scheme 1). This process is illustrated below.

Scheme 1: Electron solvation

$$NH_3\,(l) + Na\,(s) \longrightarrow Na^+ + e^-\,[NH_3]_n$$

Scheme 2: Billups-Birch alkyl reduction

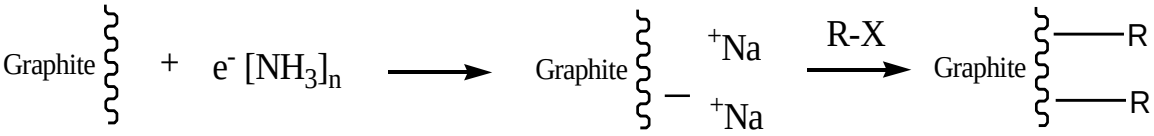

Raman spectroscopy can be used to show an increase in defects in the aromatic rings of functionalized graphite. Unfunctionalized graphite has a strong feature associated with it, located at ~1580 cm^{-1} (G peak). The G peak is associated with in-plane bond stretching between pairs of C sp^2 atoms. Functionalization of graphite causes defects in the aromaticity by reducing C sp^2 to sp^3. This results in a decrease in the G peak and an introduction of a peak at ~1350 (D peak) which is associated with the breathing mode of the ring. The D peak is only seen when disorder is introduced into the rings (Ferrari and Robertson 2000; Ferrari, Meyer *et al.* 2006). In Figure 3, the Raman spectrum for graphite (C0) and functionalized graphite (with butane (C4), octane (C8), dodecane (C12), and hexadecane (C16)) is shown. The unfunctionalized graphite D/G peak ratio of 0.18 indicates that there are inherit defects in the graphite used. However, functionalization of the graphite provides at least a 100% increase in the amount of defects found in the solid. This indicates that the coating is being added to the graphite as it undergoes hybridization from sp^2 to sp^3 carbon. The Raman spectrum provides evidence that functionalization of graphite is occurring.

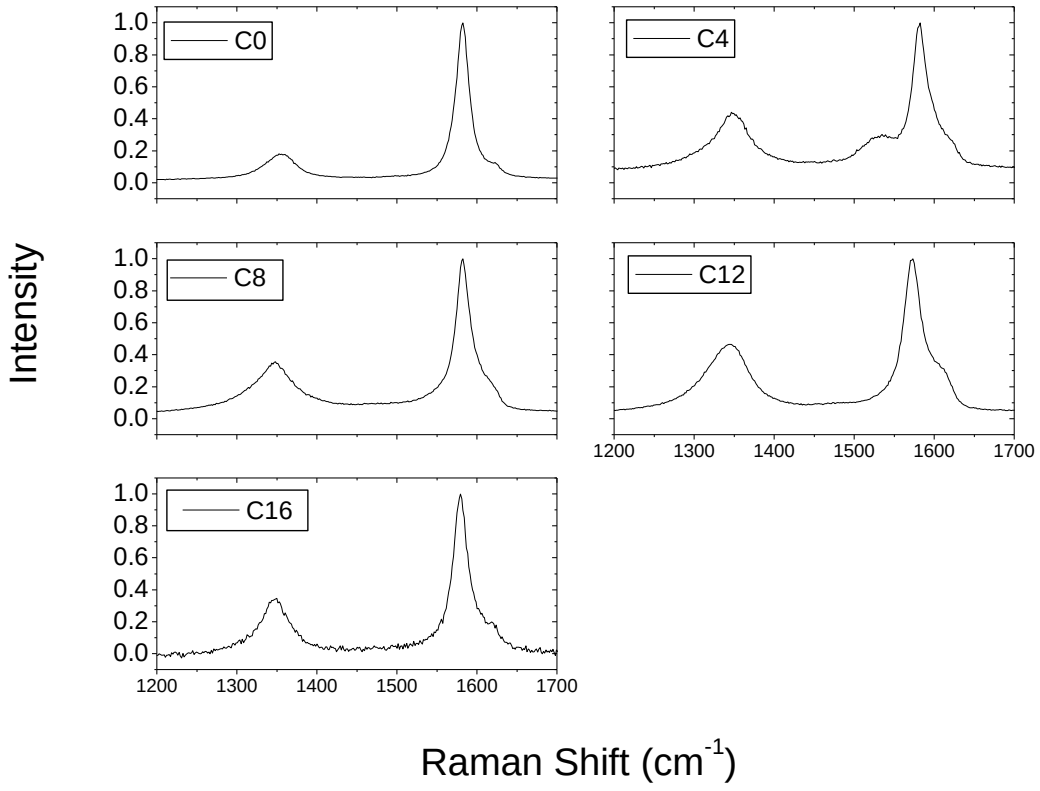

Figure 3. Raman spectrum showing the D and G peaks. The labels are: 1. C0 is for graphite, 2. C4 is for graphite coated butane, 3. C8 is for octane, 4. C12 is for dodecane, and 5. C16 is for hexadecane.

FT-IR is useful for indicating what functional groups are present on the compound being analyzed. The graphite and functionalized graphite was analyzed with FT-IR to see if the coating added would appear on the spectrum, and if it did, it would be an indicator that functionalization has occurred. Analysis of the butane, octane, dodecane and hexadecane functionalized graphite showed C-H stretching and bending peaks at ~2975 cm^{-1}, ~1380 cm^{-1}, and ~1050 cm^{-1}, which are indicators that the alkane chains were successfully attached to graphite (Brown and Foote 1998). This indicates that functionalization occurs. Spectrums of the data are shown in Figure 4.

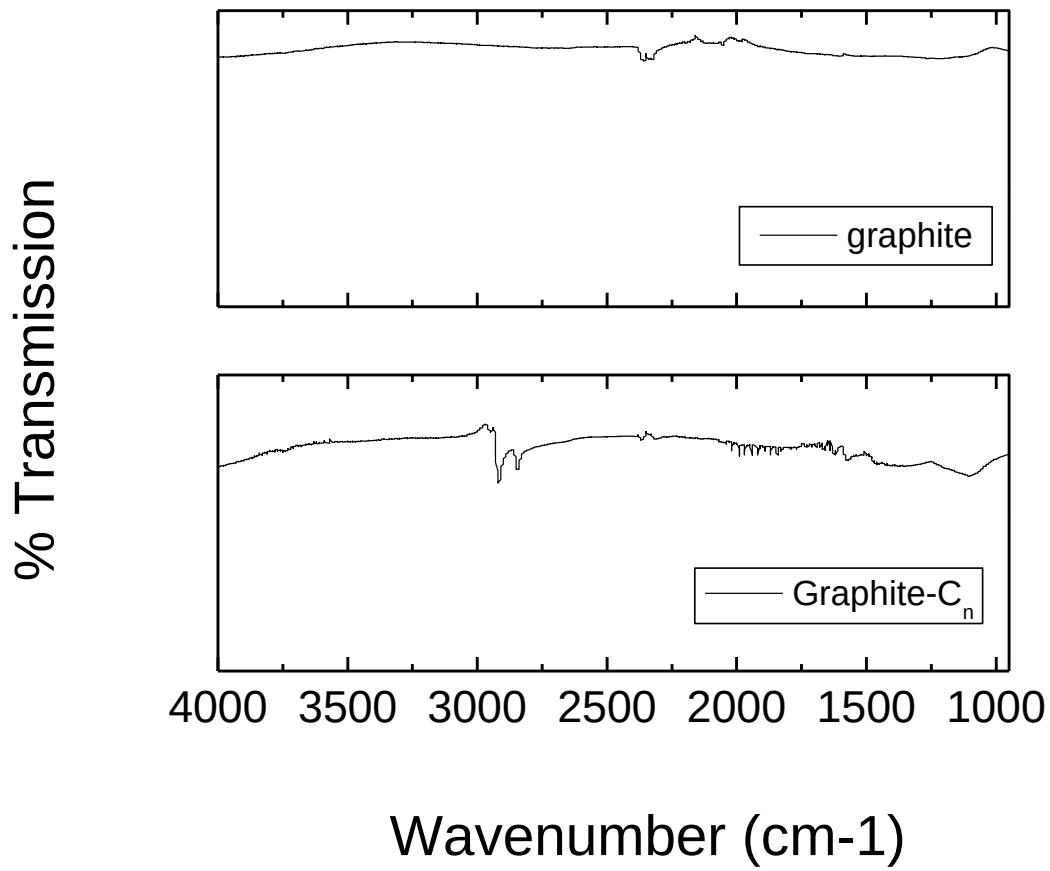

Figure 4. FTIR spectrum of (from top to bottom): graphite, graphite coated with an alkane, and graphite coated with pentanoic acid.

TGA has been shown to be an indicator for the degree of functionalization (Dyke and Tour 2003). Therefore it is a useful indicator to determine if functionalization has occurred. When graphite is analyzed with TGA, no weight loss occurs. However, after performing an alkylation reduction, the spectrum shows a reduction in the original weight of the sample, which indicates that a coating was added to graphite. Figure 5 shows a spectrum which indicates, that primarily, the reduction occurs in the temperature range of 250 ^{o}C - 500 ^{o}C.

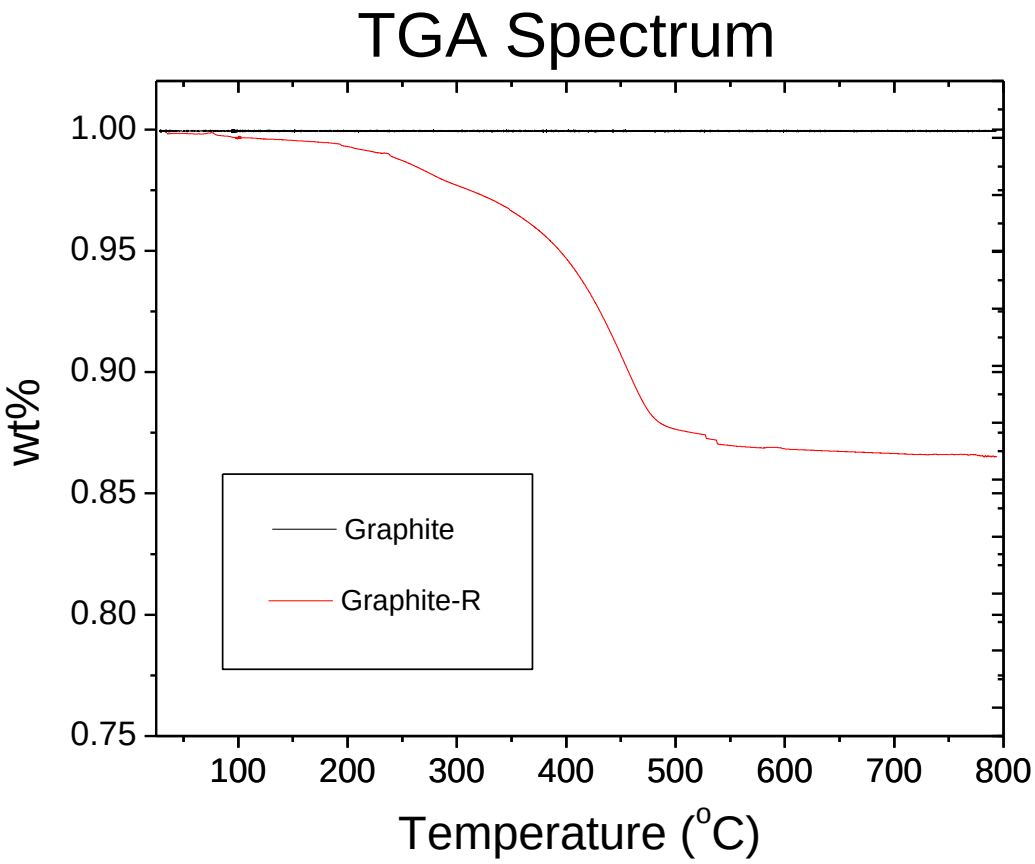

Figure 5.TGA spectrum showing graphite and coated graphite. The figure shows the temperature when coating on graphite is removed and the amount that is removed.

Analysis of the data (see Table 1. Average TGA Data), indicates the amount of the coating that was loss and the number of compounds that were attached to the graphite sample. The value of the amount of compound that was attached to graphite was shown to be similar when compared by means with Student's t.

Equation 1

$$t_{calculated} = \frac{\bar{x}_1 - \bar{x}_2}{s_{pooled}} \sqrt{\frac{n_1 n_2}{n_1 + n_2}}$$

Equation 2

$$s_{pooled} = \sqrt{\frac{s_1^2(n_1 - a) + s_2^2(n_2 - 1)}{n_1 + n_2 - 2}}$$

Here, $\bar{x}$ is the average number of molecules on graphite for each compound; n is the number of observations, and s is the standard deviation of the average. The $t_{calculated}$ for each comparison was less than the value for the 95% Confidence level, which means that the results are similar (Harris 1999). This data shows that the number of graphite added to graphite did not depend on the difference in the compounds' chain length (7.150 Å for butane, 13.770 Å for octane, 19.890 Å for dodecane, and 26.010 for hexadecane). The percent weight loss is not a good indicator of the similarity of the results because of the differences in weight due to the chain length. Table 1 indicates the amount of coating that was added to the graphite.

Table 1. Average TGA Data

Compound	Weight loss (%) observed	Average number of the compound attached to the sample	Standard deviation
Graphite	0	0	0
Butane	8	1.7119E+18	7.9435E+17
Octane	10.5	1.2288E+18	3.9485E+17
Dodecane	10.5	7.8440E+17	1.4269E+17
Hexadecane	40	2.3066E+18	7.8982E+17

XPS is useful for determining the way atoms within a molecule interacts. As an aromatic element, a characteristic feature of XPS associated with graphite is the appearance of a shake-up line. This distinctive peak is associated with the energy from

the $\pi \rightarrow \pi^*$ transition and can be seen in the spectrum at ~7 eV higher than the C 1s binding energy (Moulder, Stickle *et al.* 1995; Heide 2012). Comparing graphite with graphite coated with butane, octane, dodecane, and hexadecane, it is seen that the shake-up peak disappears. For the butane coated peak, the baseline is higher than in the graphite peak, but the baseline does not contain any peaks. It is difficult to determine if the octane baseline contains any peak just by looking, but drawing a straight line along the baseline showed that there was not any peaks present. The XPS spectrum of the samples is seen in Figure 6. The XPS data confirmed that graphite has been coated with substrate.

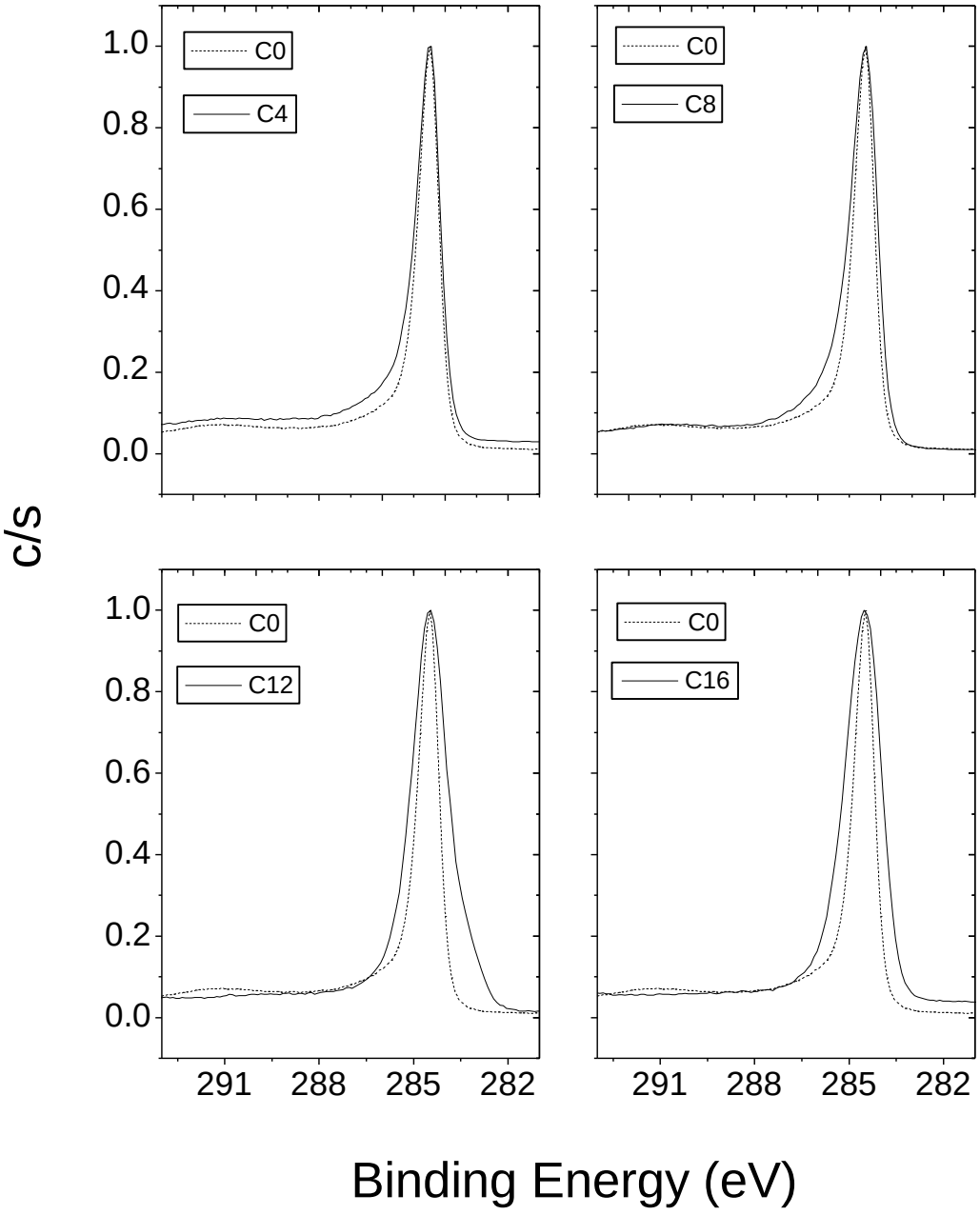

Figure 6. XPS spectrum comparing graphite with coated graphite. The labels are: 1. C0 is for graphite, 2. C4 is for graphite coated butane, 3. C8 is for octane, 4. C12 is for dodecane, and 5. C16 is for hexadecane.

Figure 7 shows AFM images, in tapping mode, of graphite coated with dodecane. The images show that coated graphite has separated into non uniform shapes with a width ranging from 0.2 - 1.2 μm. Height analysis of the forms show that the height of these shapes is less than 1 nm, which is on par with literature values for graphene sheets (Li, 2008). This suggests that the graphite was exfoliated due to the functionalization of graphite.

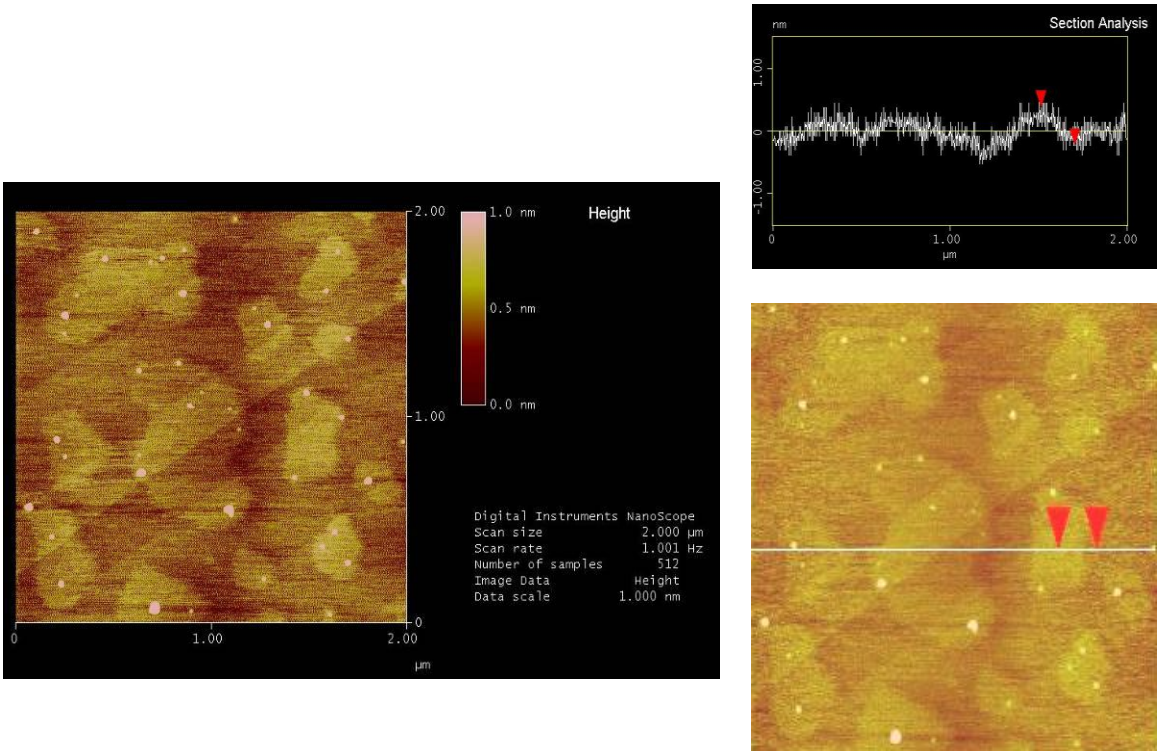

Figure 7. AFM images (Upper) A 2x2 μm AFM image solution. (Left) A height section analysis of particles. The lower image shows the area the height is measured (indicated by the white line) and the upper image indicates the measurement results. The red arrows in the two images correspond and indicates the height of the sample on and off a particle.

The exfoliation of graphite and the attachment of alkane chains led to the increase of solubility of graphite in chloroform. The pure graphite and graphite coated with

butane fell out of solution between 4 and 24 hours. However one week later, the graphite coated with octane, dodecane, and hexadecane was still suspended in chloroform. Unfortunately, the evaporation of the chloroform made it impossible to determine how long the particles would have remained in solution. Comparing the images in Figure 8, the octane, dodecane and hexadecane are clearly suspended in the solution with some of the particles crashed out of the solution. Thus the attachment of alkane side chains led to the particles taking on a solubility property of the chain.

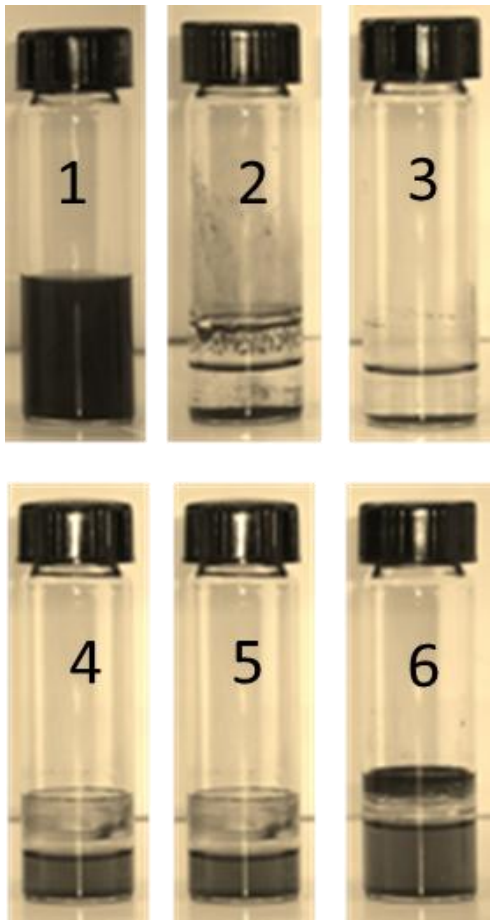

Figure 8. Images showing solubility: 1. Graphite sample in chloroform at t = 0; 2. Graphite sample in chloroform at t = 1 week; 3. Graphite coated with butane in chloroform at t = 1 week 4. Graphite coated with octane in chloroform at t = 1 week; 5. Graphite coated with dodecane in chloroform at t = 1 week; 6. Graphite coated with hexadecane in chloroform at t = 1 week

2.4 Conclusion

The results indicate that reductive alkylation using sodium as an electron donor is a valid method for producing alkyl coated exfoliated graphite. The data presented here compared with the results of the Chattopadhyay (2009) paper are significant for three reasons. First, comparing the results using the t-test indicates the amount of substrate added to graphite is similar; which demonstrate that sodium may be used instead of lithium in this reaction without a significant change in the amount of substrate added. Second, the use of sodium in this reaction instead of lithium is better for biomedical applications. Lithium is known to be toxic at levels greater than 2.5 mmol/L and it has no benefits in the normal function of a human body (Waring 2006). However, sodium is needed to keep the human body functioning regularly and it has a much higher toxicity level (>150 mmol/L) than lithium (Kupiec, Goldenring *et al.* 2004). Thus it is preferable to use sodium instead of lithium for compounds that will have use in biomedicine. Third, the addition of the substrate exfoliates the graphite powder ($\leq$ 20 μm); so the specialized exfoliated graphite used in Chattopadhyay (2009) is not necessary to achieve the desired results. These arguments prove sodium is the better choice than lithium in this reaction and that any alkyl halide may be added to the graphite to yield similar results.

CHAPTER 3. CHEMICAL MODIFICATION OF EXFOLIATED GRAPHITE VIA THE BILLUPS-BIRCH ALKYLCARBOXYLATION REACTION

3.1 Introduction

The use of graphene oxide in the biomedical field has recently been explored. It has been found that graphene oxide can deliver water insoluble drugs, fluorescence dyes for imaging, and DNA for use in gene therapy. The use of graphene oxide to accomplish these feats solved the problems normally inherent in those processes (Liu, Robinson *et al.* 2008; Mintzer and Simanek 2008; Yang, Zhang *et al.* 2008; He, Song *et al.* 2010; Lu, Li *et al.* 2010; Lu, Zhu *et al.* 2010; Zhang, Xia *et al.* 2010; Chen, Liu *et al.* 2011; Feng, Zhang *et al.* 2011). The design of carrier vector that prevents oligonucleotide and DNA degradation and is not toxic was a problem in the afore mentioned fields which the use of graphene oxide solved (Mintzer and Simanek 2008). However, the production of graphene oxide uses non ideal reaction conditions, such as the use of strong acids and peroxides.

Functionalization of pristine graphite using the Billups-Birch alkylcarboxylation reaction provides an alternative pathway to highly exfoliated defect free graphene that is functionalized by carboxylic groups which can be converted to acid chlorides. Because the corresponding acid chlorides can be reacted with a large variety of nucleophiles, they provide a point of departure for the synthesis of uniquely functionalized graphene including amides, esters and other carbonyl addition products that promise to find important applications in nanotechnology and biomedicine (Jones 2005). In this chapter, I will describe the synthesis of exfoliated graphene functionalized by amides and esters.

3.2 Experimental

Materials

Graphite (powder, <20 μm, synthetic), sodium (cube, 99.9%), 5-bromovaleric (97%), thionyl chloride (99.5%), N,N-dimethylformamide (99.9%), octadecylamine (97%), ethanol (190 proof) and benzene (ACS grade) were purchased from Sigma-Aldrich. Polyethylenimine (MW ~25,000) was purchased from Polysciences, Inc. The gas used was ultra-high purity argon and anhydrous ammonia. All materials were used as received.

Synthesis of pentanoic acid coated exfoliated graphite

The atmosphere in a dry ice condenser attached to a 250 mL three neck round bottom flask was removed via vacuum, flame dried until condensation of water stops, and replaced with argon gas. A dry ice and acetone mixture (-78 ^{o}C) was added to the condenser to cool the apparatus. Graphite (0.100 g, 8.3 mmol) was then added to the three neck flask; ammonia (~160 mL) was condensed into the flask and sodium (2.1 g, 91.3 mmol) was added. The mixture was stirred until all the sodium was dissolved, approximately 30 minutes, while keeping the solution at -33 ^{o}C. 5-Bromovaleric acid (9.043 g, 49.9 mmol) was added to the solution and reacted for 6 hours while maintaining the temperature at -33 ^{o}C. The solution was reacted overnight until all of the ammonia evaporated. The next morning, ethanol (190 proof) was added to the product to react with any unreacted sodium. The solution was then washed with an ethanol and water

mixture and filtered with a 0.2 μm PTFE Whatman membrane. The resultant solid was dried overnight.

Synthesis of polyethylenimine coated exfoliated graphite

A reflux apparatus was assembled using a condenser and a 250 mL 3 neck round bottom flask. Once the apparatus was flushed with argon gas for 30 min, pentanoic acid coated exfoliated graphite (25 mg), from synthesis above, was added to the flask. Five drops of N, N-dimethylformamide, then 13 mL of thionyl chloride was added to the flask and refluxed for 24 hours. Polyethylenimine, linear (0.810 g; MW ~25,000), and benzene (15 mL) was added to the solution and reacted for five hours. Water (100 mL) was added to solution and mixed for 1 hour. The mixture was washed with benzene (3x), then filtered with a 0.2 μm PTFE Whatman membrane to obtain a grey solid.

Synthesis of octadecylamine coated exfoliated graphite

A reflux apparatus was assembled using a condenser and a 250 mL 3 neck round bottom flask. Once the apparatus was flushed with argon gas for 30 min, pentanoic acid coated exfoliated graphite (25 mg), from synthesis above, was added to the flask. Five drops of N, N-dimethylformamide, then 13 mL of thionyl chloride was added to the flask and refluxed for 24 hours. Octadecylamine (0.010 g, 0.0371 mmol) , and benzene (15 mL) was added to the solution and reacted for five hours. Water (100 mL) was added to solution and mixed for 1 hour. The mixture was washed with benzene (3x), then filtered with a 0.2 μm PTFE Whatman membrane to obtain the solid.

Characterization

The functionalized graphite was characterized by Raman spectroscopy, Fourier transform infrared spectroscopy (FTIR), thermo-gravimetric analysis (TGA), X-ray photoelectron spectroscopy (XPS), and high resolution transmission electron microscope (HRTEM). The TGA data was obtained with a Q-600 simultaneous DSC-TGA from TA Instruments. The samples were ramped to 100 ^{o}C and remained at that temperature for 15 min in order to remove any water that may be absorbed on the sample, and they were ramped for 10 min to 800 ^{o}C. Raman samples were analyzed with Renishaw 1000 Raman system equipped with a 514nm laser source. FTIR spectra were acquired on a Nicolet FTIR microscope, fitted with an attenuated total reflectance (ATR) module. The JEOL 2100 field emission gun TEM operating at 100 kV imaged the samples, which were on Ted Pella's Lacey grid. The XPS data was obtained with a PHI Quantera XPS with a monochromatic Al X-ray source, mounted on aluminum. These characterizations provide the proof that the samples were functionalized.

3.3 Results and Discussions

The alkylcarboxylation of graphene using 5-bromopentanoic acid is illustrated in Scheme 3. Scheme 4 shows the process of producing acid chlorides and Scheme 5 shows the nonspecific addition-elimination reaction to produce the desired product.

Scheme 3: Billups-Birch alkylcarboxylation reduction

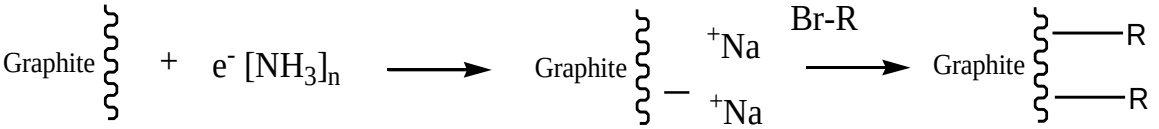

R = pentanoic acid

Scheme 4: Acid chloride formation

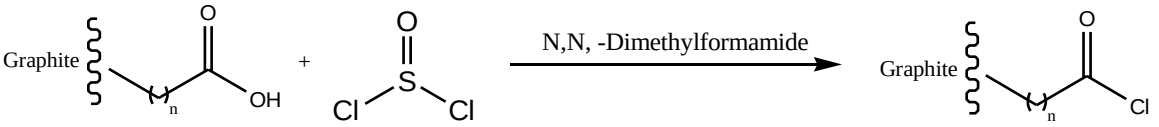

Scheme 5: Nucleophilic addition-elimination reaction

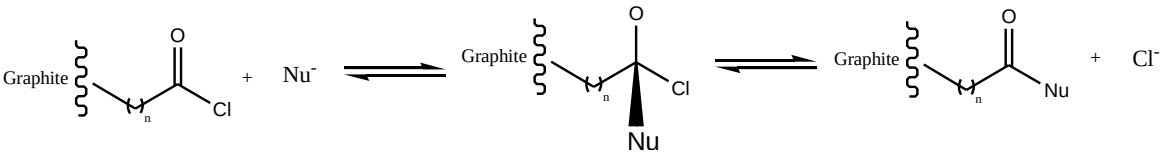

Figure 9 displays the spectra from TGA, Raman, FTIR, and XPS to prove that pentanoic acid was attached to exfoliated graphite. The TGA spectrum shows that 9.64 wt% of pentanoic acid was functionalized to graphite (Dyke and Tour 2003). The ratio of the D/G peak in the Raman spectrum shows a 100% increase in the amount of defects in the aromatic rings found as compared to unfunctionalized graphite in Figure 3. This is indicative of pentanoic acid bonding to graphite as it undergoes hybridization from sp^2 to sp^3 carbon. The FTIR data shows the O-H stretch at ~3650 cm^{-1}, which indicates that there is a OH group in the compound (Brown and Foote 1998). The XPS spectrum does not contain the shake-up peak that indicates aromatic compounds, thus it shows that defects are present in the sample. Also, another peak appears close to the main carbon peak and is identified as the carbon bonded to oxygen peak. (Naumkin, Kraut-Vass *et al.* 2006) This data shows the graphite sample contains defects and carbon bonded to

oxygen. This information along with results from the previous chapter indicate that graphene sheets functionalized with pentanoic acid was produced.

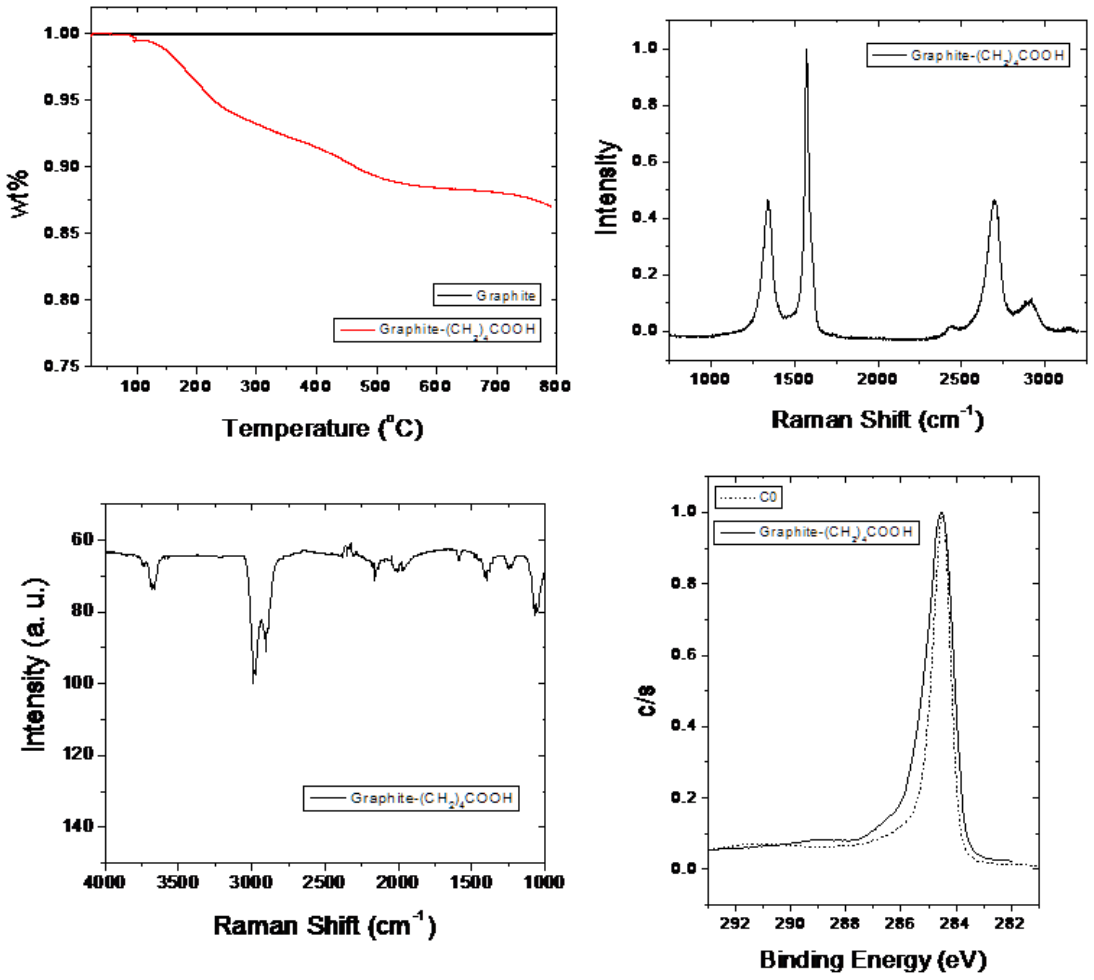

Figure 9. These spectrum show data for the attachment of pentanoic acid to graphite. (Top Left) TGA data; (Top Right) Raman Data; (Bottom Left) FTIR data; (Bottom Right) XPS data

Figure 10 shows the XPS data for octadecylamine and polyethylenimine attached to carboxyl functionalized exfoliated graphite. The C 1s peaks do not have the shake-up peak associated with aromatic carbon, which indicates that the graphite is functionalized.

The peaks associated with the O 1s and the N 1s in octadecylamine are ~532.3 eV and ~399.6 eV respectively (Naumkin, Kraut-Vass *et al.* 2006). These peaks are associated with amides thus giving a good indicator that octadecylamine was successfully attached via an addition-elimination reaction. The O 1s, ~530.7 eV, in polyethylenimine is associated with esters and the N 1s peak, ~398.3 eV, is associated with the appearance of amines. These peaks indicate that an addition-elimination reaction occurred attaching polyethylenimine to carbon chain. XPS indicates that octadecylamine and polyethylenimine were successfully covalently added to graphite.

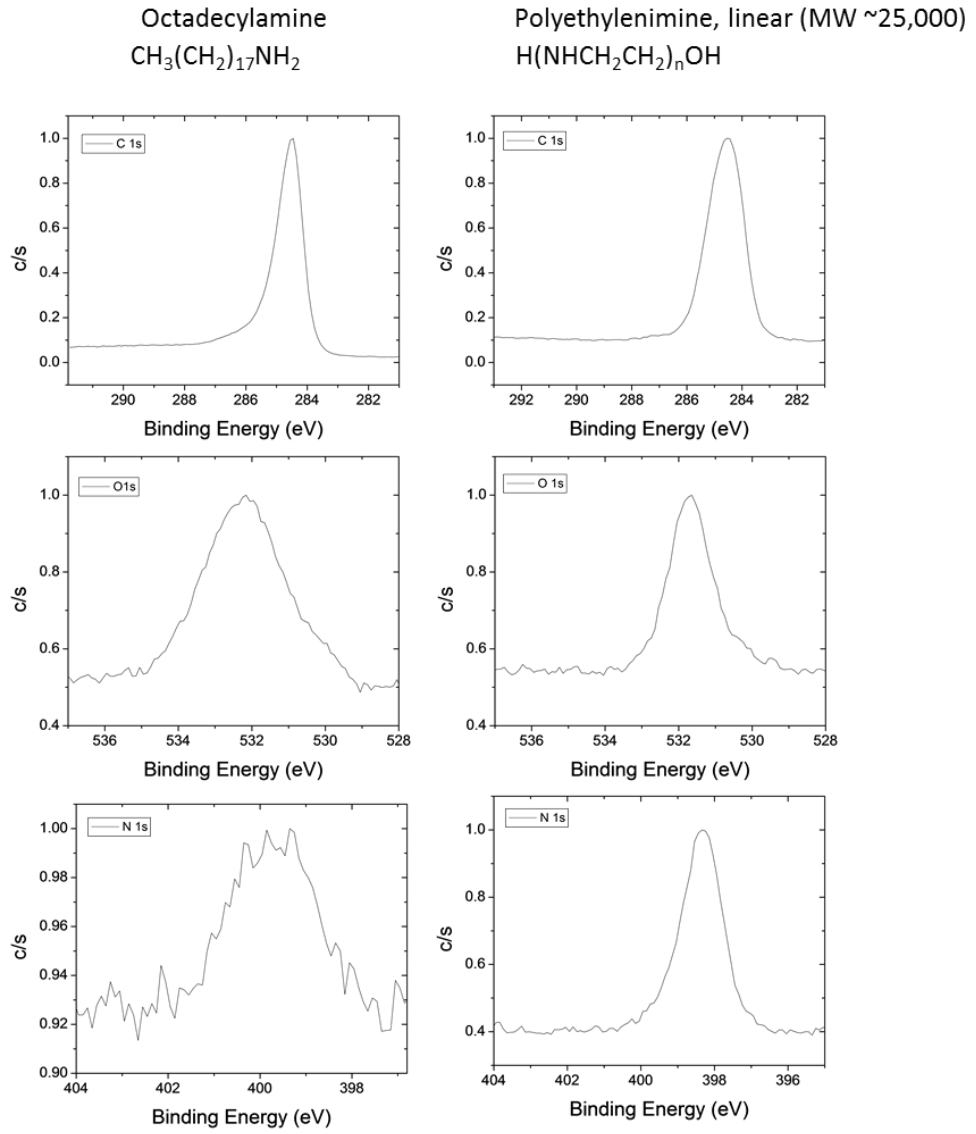

Figure 10. XPS data for the attachment of octadecylamine and polyethylenimine to graphite.

FT-IR spectrum in Figure 11 was used to determine if certain functional groups were present in the compounds. In the spectrum indicating graphite coated with pentanoic acid, the broad peak around 3000 cm^{-1} is indicative of carboxylic group O-H stretch (Jones 2005). The medium size peak at ~3770 cm^{-1} in the octadecylamine

spectrum is associated with an N-H amide stretch. This is an indicator that octadecylamine was covalently attached to form an amide (Merlic 2000). The polyethylenimine spectrum has a N-H stretch peak at ~3260 cm^{-1} which indicates secondary amines are present and contains the C=O stretch seen in previous studies on single wall nanotubes and coal performed in the Billups lab. These peaks are indicators that polyethylenimine was successfully attached. The FT-IR data suggest that octadecylamine and polyethylenimine were successfully attached.

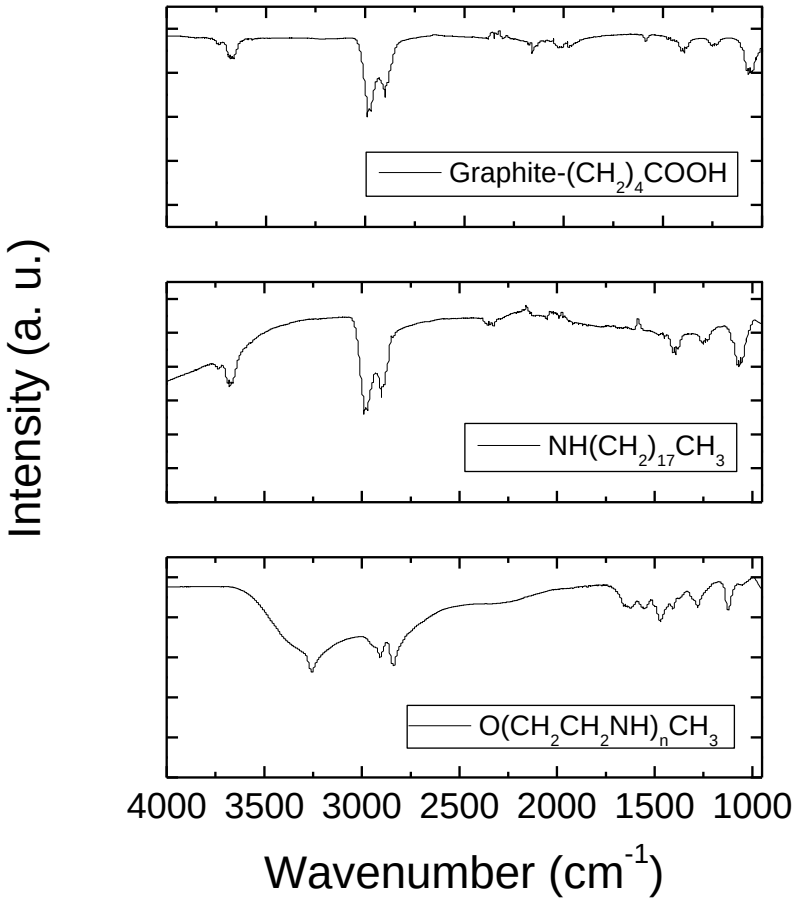

Figure 11. FTIR data for the attachment of octadecylamine and polyethylenimine

The TEM images shown in Figure 12 are of exfoliated graphite coated with polyethylenimine. High resolution TEM of the sample is shown in Figure 12. This high res image shows graphite as being made up of stacked lines (the lattice) while along graphite's edge is an amorphous nodule. This nodules is the PEI attached to graphite. These images indicate that the attachment of PEI and octadecylamine occurred.

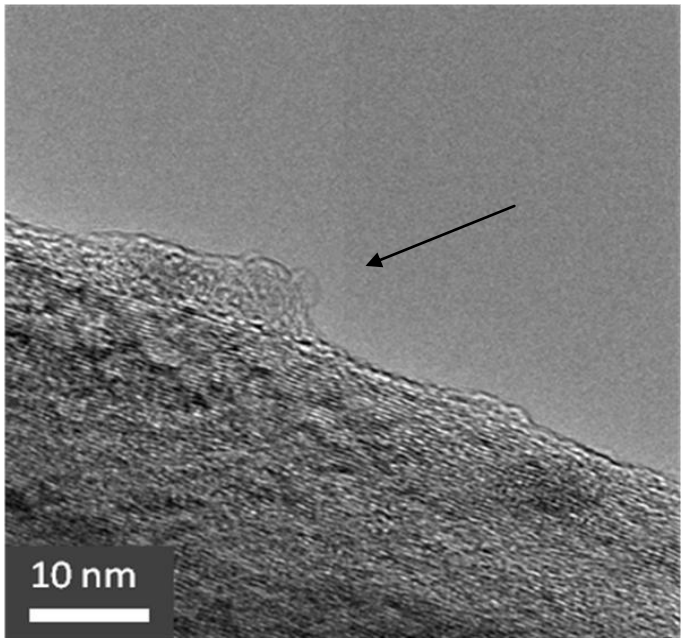

Figure 12**.** Images of PEI coated graphite; image B is a high resolution image.

TGA data of PEI attached graphite show a 60% weight loss. Subtracting the weight loss of pentanoic acid from the total weight loss gives 1.042 mg weight loss of PEI. Due to the high weight of PEI, the amount of molecules present on the sample is 2.52×10^{16} which is 2 orders of magnitude less than the amount of pentanoic acid added as seen in Table 2. This shows while PEI was attached, there were many sites of attachment that were not utilized. This may be due to inefficiency of the reaction or to

the large size of PEI. PEI may be so large that steric hindrance may be occurring when more PEI is trying to attach to the sample.

Table 2.Amount of PEI and pentanoic acid present on exfoliated graphite sample

	Molecules of coating on sample
Pentanoic Acid	1.84E+18
Polyethylenimine	2.51E+16

3.4 Conclusion

The data presented shows attachment of polyethylenimine and octadecylamine (both of which has previous uses in biomedicine) to graphene sheets (Dubrovin, Gerritsen *et al.* 2010; Chen, Liu *et al.* 2011). The attachment of the moiety to graphite was not 1 to 1 ratio of the moiety to pentanoic acid, which may be due to inefficiency or steric hindrance associated with the size of the moiety attached. But even with this restriction, this method is viable for the addition of nitrogen and oxygen accessible containing compounds for functionalization to graphite. Using the Billups-Birch alkylcarboxylation reaction by way of an addition-elimination reaction with an acid chloride opens up the use of graphite in nanotechnology, specifically biomedicine.

CHAPTER 4. CONCLUSIONS

This body of work introduces the use of sodium in the Billups-Birch alkyl reaction with graphite. It proves that it is viable to use the less toxic sodium instead of lithium in the reduction because the results are comparable in the production of exfoliated graphite in the size range of graphene. It also shows that the Billups-Birch alkyl reaction may be modified to an alkylcarboxylation reaction. This increases the quantity of compounds that can be attached to graphite by combining it with an acid chloride addition-elimination reaction. Thereby providing an easy way of producing the product of interest. This body of work offers new ways of producing functionalized exfoliated graphite for use in biomedical applications.

REFERENCES

Becerril, H. A., J. Mao, *et al.* (2008). "Evaluation of solution-processed reduced graphene oxide films as transparent conductors." ACS Nano 2(3): 463-470.

Brown, W. H. and C. S. Foote (1998).Organic Chemistry. New York, Saunders College Publishing.

Chandra, S., S. Bag, *et al.* (2012)."Fabrication of magnetically separable palladium-graphene nanocomposite with unique catalytic property of hydrogenation." Chemical Physics Letters 519-20: 59-63.

Chandra, S., S. Sahu, *et al.* (2010)."A novel synthesis of graphene by dichromate oxidation." Materials Science and Engineering B-Advanced Functional Solid-State Materials 167(3): 133-136.

Chattopadhyay, J., A. Mukherjee, *et al.* (2009). "Exfoliated soluble graphite." Carbon 47(13): 2945-2949.

Chattopadhyay, J., A. Mukherjee, *et al.* (2008). "Graphite epoxide." Journal of the American Chemical Society 130(16): 5414-+.

Chen, B., M. Liu, *et al.* (2011). "Polyethylenimine-functionalized graphene oxide as an efficient gene delivery vector."Journal of Materials Chemistry 21(21): 7736-7741.

Chung, D. D. L. (2002). "Review graphite." Journal of Materials Science 37(8): 1475-1489.

Cotton, F. A., G. Wilkinson, *et al.* (1999). Advanced Inorganic Chemistry.New York, Wiley-Interscience.

Dubrovin, E. V., J. W. Gerritsen, et al. (2010). "The effect of underlying octadecylamine monolayer on the DNA conformation on the graphite surface." Colloids and Surfaces B-Biointerfaces **76**(1): 63-69.

Dyke, C. A. and J. M. Tour (2003)."Solvent-Free Functionalization of Carbon Nanotubes." Journal of the American Chemical Society 125(5): 1156-1157.

Feng, L., S. Zhang, *et al.* (2011). "Graphene based gene transfection." Nanoscale 3(3): 1252-1257.

Ferrari, A. C., J. C. Meyer, *et al.* (2006). "Raman Spectrum of Graphene and Graphene Layers." Physical Review Letters 97(18): 187401.

Ferrari, A. C. and J. Robertson (2000)."Interpretation of Raman spectra of disordered and amorphous carbon." Physical Review B 61(20): 14095-14107.

Fletcher, A. (2008). "Carbon."Retrieved October 31, 2012, from http://personal.strath.ac.uk/ashleigh.fletcher/carbon.htm.

Fukushima, H., L. T Drzal, *et al.* (2006). "Thermal conductivity of exfoliated graphite nanocomposites." Journal of Thermal Analysis and Calorimetry 85(1): 235-238.

Gupta, A. K. and M. Gupta (2005)."Synthesis and surface engineering of iron oxide nanoparticles for biomedical applications." Biomaterials 26(18): 3995-4021.

Harris, D. C. (1999).Quantitative Chemical Analysis. USA, W. H. Freeman and Company.

He, S., B. Song, *et al.* (2010)."A Graphene Nanoprobe for Rapid, Sensitive, and Multicolor Fluorescent DNA Analysis."Advanced Functional Materials 20(3): 453-459.

Heide, P. V. D. (2012). X-ray Photoelectron Spectroscopy: An Introduction to Principles and Practices. Hoboken, John Wiley & Sons, Inc.

Hummers, W. S. and R. E. Offeman (1958)."Preparation of Graphitic Oxide." Journal of the American Chemical Society 80(6): 1339-1339.

Jamison, J. A., E. L. Bryant, *et al.* (2011). "Altering protein surface charge with chemical modification modulates protein-gold nanoparticle aggregation." Journal of Nanoparticle Research 13(2): 625-636.

Kim, B. G., C. L. Park, *et al.* (2009). "Fabrication of Platelet-Like Natural Crystalline Graphite with Nano-Scale Thickness via Layer Distance Expansion." Materials Transactions 50(9): 2323-2328.

Krapcho, A. P. and A. A. Bothner (1959). "Kinetics of the Metal-Ammonia-Alcohol Reductions of Benzene and Substituted Benzenes1." Journal of the American Chemical Society 81(14): 3658-3666.

Kupiec, T. C., J. M. Goldenring, et al. (2004). "A non-fatal case of sodium toxicity." Journal of Analytical Toxicology **28**(6): 526-528.

Liang, F., L. B. Alemany, *et al.* (2005)."Structure Analyses of Dodecylated Single-Walled Carbon Nanotubes." Journal of the American Chemical Society 127(40): 13941-13948.

Liang, F., A. K. Sadana, *et al.* (2004)."A Convenient Route to Functionalized Carbon Nanotubes." Nano Letters 4(7): 1257-1260.

Liga, M. V., E. L. Bryant, *et al.* (2011). "Virus inactivation by silver doped titanium dioxide nanoparticles for drinking water treatment." Water Research 45(2): 535-544.

Liu, Z., J. T. Robinson, *et al.* (2008). "PEGylated nanographene oxide for delivery of water-insoluble cancer drugs."Journal of the American Chemical Society 130(33): 10876-+.

Lu, C.-H., J. Li, *et al.* (2010). "Increasing the Sensitivity and Single-Base Mismatch Selectivity of the Molecular Beacon Using Graphene Oxide as the "Nanoquencher"." Chemistry – A European Journal 16(16): 4889-4894.

Lu, C.-H., C.-L.Zhu, *et al.* (2010)."Using graphene to protect DNA from cleavage during cellular delivery." Chemical Communications 46(18): 3116-3118.

McAllister, M. J., J. L. Li, *et al.* (2007). "Single sheet functionalized graphene by oxidation and thermal expansion of graphite." Chemistry of Materials 19(18): 4396-4404.

Mintzer, M. A. and E. E. Simanek (2008)."Nonviral Vectors for Gene Delivery."Chemical Reviews 109(2): 259-302.

Mohapatra, M. and S. Anand (2010)."Synthesis and applications of nano-structured iron oxides/hydroxides – a review." International Journal of Engineering, Science and Technology 2(8): 127-146.

Moulder, J. F., W. F. Stickle, *et al.* (1995). Handbook of X-Ray Photoelectron Spectroscopy. Eden Prairie, Physical Electronics, Inc.

Mukherjee, A., J. Kang, *et al.* (2011). "Water-Soluble Graphite Nanoplatelets Formed by Oleum Exfoliation of Graphite." Chemistry of Materials 23(1): 9-13.

NanoSight. (2012). "Duke University uses Nanoparticle Tracking Analysis to characterize "nanoconstructs" for biomedical applications." 2012.

Niyogi, S., E. Bekyarova, *et al.* (2006)."Solution properties of graphite and graphene." Journal of the American Chemical Society 128(24): 7720-7721.

Novoselov, K. S., A. K. Geim, *et al.* (2004). "Electric field effect in atomically thin carbon films." Science 306(5696): 666-669.

Pankhurst, Q. A., J. Connolly, *et al.* (2003). "Applications of magnetic nanoparticles in biomedicine." Journal of Physics D-Applied Physics 36(13): R167-R181.

Rabideau, P. W. (1989). "The Metal-Ammonia Reduction of Aromatic-Compounds." Tetrahedron 45(6): 1579-1603.

Sidorov, A. N., M. M. Yazdanpanah, *et al.* (2007). "Electrostatic deposition of graphene."Nanotechnology 18(13).

Silver Institute. (2012)."Silver in Nanotechnology."Retrieved Jan 2,, 2012, from http://www.silverinstitute.org/site/silver-in-technology/silver-in-nanotechnology/.

Tartaj, P., M. D. Morales, *et al.* (2003). "The preparation of magnetic nanoparticles for applications in biomedicine." Journal of Physics D-Applied Physics 36(13): R182-R197.

United States Social Security Administration. (2012)."Life Expectancy for Social Security." Retrieved January 2, 2013, 2013, from http://www.ssa.gov/history/lifeexpect.html.

Vasilev, K., J. Cook, *et al.* (2009). "Antibacterial surfaces for biomedical devices." Expert Review of Medical Devices 6(5): 553-567.

Visai, L., L. De Nardo, *et al.* "Titanium oxide antibacterial surfaces in biomedical devices." International Journal of Artificial Organs 34(9): 929-946.

Wang, G. X., J. Yang, *et al.* (2008). "Facile synthesis and characterization of graphene nanosheets." Journal of Physical Chemistry C 112(22): 8192-8195.

Waring, W. S. (2006). "Management of lithium toxicity." Toxicological reviews **25**(4): 221-30.

Yang, X., X. Zhang, *et al.* (2008)."High-Efficiency Loading and Controlled Release of Doxorubicin Hydrochloride on Graphene Oxide." The Journal of Physical Chemistry C 112(45): 17554-17558.

Zhang, D., O. Neumann, *et al.* (2009). "Gold Nanoparticles Can Induce the Formation of Protein-based Aggregates at Physiological pH." Nano Letters 9(2): 666-671.

Zhang, L., J. Xia, *et al.* (2010). "Functional Graphene Oxide as a Nanocarrier for Controlled Loading and Targeted Delivery of Mixed Anticancer Drugs."Small**6**(4): 537-544.

Zhang, P., Z. Zhang, *et al.* (2012). "Antibacterial TiO2 coating incorporating silver nanoparticles by micro-arc oxidation and ion implantation."Journal of Nanomaterials.

APPENDIX 1: VIRUS INACTIVATION BY SILVER DOPED TITANIUM DIOXIDE NANOPARTICLES FOR DRINKING WATER TREATMENT

Virus inactivation by silver doped titanium dioxide nanoparticles for drinking water treatment

Michael V. Liga[a], Erika L. Bryant[b], Vicki L. Colvin[b], Qilin Li[a,*]

Water Research 45, (2), 535-544

[a]Department of Civil and Environmental Engineering, Rice University, 6100 Main St., Houston, TX 77005, United States
[b]Department of Chemistry, Rice University, 6100 Main St., Houston, TX 77005, United States

Abstract

Photocatalytic inactivation of viruses and other microorganisms is a promising technology that has been increasingly utilized in recent years. In this study, photocatalytic silver doped titanium dioxide nanoparticles (nAg/TiO_2) were investigated for their capability of inactivating Bacteriophage MS2 in aqueous media. Nano-sized Ag deposits were formed on two commercial TiO_2 nanopowders using a photochemical reduction method. The MS2 inactivation kinetics of nAg/TiO_2 was compared to the base TiO_2 material and silver ions leached from the catalyst. The inactivation rate of MS2 was enhanced by more than 5 fold depending on the base TiO_2 material, and the inactivation efficiency increased with increasing silver content. The increased production of hydroxyl free radicals was found to be responsible for the enhanced viral inactivation.

Keywords: Drinking water, Nanotechnology, Photocatalysis, Silver, Titanium dioxide, Virus

Introduction

The removal of viruses and other pathogens from drinking water (and the environment in general) is important for the maintenance of the health and well being of society. Pathogenic viruses such as adenovirus, norovirus, rotavirus, and hepatitis A commonly occur in both surface and groundwater sources (Abbaszadegan, Lechevallier *et al.* 2003; Hamza, Jurzik *et al.* 2009; Wong, Kumar *et al.* 2009) and must be effectively inactivated to provide safe water. In the United States just between 2003 and 2005 there were four reported waterborne disease outbreaks attributed to viruses in drinking water affecting 282 people (Liang, Dziuban *et al.* 2006; Yoder, Roberts *et al.* 2008). The USEPA requires treatment systems capable of providing 4 log (99.99%) removal of viruses for all surface water sources (Agency 2006a) and groundwater sources with a history of contamination or other deficiencies (Agency 2006b).

Traditional chlorine disinfection, while highly effective for viral inactivation, produces harmful disinfection byproducts (DBPs) when organic compounds are present in the water. This has prompted stricter regulations concerning the acceptable levels of these compounds (Agency 2006c). Although UV disinfection has not been found to form DBPs (Liberti, Notarnicola *et al.* 2003), some viruses such as adenoviruses are highly resistant to UV disinfection (Yates, Malley *et al.* 2006). As a result, the USEPA has increased the UV fluence requirements for 4 log removal of viruses from 40 mJ/cm^2 to 186 mJ/cm^2(Agency 2006a). The new high fluence requirement significantly increases the energy demand, which translates into a higher treatment cost.

The employment of a highly efficient photocatalyst for advanced oxidation could potentially enable effective virus inactivation in drinking water as chlorine can while

limiting the formation of DBPs (Liu, Lim *et al.* 2008). It would also require less energy than UV disinfection. Therefore, photocatalytic oxidation is being actively researched as an alternative water disinfection method (Lydakis-Simantiris, Riga *et al.* 2010; Sordo, Van Grieken *et al.* 2010). A highly efficient photocatalyst could also be utilized for air treatment or as an antimicrobial coating.

Titanium dioxide photocatalysis

Titanium dioxide is an attractive photocatalyst for water treatment as it is resistant to corrosion and non toxic when ingested (Kaneko and Okura 2002). The basic mechanism of TiO_2 photoactivation and reactive oxygen species (ROS) generation is well known (Hoffmann, Martin *et al.* 1995).

There are currently a few commercial treatment systems that utilize TiO_2 photocatalysis (e.g. Wallenius AOT$^{(R)}$, Purifics$^{(R)}$). However their usage is not wide spread. One major reason for the limited application is the slow reaction kinetics as a consequence of charge recombination, which consumes the activated electrons and holes.

The antibacterial properties of TiO_2 have been well documented (Wei, Lin *et al.* 1994; Watts, Kong *et al.* 1995; Kikuchi, Sunada *et al.* 1997; Cho, Chung *et al.* 2005; Benabbou, Derriche *et al.* 2007; Page, Palgrave *et al.* 2007) and are attributed to the generation of ROS, especially hydroxyl free radicals ($HO^{\cdot}$) and hydrogen peroxide (H_2O_2) (Kikuchi, Sunada *et al.* 1997). While fewer studies have investigated the antiviral properties of TiO_2, its potential for inactivating viruses has been demonstrated (Watts, Kong *et al.* 1995; Belhacova, Krysa *et al.* 1999; Koizumi and Taya 2002; Cho, Chung *et al.* 2005). However, the inactivation rates obtained in most of these studies were

extremely low. For example, Cho *et al.* (2005) demonstrated only ~1 log removal of MS2 after 2 h of irradiation using P25 TiO_2 suspended at 1 g/L. The inactivation kinetics needs to be greatly improved in order to provide efficient drinking water disinfection.

Metal doping has been used to enhance TiO_2 photocatalysis by trapping excited electrons to prevent charge recombination (Mu, Herrmann *et al.* 1989; Choi, Termin *et al.* 1994; Haick and Paz 2003; Iliev, Tomova *et al.* 2006). Electron trapping can occur if the dopant has a lower Fermi level than the excited electron. Several metals including Fe, Mo, Ru, Os, Re, V, Rh, Au, Pt, and Ag have been shown to enhance TiO_2 performance. Silver in particular has been shown to enhance the photocatalytic efficiency of TiO_2 for both organic contaminant degradation and bacterial inactivation (Kondo and Jardim 1991; Vamathevan, Amal *et al.* 2002; Zhang, Yu *et al.* 2003; Xin, Jing *et al.* 2005; Page, Palgrave *et al.* 2007; Seery, George *et al.* 2007). Tran *et al.* (2006)showed selective enhancement by silver, which increased degradation rates for short chain carboxylic acids but not for alcohols or aromatics. Silver coatings above the optimum amount can also decrease the photocatalytic activity (Sclafani, Mozzanega *et al.* 1991; Sung-Suh, Choi *et al.* 2004). However, there is limited information on its impact on the antiviral capabilities of TiO2 (Kim, Cho *et al.* 2006). In addition to facilitating charge separation, silver is thought to enhance TiO_2 photocatalysis by directly interacting with microorganisms and providing more surface area for adsorption (Sclafani, Mozzanega *et al.* 1997; Sung-Suh, Choi *et al.* 2004), although Vamathevan *et al.* (2002)found no increase in BET surface area after silver doping. Silver ions and nanoparticles have been shown to have antimicrobial properties themselves through a variety of mechanisms

(Feng, Wu *et al.* 2000; Elechiguerra, Burt *et al.* 2005; Morones, Elechiguerra *et al.* 2005), which could also aid in bacterial or viral inactivation.

Utilizing silver in conjunction with TiO_2 photocatalysis could potentially allow several different inactivation mechanisms to work in concert. Therefore, it is possible that a synergism occurs between silver and TiO_2 when silver doped titanium dioxide is used for inactivating microorganisms under UV radiation. The study reported here demonstrated that silver doping TiO_2 greatly enhanced the photocatalytic inactivation of viruses primarily by increasing $HO^{\cdot}$ production in addition to slightly increasing virus adsorption.

Materials and methods

Synthesis and characterization of nano-silver doped TiO_2 (nAg/TiO_2)

nAg/TiO2 was prepared by depositing nano-sized silver islands via photochemical reduction of silver nitrate (Alfa Aesar) onto two commercially available TiO_2: Aeroxide TiO_2 P25 (denoted hereafter P25 TiO_2, Degussa) and Anatase TiO_2 (denoted hereafter $AATiO_2$, Alfa Aesar; CAS: 1317-70-0). A solution containing oxalic acid (Sigma-Aldrich, anhydrous 99%) as a sacrificial electron donor, TiO_2, and silver nitrate (Sigma-Aldrich, 99.9999%) was stirred for 2 h at pH 1 under ambient light at room temperature while purged with nitrogen gas. The solution was then irradiated with a germicidal UV lamp for one day and the product purified by washing with excessive water four times (Iliev, Tomova *et al.* 2006). The concentration of silver nitrate used in the reaction solution was varied to achieve 4, 8, and 10 wt.%; oxalic acid was added at a

25:1 acid to silver molar ratio. The $AATiO_2$ was doped using 10% $AgNO_3$ in solution. The doped particles were then dried and stored under vacuum in dark.

Samples were prepared for TEM and XPS analysis by applying a drop of a $nAgTiO_2$ suspension to a Silicon Monoxide/Formvar grid (Ted Pella; 01829) or a silicon wafer coated with gold (w68 nm). The grid was then used to analyze the sample in a JEOL 2100 field emission gun transmission electron microscope (JEM 2100F TEM) at 200 KV. The silicon wafer was used for x-ray photoelectron spectroscope (PHI Quantera XPS).

The actual silver content of the nAg/TiO_2 nanoparticles was determined by acid digestion and subsequent analysis of silver concentration using inductively coupled plasma optical emission spectroscopy (ICP-OES, PerkinElmer Optima 4300 DV). Aliquots of 0.01 g nAg/TiO_2 nanoparticles were mixed with 5 mL of 50% HNO_3, briefly bath sonicated, refluxed for 4 h and diluted to 50 mL with ultrapure water. The resulting suspensions were centrifuged and the supernatants filtered through a 0.22 mm-pore-size syringe filter. The filtrates were then analyzed by ICP-OES to determine the silver concentration.

Model virus

Bacteriophage MS2 (ATCC 15597-B1) was used as a model virus in this study due to its similarity to many waterborne pathogenic viruses (Koizumi and Taya 2002; Mackey, Hargy *et al.* 2002; Butkus, Labare *et al.* 2004) and the simplicity of its propagation and enumeration. MS2 has been found to be comparable or more resistant to chlorine and chloramines than Hepatitis A virus (Sobsey, Fuji *et al.* 1988) and Poliovirus

(Tree, Adams *et al.* 2003), and more resistant to UV disinfection than other bacteriophages (Sommer, Pribil *et al.* 2001). Hence, using MS2 as a virus surrogate provides conservative assessment on treatment efficiency.

The virus stock solution used in the disinfection procedures was obtained by infecting an incubation of the *E. Coli* host (ATCC 15597) with a liquid MS2 suspension. The mixture was mixed with a molten LB-Lennox (Fisher) medium containing 0.7% Bacto^{TM} agar (Difco Laboratories) and poured over a Petri dish containing solid LBeLennox media. After incubating overnight at 37 ^{o}C, sterile 0.1 M bicarbonate (Fisher) buffer was added to the plate which was gently rocked for 3 h. The solution was withdrawn from the plate, centrifuged, and the supernatant filtered through a 0.22 mM-pore-size PES syringe filter (Cho, Chung *et al.* 2005). The virus suspension contained ~7 x 10^{9} plaque forming units per milliliter (PFU/mL) and was stored at 4 ^{o}C before use.

MS2 samples were enumerated according to the double agar layer method (Adams 1959). Samples were analyzed either immediately or stored at 4 ^{o}C in dark and analyzed within 24 h. No change in viral titers was found within 24 h of storage in the presence or absence of the nanomaterials. To determine if the presence of nanoparticles interfered with virus enumeration, parallel samples containing nanoparticles were enumerated directly or after centrifugation at 10,900 x g for 15 min to remove the nanoparticles. No significant difference was found between the two methods. Therefore, all data reported hereafter were obtained from direct enumeration of the samples without removing the nanoparticles. Control tests consisted of enumerating buffer solution to ensure that viral contamination was not present in any of the reagents.

Virus inactivation experiments

All materials that came in contact with the virus solutions, media, and reagents were sterilized by autoclaving, filtering, or purchased sterile. Nanoparticle suspensions were freshly prepared in ultrapure water and were bath sonicated for 30-45 min to ensure good dispersion before each experiment. Particle size and zeta potential of each suspension was analyzed by dynamic light scattering (DLS) using a Zen 3600 Zetasizer (Malvern Instruments, Worcestershire, UK) to determine if differences in particle size and thus surface area were responsible for any observed differences in viral inactivation.

Dark inactivation of viruses

Dark inactivation of viruses was assessed using undoped P25 TiO_2 and nAg/TiO_2 synthesized with P25 and 10 wt.% $AgNO_3$. A suspension of ~7 x 10^7 PFU/mL MS2 was made in ultrapure water to which sonicated nAg/TiO_2 or P25 TiO_2 nanoparticles were added. The suspension was then stirred for up to 10 min in the dark, and sampled at different times for virus enumeration. The virus/nanoparticle mixtures were subsequently kept in dark at 4 ^oC for 24 h before enumerated again. The effect of leached silver was investigated by removing the catalyst particles from suspension after sonication by centrifugation and filtration. The resulting solution was added to an MS2 suspension, which was sampled periodically for the active MS2 titer.

Photocatalytic virus inactivation

The photocatalytic viral inactivation experiments were carried out in a pre-stabilized Luzchem LZC-4V photoreactor (Luzchem Research, Inc., Ottawa, ON Canada)

fitted with four 8 W UV-A (315-400 nm) lamps with peak emission at 350 nm (Hitachi). The total light intensity used in all experiments was 2.5 mW/cm^2 as determined by a UV radiometer (Control Company, Friendswood, TX) with a NIST traceable 350 nm photosensor.

Reactions were housed in sealed 25 mL Pyrex Erlenmeyer flasks. Sterile ultrapure water was combined with the MS2 stock solution and catalyst suspensions or leached Ag^+ solutions to achieve a final concentration of ~7 x 10^7 PFU/mL MS2 and 100 mg/L TiO_2 or nAg/TiO_2. The volume of leached Ag^+ solution added was the same as that used with particles in suspension. The mixture was stirred for 1 min in the dark, after which a sample was taken representing the initial virus concentration after adsorption. The reaction flask was then placed in the reactor and 1 mL samples were taken at 30 s intervals. All samples were immediately enumerated or covered and refrigerated at 4 ^oC to prevent further inactivation while waiting to be processed.

To investigate the role of $HO^{\cdot}$ in MS2 inactivation, reactions were carried out in the presence of two $HO^{\cdot}$ scavengers, methanol (99.9%, Fisher spectranalyzed) or tert-butanol (Fisher, ACS Certified) at concentrations from 30 to 400 mM. Control experiments were performed by mixing MS2 in the corresponding alcohol solution for 10 min to account for any inactivation due to the alcohol. Samples were immediately diluted into 0.1 M bicarbonate buffer.

Results and discussion

nAg/TiO2 characterization

The color of the dried nAg/TiO_2 nanoparticles varied from light brown to reddish brown. The degree of surface oxidation of the silver is likely responsible for the differences in color.

Silver content

The amount of silver captured by the TiO_2 varied with both the $AgNO_3$ concentration and the base TiO_2 material used. The P25 TiO_2 based nAg/TiO_2 made with 10, 8, and 4 wt.% AgNO3 had final Ag contents of 5.95, 4.36, and 2.46 wt.%. The $AATiO_2$ based nAg/TiO_2 made with 10 wt.% $AgNO_3$ had a final Ag content of 3.94 wt.%. The nAg/TiO_2 materials are hereafter designated by the final nAg content and base TiO_2 material (e.g. $5.95\%nAg/P25TiO_2$). Silver deposition was more efficient at higher $AgNO_3$ concentrations. Deposition onto P25 was notably greater than that on the $AATiO_2$: 90% of the Ag added was coated onto P25 while only 59% onto the $AATiO_2$ when 10% $AgNO_3$ was applied. The lower doping efficiency of $AATiO_2$ is attributed to its limited photoactivity.

TEM and XPS analyses

Fig. 1 presents representative TEM images of the Ag doped and undoped P25 samples. Silver islands of ~2-4 nm in diameter were found on the TiO_2 nanoparticles (~10-50 nm), although they were not apparent on all crystallites. No silver deposits were observed on any TiO_2 particles not treated with silver. XPS analyses showed similar results for all samples. Fig. 2 presents the XPS spectra for the $5.95\%nAg/P25TiO_2$ as an

example. O 1s spectra (e.g., Fig. 2a) of all samples showed a major peak with a broad shoulder in the area for metal oxides (528-531 eV). The presence of the shoulder indicates the presence of multiple metal oxides, i.e., titanium dioxide and silver oxide. The Ag 3d spectra (e.g., Fig. 2b) confirm the presence of silver oxide (peak range 367.3-368.0). This may be due to silver adsorbing on the TiO2 surface at oxygen sites or the oxidation of the surface of the deposited silver.

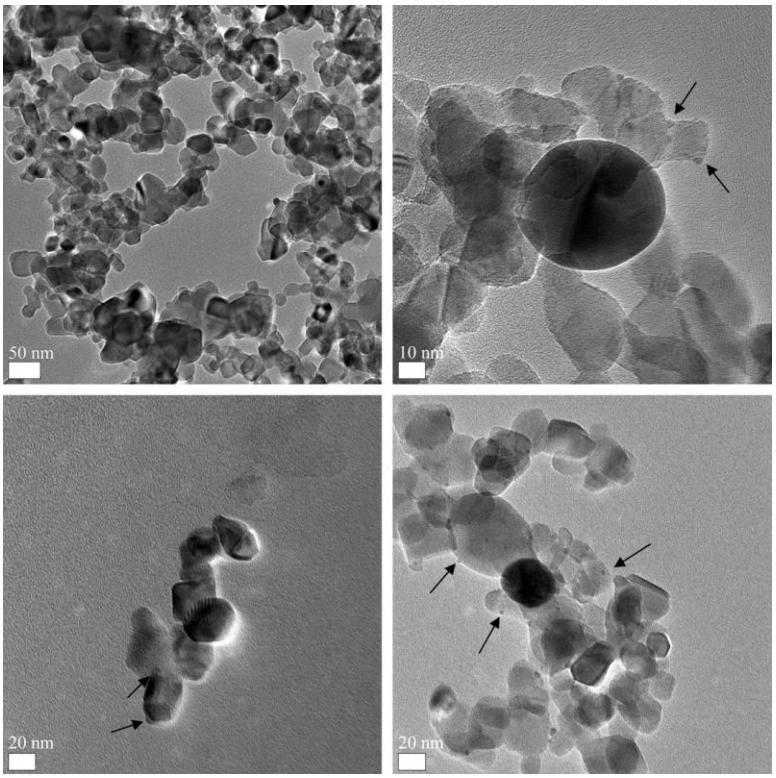

Fig. 1 TEM images of nAg/P25TiO_2 with silver particles (~2-4 nm dia.) indicated by arrows. Silver particles are visible on all doped samples, although they are not apparent on all TiO_2 crystallites (10-50 nm dia.). **Top left** undoped P25 (50 nm scale), **top right** 5.95% Ag (10 nm scale), **bottom left** 4.36% Ag (20 nm scale), **bottom right** 2.46% Ag (20 nm scale).

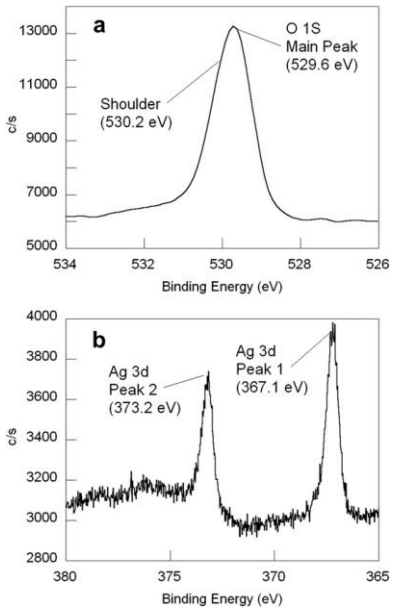

Fig. 2 Typical X-ray photoelectron spectra of **(a)** O 1s, which reveals the presence of multiple metal oxides through the observed peak shoulder and **(b)** Ag 3d, with peak between 367.3 and 368 eV which corresponds to silver oxide. Spectra shown for 5.95%nAg/P25TiO_2.

Dispersed particle size

Mean hydrodynamic diameters of all photocatalyst suspensions in ultrapure water are presented in Fig. 3. The sizes of P25 TiO_2, $AATiO_2$, and 3.94%nAg/$AATiO_2$ stayed constant for at least 25 min, suggesting that these suspensions were stable during the virus inactivation experiments (~5 min). All the P25 based nAg/TiO_2 materials, however, formed large aggregates and settled out gradually. The aggregation of the silver doped samples was consistent with the measured changes in zeta potential: -9.1 to -9.3 mV versus ~38.7 mV for P25. The sizes presented in Fig. 3 for these materials are the average of data obtained in the first 5 min concurrent with the inactivation procedure.

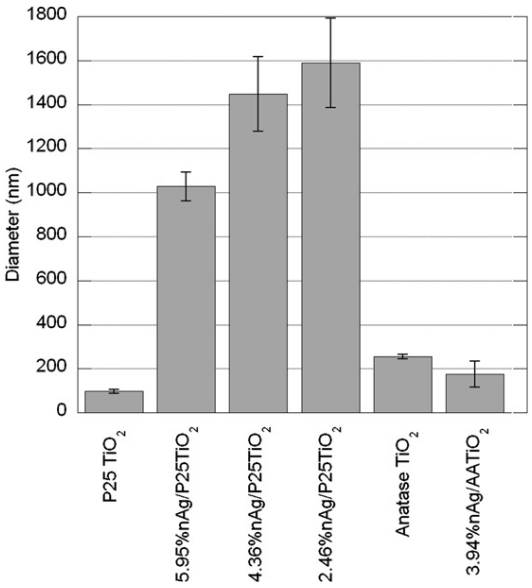

Fig. 3 Dispersed particle diameters of nanoparticles used for virus inactivation as measured by DLS. Silver doping P25 TiO_2 was found to decrease the stability of the suspended particles, resulting in the observed aggregation.

MS2 dark inactivation

Inactivation and removal of MS2 by the photocatalysts in dark (referred to as dark inactivation hereafter) is attributed to adsorption to the photocatalyst particles and inactivation by Ag^+ released from nAg/TiO_2. Fig. 4 shows the total dark removal after 10 min of exposure to P25 and 5.95%$nAg/P25TiO_2$. Leached Ag^+ was responsible for 37% (0.2 log) MS2 inactivation, with most inactivation occurring during the first 1 min of exposure. When enumerated with catalyst particles in suspension, a total of 75% (0.6 log) removal was observed with 5.95%$nAg/P25TiO_2$. After accounting for the effect of leached Ag^+ (37% removal), the 5.95%nAg/TiO_2 removed 38% (0.2 log) of the MS2 by adsorption, 12% more than that adsorbed by undoped P25, which inactivated 26% (0.13 log) of the MS2. The majority of dark inactivation occurred during the first minute of exposure. Therefore, the MS2 concentration measured after 1 min of dark contact in each photocatalytic inactivation experiment was used as the initial concentration for analysis of the photocatalytic inactivation data.

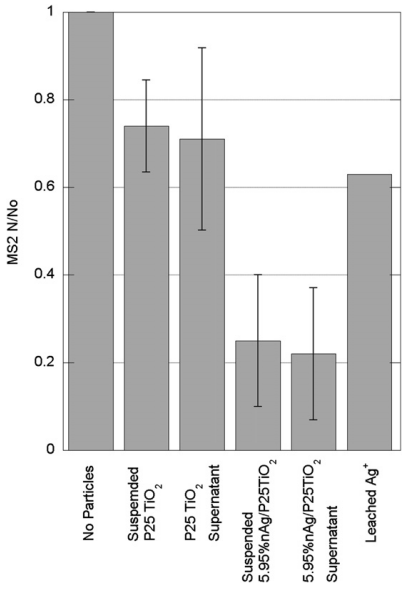

Fig. 4 Removal of MS2 by P25 TiO_2, 5.95% $nAg/P25TiO_2$, and leached Ag^+ from 5.95% $nAg/P25TiO_2$ after 10 min of contact in dark. TiO_2 and nAg/TiO_2 samples were enumerated both with particles in suspension and after their removal by centrifugation (data marked "supernatant") to determine if adsorbed viruses remained infective. The limited difference in virus titers between solutions with particles suspended and removed suggests that MS2 is inactivated upon adsorption to the catalysts. After accounting for the effect of leached Ag^+, the 5.95% $nAg/P25TiO_2$ removed 38% MS2 by adsorption as compared to only 26% by P25 TiO_2.

The increased adsorptive removal by nAg/TiO2 may be explained by interactions of viral surface amino acids with silver. Silver has a high affinity for sulfur moieties, and there are 183 cysteine residues exposed on the MS2 capsid surface (Jou, Ysebaert *et al.* 1972; Nolf, Vandekerckhove *et al.* 1977; Penrod, Olson *et al.* 1996). Carboxyl groups on the amino acids are also known to interact with silver (Stewart and Fredericks 1999). The minimum difference between virus titers with nanoparticles in suspension and nanoparticle free centrifuge supernatant (Fig. 4) suggests that adsorption of MS2 to the nAg/TiO_2 or undoped TiO_2 surface either inactivates these viruses or sterically inhibits access of the MS2 A protein to the *E. Coli* pili, where infection occurs. The limited additional removal observed after centrifugation of samples is attributed to the interception of MS2 by the catalyst particles during centrifugation.

The mixtures of the MS2 and the P25 TiO_2 or 5.95% $nAg/P25TiO_2$ were further kept in dark at 4 ^oC for 24 h and re-enumerated to assess the potential dark inactivation of

stored samples. Negligible change in virus titer was observed during the 24 h period for either materials (data not shown), suggesting that further inactivation was absent in dark.

Photocatalytic MS2 inactivation

The inactivation of MS2 by the different nanomaterials and UV-A alone is shown in Fig. 5. The plain P25 TiO_2 achieved 1.6 log inactivation of MS2 in 2 min while UV-A irradiation alone showed negligible MS2 removal within the same time period (Fig. 5a), showing that the inactivation in the presence of P25 TiO_2 is attributed to photocatalytic oxidation. Silver doping significantly enhanced MS2 inactivation by P25 TiO_2 and the inactivation rate increased with silver content. The enhanced inactivation was also observed with the Ag doped $AATiO_2$ (Fig. 5b), even though $AATiO_2$ showed minimum inactivation.

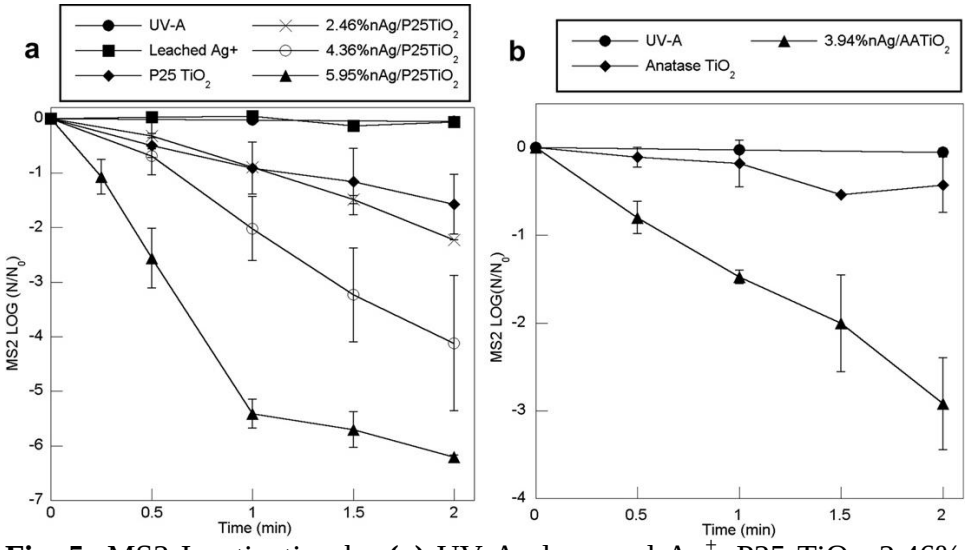

Fig. 5 MS2 Inactivation by **(a)** UV-A alone and Ag^+, P25 TiO_2, 2.46% nAg/P25TiO_2, 4.36% nAg/P25TiO_2, and 5.95% nAg/P25TiO_2 under UV-A irradiation, and by **(b)** UV-A alone and, $AATiO_2$, 3.94% nAg/$AATiO_2$ under UV-A irradiation. The inactivation rate was found to increase along with the silver content on P25 TiO_2 up to the maximum amount tested (5.95%). 3.94% nAg on anatase TiO_2 also dramatically increased the inactivation rate.

The photocatalytic inactivation kinetics data could be described by the Chick-Watson model (Equation (1)), where k is the rate constant (s^{-1}) and N_0 and N are the titer of active viruses at time zero and t. Here, the virus titer after dark adsorption equilibrium was used as N_0.

$$log\left(\frac{N}{N_0}\right) = -kt$$

The inactivation rate constants obtained from fitting the kinetics data with the Chick-Watson model are shown in Table 1. The silver doping increased the reaction rate constant by up to 584% as compared to the base TiO_2. The inactivation rate was found to increase with the silver content on P25 TiO_2, with rate constants of 0.089, 0.035, 0.017 and 0.013 s^{-1}, for the materials with 5.95, 4.36, 2.46 and 0% silver, respectively. The inactivation rate constant for 3.94% nAg/$AATiO_2$ (0.024 s^{-1}) showed a 5 fold increase from the plain $AATiO_2$ (0.004 s^{-1}); it also outperformed P25 TiO_2 and 2.46% nAg/$P25TiO_2$, even though the P25 TiO_2 inactivated MS2 ~3.2 times faster than the $AATiO_2$. While silver was found to be beneficial when doped onto P25 TiO_2, the increased aggregate size may have offset some enhancement in photoactivity. Also shown in Table 1 is the time required for each nanomaterial to achieve 4 log removal of MS2. With 5.95 wt.% nAg loading on P25, 4 log removal of MS2 could be obtained in 45 s, making it feasible to achieve virus removal from drinking water using a small photoreactor or to improve removal of UV resistant viruses of existing UV reactors.

Table 1 – Actual silver contents on nAg/TiO_2 particles and first order rate constants for MS2 inactivation.

Material	Rate Constant (s^{-1})	R^2	Time Required to Achieve 4 Log Removal (min)[a]
P25 TiO_2	0.013	0.91	5.1
2.46%nAg/P25TiO_2	0.017	0.99	3.9
4.36%nAg/P25TiO_2	0.035	0.97	1.9
5.95%nAg/P25TiO_2	0.089[b]	0.99	0.75
AATiO_2	0.004	0.98	16.7
3.94%nAg/AATiO_2	0.024	0.99	2.8

a Times greater than 2 min obtained by projecting kinetic data.
b Rate for first 60 s of inactivation.

Experiments using solutions containing leached Ag^+ resulted in no notable photocatalytic inactivation. These results suggest that the enhanced inactivation was due to the increase in the photocatalytic activity of TiO_2 instead of the antimicrobial property of nAg. Two mechanisms may be responsible for such enhancement: increased MS2 adsorption and greater ROS generation. MS2 inactivation has been shown to be directly proportional to the amount adsorbed to the TiO_2 surface (Koizumi and Taya 2002). Increased adsorption as demonstrated in Fig. 4 may enhance the inactivation rate by placing the virus in close proximity to newly generated $HO^{\cdot}$(both surface bound and bulk) and may increase direct hole oxidation. In addition, silver doping has been proposed to facilitate charge separation in TiO_2 resulting in more efficient ROS generation and consequently greater MS2 inactivation.

MS2 inactivation by 5.95% nAg/P25TiO_2 shows a tailing effect after 60 s (5.4 log removal), when the inactivation rate constant decreased from 0.089 to 0.013. This was not observed when MS2 was inactivated by the other materials. This is likely due to the presence of the large number of inactivated viruses and their remnants, which compete with infective viruses for adsorption sites and ROS, since 99.9996% of the MS2 had been inactivated after 60 s.

Effects of $HO^{\cdot}$ scavengers

As discussed above, one potential mechanism for the enhanced virus inactivation of nAg/TiO_2 is higher $HO^{\cdot}$ production rate. To test this mechanism, methanol and tertbutanol were employed to elucidate the role of Ag doping in $HO^{\cdot}$ production and MS2 inactivation. Alcohols, especially methanol and t-butanol, are known $HO^{\cdot}$ scavengers. Methanol was reported to scavenge both surface bound and bulk $HO^{\cdot}$, as well as holes (Cho, Chung *et al.* 2005). While t-butanol has been shown to competitively adsorb to TiO_2 (Sun and Pignatello 1995), research has demonstrated that it does not scavenge all surface bound $HO^{\cdot}$ (Kim and Choi 2002). Using methanol and t-butanol as $HO^{\cdot}$ scavengers, Cho *et al.* (2005) showed that bulk $HO^{\cdot}$ was responsible for the inactivation of MS2 by TiO_2. Singlet oxygen and superoxide anion were also found to inactivate MS2 in a study using fullerol as the photocatalyst (Badireddy, Hotze *et al.* 2007).

Experiments were performed using P25 TiO_2 (Fig. 6a,b) and 5.95% nAg/P25TiO_2 (Fig. 6c,d) at different methanol or t-butanol concentrations. Both methanol and t-butanol completely stopped inactivation of MS2 by the plain P25 TiO_2 at 400 mM and considerably slowed the reaction at 200 mM. P25 TiO_2 showed higher sensitivity to t-butanol, as 30 and 100 mM t-butanol both decreased the inactivation rate while the same concentrations of methanol had no effect. Control experiments using methanol or t-butanol in the absence of any photocatalyst did not show any decrease in virus titer for methanol or t-butanol concentrations up to 400 mM. These results suggest that $HO^{\cdot}$ is primarily responsible for MS2 inactivation by P25 TiO_2. Although singlet oxygen and superoxide anions are also produced by TiO_2 (Hoffmann, Martin *et al.* 1995), they did not seem to cause notable MS2 inactivation in our study. Because there was no

significant difference in reaction rates when either methanol or t-butanol was used at 400mM and the inactivation rate was more sensitive to low t-butanol concentrations, the data suggests that bulk $HO^{\cdot}$ plays a more important role than surface bound $HO^{\cdot}$ in MS2 inactivation. This observation agrees with the conclusion by Cho *et al.* (2005).

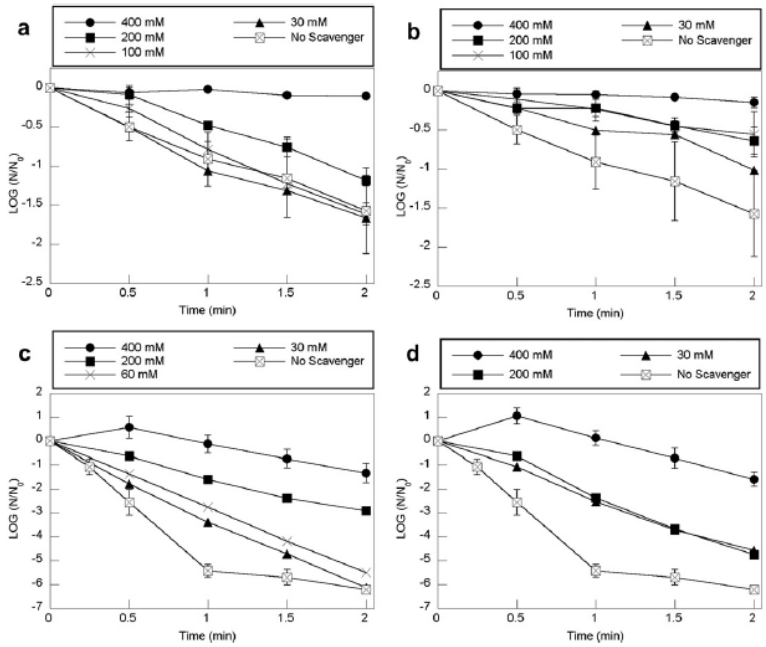

Fig. 6 MS2 inactivation in the presence of $HO^{\cdot}$ scavengers methanol and t-butanol. **(a)** P25 TiO_2 with methanol; **(b)** P25 TiO_2 with t-butanol; **(c)** 5.95% nAg/P25TiO_2 with methanol; **(d)** 5.95% nAg/P25TiO_2 with t-BuOH. The inactivation rate was found to decrease in a concentration dependent manner when either alcohol was applied. When present at 400 mM, both alcohols completely stopped MS2 inactivation by P25 TiO_2 while inactivation still occurred by 5.95% nAg/P25TiO_2, but to a much lesser degree than the case when no $HO^{\cdot}$ scavenger is applied. Dark inactivation of MS2 by 5.95% nAg/P25TiO_2 was enhanced when either alcohol was present at 400 mM, but the effect was reversed after 30 s of irradiation corresponding to the apparent initial rise in active virus titer.

Both alcohols also reduced the inactivation rate of MS2 by 5.95% nAg/P25TiO_2, but to a much less extent. With 400 mM methanol or t-butanol, 1.3 and 1.6 log of MS2 inactivation was achieved, respectively, suggesting that silver doping increases $HO^{\cdot}$

production and consequently MS2 inactivation. When nAg/TiO_2 was used with 400 mM of either alcohol, the amount of viruses removed by dark stirring was greater than that observed without added alcohol (90-98%, data not shown). The active virus titer increased after 30 s of irradiation compared to that before UV exposure. Since the depression of initial virus concentration was not observed with undoped P25 TiO_2, this effect is attributed to the interaction of the alcohol with the silver and the subsequent changes in viral adsorption capacity. Any increased adsorption of alcohol to silver/silver oxide as compared to TiO_2 could change the electrostatic and/or hydrophilic properties of the catalyst, resulting in changes to its adsorptive capacity. From 30 s to 2 min, the MS2 was slowly inactivated. The inactivation rate by nAg/TiO_2 was observed to be influenced by both alcohols in a concentration dependent manner, confirming the role of $HO^{\cdot}$ in MS inactivation.

Conclusion

This study demonstrated that silver doping TiO_2 nanoparticles is an effective way to increase TiO_2 photocatalytic activity for virus inactivation. Silver doping enhances photocatalytic inactivation of viruses primarily by increasing $HO^{\cdot}$ production, although increased virus adsorption to silver sites and leaching of antimicrobial Ag^{+} also contribute to virus removal. The fast virus inactivation kinetics of the nAg/TiO_2 materials demonstrated in our study suggest that effective virus inactivation can be achieved using a small photoreactor and photocatalytic disinfection of drinking water at both point of use and municipality scales could be a potential application of the nAg/TiO_2 materials. Further research is needed to address issues such as photocatalyst fouling,

impact of water quality, loss of silver, and need for catalyst regeneration to ensure the sustainability of the technology. Very importantly, the retention of the nAg/TiO_2 materials in the treatment system is critical. This can be achieved by using a hybrid photoreactor/membrane system, where the photocatalyst is retained by a membrane unit down-stream of the photoreactor and recirculated, or by applying the photocatalyst as a coating on surfaces inside a photoreactor. Because UV-A is a significant component of the solar irradiation that reaches earth surface, coating transparent piping or shallow open channels with the photocatalyst at sunny locations could also be a low-cost solution to drinking water disinfection. Ag/TiO_2 may also be activated by visible light through the silver surface plasmon resonance, however it is not clear how the catalyst will behave under both UV and visible radiation (Sung-Suh, Choi *et al.* 2004; Seery, George *et al.* 2007).

References

Abbaszadegan, M., M. Lechevallier, *et al.* (2003)."Occurrence of viruses in US groundwaters."Journal American Water Works Association 95(9): 107-120.

Adams, M. H. (1959). Bacteriophages. New York, Interscience Publishers, Inc.

Agency, E. P. (2006a). National Primary Drinking Water Regulations: Long Term 2 Enhanced Surface Water Treatment Rule; Final Rule, Federal Register. 40: 654-786.

Agency, E. P. (2006b). National Primary Drinking Water Regulations: Ground Water Rule; Final Rule. Federal Register, Federal Register. 40: 65574-65659.

Agency, E. P. (2006c). National Primary Drinking Water Regulations: Stage 2 Disinfectants and Disinfection Byproducts Rule; Final Rule, Federal Register. 40: 387-493.

Badireddy, A. R., E. M. Hotze, *et al.* (2007). "Inactivation of Bacteriophages via photosensitization of fullerol nanoparticles."Environmental Science &Technology 41(18): 6627-6632.

Belhacova, L., J. Krysa, *et al.* (1999). "Inactivation of microorganisms in a flow-through photoreactor with an immobilized TiO_2 layer."Journal of Chemical Technology and Biotechnology 74(2): 149-154.

Benabbou, A. K., Z. Derriche, *et al.* (2007). "Photocatalytic inactivation of Escherischia coli - Effect of concentration of TiO_2 and microorganism, nature, and intensity of UV irradiation."Applied Catalysis B-Environmental 76(3-4): 257-263.

Butkus, M. A., M. P. Labare, *et al.* (2004). "Use of aqueous silver to enhance inactivation of coliphage MS-2 by UV disinfection."Applied and Environmental Microbiology 70(5): 2848-2853.

Cho, M., H. M. Chung, *et al.* (2005)."Different inactivation Behaviors of MS-2 phage and Escherichia coli in TiO_2 photocatalytic disinfection."Applied and Environmental Microbiology 71(1): 270-275.

Choi, W. Y., A. Termin, *et al.* (1994)."The Role of Metal-Ion Dopants in Quantum-Sized TiO_2 - Correlation between Photoreactivity and Charge-Carrier Recombination Dynamics."Journal of Physical Chemistry 98(51): 13669-13679.

Elechiguerra, J. L., J. L. Burt, *et al.* (2005). "Interaction of silver nanoparticles with HIV-1."Journal of Nanobiotechnology 3(6).

Feng, Q. L., J. Wu, *et al.* (2000). "A mechanistic study of the antibacterial effect of silver ions on Escherichia coli and Staphylococcus aureus."Journal of Biomedical Materials Research 52(4): 662-668.

Haick, H. and Y. Paz (2003)."Long-range effects of noble metals on the photocatalytic properties of titanium dioxide."Journal of Physical Chemistry B 107(10): 2319-2326.

Hamza, I. A., L. Jurzik, *et al.* (2009). "Detection of human viruses in rivers of a densly-populated area in Germany using a virus adsorption elution method optimized for PCR analyses." Water Research 43(10): 2657-2668.

Hoffmann, M. R., S. T. Martin, *et al.* (1995). "Environmental Applications of Semiconductor Photocatalysis."Chemical Reviews 95(1): 69-96.

Iliev, V., D. Tomova, *et al.* (2006). "Photocatalytic properties of TiO_2 modified with platinum and silver nanoparticles in the degradation of oxalic acid in aqueous solution." Applied Catalysis B-Environmental 63(3-4): 266-271.

Jou, W. M., M. Ysebaert, *et al.* (1972). "Nucleotide sequence of gene coding for bacteriophage MS2 coat protein."Nature 237(5350): 82-88.

Kaneko, M. and I. E. Okura, Eds. (2002). Photocatalysis: Science and Technology. New York, Springer.

Kikuchi, Y., K. Sunada, *et al.* (1997). "Photocatalytic bactericidal effect of TiO_2 thin films: Dynamic view of the active oxygen species responsible for the effect." Journal of Photochemistry and Photobiology a-Chemistry 106(1-3): 51-56.

Kim, J.-P., I.-H.Cho, *et al.* (2006)."Manufacturing of anti-viral inorganic materials from colloidal silver and titanium oxide."Revue Roumaine De Chimie 51(11): 1121-+.

Kim, S. and W. Choi (2002). "Kinetics and mechanisms of photocatalytic degradation of (CH3)(n)NH4-n+ ($0 <= n <= 4$) in TiO_2 suspension: The role of OH radicals." Environmental Science &Technology 36(9): 2019-2025.

Koizumi, Y. and M. Taya (2002). "Kinetic evaluation of biocidal activity of titanium dioxide against phage MS2 considering interaction between the phage and photocatalyst particles." Biochemical Engineering Journal 12(2): 107-116.

Kondo, M. M. and W. F. Jardim (1991)."Photodegradation of Chloroform and Urea Using Ag-Loaded Titanium Diode as Catalyst."Water Research 25(7): 823-827.

Liang, J. L., E. J. Dziuban, *et al.* (2006). "Surveillance for Waterborne Disease and Outbreaks Associated with Drinking Water and Water not Intended for Drinking -- United States, 2003--2004." Surveillance Summaries 55(SS12): 31-58.

Liberti, L., M. Notarnicola, *et al.* (2003). "Advanced treatment for municipal wastewater reuse in agriculture. UV disinfection: parasite removal and by-product formation." Desalination 152(1-3): 315-324.

Liu, S., M. Lim, *et al.* (2008). "TiO_2 photocatalysis of natural organic matter in surface water: impact on trihalomethane and haloacetic acid formation potential." Environmental Science &Technology 42(16): 6218-6223.

Lydakis-Simantiris, N., D. Riga, *et al.* (2010)."Disinfection of spring water and secondary treated municipal wastewater by TiO_2 photocatalysis."Desalination 250(1): 351-355.

Mackey, E. D., T. M. Hargy, *et al.* (2002). "Comparing Cryptosporidium and MS2 bioassays - implications for UV REACTOR validation."Journal American Water Works Association 94(2): 62-69.

Morones, J. R., J. L. Elechiguerra, *et al.* (2005). "The bactericidal effect of silver nanoparticles."Nanotechnology 16(10): 2346-2353.

Mu, W., J. M. Herrmann, *et al.* (1989)."Room-Temperature Photocatalytic Oxidation of Liquid Cyclohexane into Cyclohexanone over Neat and Modified TiO_2."Catalysis Letters 3(1): 73-84.

Nolf, F. A., J. S. Vandekerckhove, *et al.* (1977). "Sequence of A-protein of coliphage-MS2.1. Isolation of A-protein, determination of NH2-terminal and COOH-terminal sequences, isolation and amino-acid sequence of tryptic peptides."Journal of Biological Chemistry 252(21): 7752-7760.

Page, K., R. G. Palgrave, *et al.* (2007)."Titania and silver-titania composite films on glass-potent antimicrobial coatings."Journal of Materials Chemistry 17(1): 95-104.

Penrod, S. L., T. M. Olson, *et al.* (1996). "Deposition kinetics of two viruses in packed beds of quartz granular media." Langmuir 12(23): 5576-5587.

Sclafani, A., M. N. Mozzanega, *et al.* (1997). "Influence of silver deposits on the photocatalytic activity of titania." Journal of Catalysis 168(1): 117-120.

Sclafani, A., M. N. Mozzanega, *et al.* (1991). "Effect of Silver Deposits on the Photocatalytic Activity of Titanium-Dioxide Samples for the Dehydrogenation or Oxidation of 2-Propanol."Journal of Photochemistry and Photobiology a-Chemistry 59(2): 181-189.

Seery, M. K., R. George, *et al.* (2007). "Silver doped titanium dioxide nanomaterials for enhanced visible light photocatalysis." Journal of Photochemistry and Photobiology a-Chemistry 189(2-3): 258-263.

Sobsey, M. D., T. Fuji, *et al.* (1988). "Inactivation of Hepatitis-a Virus and Model Viruses in Water by Free Chlorine and Monochloramine."Water Science and Technology 20(11-12): 385-391.

Sommer, R., W. Pribil, *et al.* (2001). "Inactivation of bacteriophages in water by means of non-ionizing (UV-253.7 nm) and ionizing (gamma) radiation: A comparative approach." Water Research 35(13): 3109-3116.

Sordo, C., R. Van Grieken, *et al.* (2010). "Solar photocatalytic disinfection with immobilised TiO_2 at pilot-plant scale."Water Science and Technology 61(2): 507-512.

Stewart, S. and P. M. Fredericks (1999)."Surface-enhanced Raman spectroscopy of peptides and proteins adsorbed on an electrochemically prepared silver surface."Spectrochimica Acta Part a-Molecular and Biomolecular Spectroscopy 55(7-8): 1615-1640.

Sun, Y. F. and J. J. Pignatello (1995). "Evidence for a Surface Dual Hole - Radical Mechanism in the TiO_2 Photocatalytic Oxidation of 2,4-Dichlorophenaxyacetic Acid." Environmental Science &Technology 29(8): 2065-2072.

Sung-Suh, H. M., J. R. Choi, *et al.* (2004). "Comparison of Ag deposition effects on the photocatalytic activity of nanoparticulate TiO_2 under visible and UV light irradiation." Journal of Photochemistry and Photobiology a-Chemistry 163(1-2): 37-44.

Tree, J. A., M. R. Adams, *et al.* (2003)."Chlorination of indicator bacteria and viruses in primary sewage effluent."Applied and Environmental Microbiology 69(4): 2038-2043.

Vamathevan, V., R. Amal, *et al.* (2002)."Photocatalytic oxidation of organics in water using pure and silver-modified titanium dioxide particles."Journal of Photochemistry and Photobiology a-Chemistry 148(1-3): 233-245.

Watts, R. J., S. H. Kong, *et al.* (1995). "Photocatalytic Inactivation of Coliform Bacteria and Viruses in Secondary Waste-Water Effluent."Water Research 29(1): 95-100.

Wei, C., W. Y. Lin, *et al.* (1994). "Bactericidal Activity of TiO_2 Photocatalyst in Aqueous-Media - toward a Solar-Assisted Water Disinfection System."Environmental Science &Technology 28(5): 934-938.

Wong, M., L. Kumar, *et al.* (2009). "Evaluation of public health risks at recreational beaches in Lake Michigan via detection of enteric viruses and a human-specific bacteriological marker." Water Research 43(4): 1137-1149.

Xin, B. F., L. Q. Jing, *et al.* (2005). "Effects of simultaneously doped and deposited ag on the photocatalytic activity and surface states of TiO_2."Journal of Physical Chemistry B 109(7): 2805-2809.

Yates, M. V., J. Malley, *et al.* (2006). "Effect of adenovirus resistance on UV disinfection requirements: A report on the state of adenovirus science." Journal American Water Works Association 98(6): 93-106.

Yoder, J., V. Roberts, *et al.* (2008). "Surveillance for Waterborne Disease and Outbreaks Associated with Drinking Water and Water not Intended for Drinking --- United States, 2005--2006." Surveillance Summaries 57(SS09): 39-62.

Zhang, L. Z., J. C. Yu, *et al.* (2003). "Ambient light reduction strategy to synthesize silver nanoparticles and silver-coated TiO_2 with enhanced photocatalytic and bactericidal activities." Langmuir 19(24): 10372-10380.

APPENDIX 2: ALTERING PROTEIN SURFACE CHARGE WITH CHEMICAL MODIFICATION MODULATES PROTEIN–GOLD NANOPARTICLE AGGREGATION

Altering protein surface charge with chemical modification modulates protein–gold nanoparticle aggregation

Jennifer A. Jamison• Erika L. Bryant• Shyam B. Kadali• Michael S. Wong• Vicki L. Colvin• Kathleen S. Matthews• Michelle K. Calabretta

Journal of Nanopaticle Research 13(2), 625-636

J. A. Jamison; K. S. Matthews; M. K. Calabretta
Department of Biochemistry and Cell Biology
Rice University, 6100 S. Main Street,
Houston, TX 77005, USA
e-mail: jaj@alumni.rice.edu
K. S. Matthews
e-mail: ksm@rice.edu
M. K. Calabretta
e-mail: michelle.calabretta@gmail.com

E. L. Bryant; M. S. Wong; V. L. Colvin
Department of Chemistry,
Rice University
6100 S. Main Street, Houston, TX 77005, USA

S. B. Kadali; M. S. Wong
Department of Chemical and Biomolecular Engineering
Rice University, 6100 S. Main Street
Houston, TX 77005, USA

Abstract

Gold nanoparticles (AuNP) can interact with a wide range of molecules including proteins. Whereas significant attention has focused on modifying the nanoparticle surface to regulate protein– AuNP assembly or influence the formation of the protein ‘‘corona,’’ modification of the protein surface as a mechanism to modulate protein–AuNP interaction has been less explored. Here, we examine this possibility utilizing three small globular proteins— lysozyme with high isoelectric point (pI) and established interactions with AuNP; α-lactalbumin with similar tertiary fold to lysozyme but low pI; and myoglobin with a different globular fold and an intermediate pI. We first chemically modified these proteins to alter their charged surface functionalities, and thereby shift protein pI, and

then applied multiple methods to assess protein–AuNP assembly. At pH values lower than the anticipated pI of the modified protein, AuNP exposure elicits changes in the optical absorbance of the protein–NP solutions and other properties due to aggregate formation. Above the expected pI, however, protein–AuNP interaction is minimal, and both components remain isolated, presumably because both species are negatively charged. These data demonstrate that protein modification provides a powerful tool for modulating whether nanoparticle–protein interactions result in material aggregation. The results also underscore that naturally occurring protein modifications found in vivo may be critical in defining nanoparticle–protein corona compositions.

Keywords Gold nanoparticles, Chemical modification, Nanoparticle–protein interactions, Aggregation, Protein modification, Nanobiotechnology

Proteins interact with nanoparticles to generate conjugates that can either remain in suspension or assemble into complex, three-dimensional nanoarchitectures. Both forms can exhibit properties that differ from the discrete nanoparticle and protein in solution e.g., (Deroe, Courtoy *et al.* 1987; Baudhuin, Van der Smissen *et al.* 1989; Srivastava, Verma *et al.* 2005; Asuri, Bale *et al.* 2006; Ofir, Samanta *et al.* 2008; Iosin, Toderas *et al.* 2009; Lim and Zhong 2009; Nel, Maedler *et al.* 2009; Roecker, Poetzl *et al.* 2009; Wang and Ma 2009). Indeed, this facile interaction can limit use of nanoparticles in biological systems, where the protein ‘‘corona’’ formed on exposure to biological media[1]exerts a strong influence on the fate and impact of the nanoparticle (Lacerda, Park *et al.*; Cedervall, Lynch *et al.* 2007; Lynch, Cedervall *et al.* 2007; Lundqvist, Stigler *et al.* 2008; Lynch and Dawson 2008; Aggarwal, Hall *et al.* 2009; Lynch, Salvati *et al.* 2009; Nel, Maedler *et al.* 2009). Whereas mechanisms to modify nanoparticles to enhance (or diminish) aggregation have been widely explored, less attention has been devoted to strategies that alter protein properties to modulate aggregation (e.g., (Hu, Qian *et al.* 2007; You, Chompoosor *et al.* 2007; Lu, Chen *et al.* 2008; Nel, Maedler *et al.* 2009; Wang and Ma 2009)

Citrate-stabilized gold nanoparticles (AuNPs) are non-toxic, well-characterized, and easy to synthesize in a broad range of sizes(Frens 1973). These materials undergo an easily detectable color change and other spectral and electrochemical alterations when

[1]The protein ‘‘corona’’ is the wide range of proteins that bind to nanoparticles exposed to biological fluids. These proteins become the ‘‘exposed’’ surface of the nanoparticle and alter its properties in the biological system

aggregated by ionic salts as well as by small molecules or proteins that present significant positive charge e.g., (Deroe, Courtoy *et al.* 1987; Baudhuin, Van der Smissen *et al.* 1989; Nakata, Kido *et al.* 1996; Keating, Kovaleski *et al.* 1998; Brewer, Glomm *et al.* 2005; Jiang, Jiang *et al.* 2005; Iosin, Toderas *et al.* 2009; Laaksonen, Kivioja *et al.* 2009). These properties have resulted in wide use in biological systems on the one hand (Baudhuin, Van der Smissen *et al.* 1989; Nel, Maedler *et al.* 2009; Wang and Ma 2009) and in biomolecule-mediated aggregation on the other (Srivastava, Verma *et al.* 2005; Asuri, Bale *et al.* 2006; Ofir, Samanta *et al.* 2008; Iosin, Toderas *et al.* 2009; Lim and Zhong 2009; Nel, Maedler *et al.* 2009; Roecker, Poetzl *et al.* 2009; Wang and Ma 2009). Indeed, the ubiquitous presence of the protein corona around nanoparticles in cells reflects this facile association, and analysis of nanoparticles associated with proteins under different conditions has provided insights relevant to medical and other applications (Lacerda, Park *et al.*; Lynch, Cedervall *et al.* 2007; Lundqvist, Stigler *et al.* 2008; Aggarwal, Hall *et al.* 2009).

A comprehensive study of bovine serum albumin adsorption to citrate-stabilized AuNPs concluded that, as anticipated, non-specific protein–AuNP interactions are primarily due to salt bridges between citrate and lysine side chains (Deroe, Courtoy *et al.* 1987; Brewer, Glomm *et al.* 2005). Previous studies have demonstrated that citrate-stabilized AuNPs aggregate in the presence of lysozyme at a solution pH below its isoelectric point (pI) of 11.5 (Yang, Li *et al.* 2007), presumably due to the prevalence of positive charges on the protein surface. Further, lysozyme has been shown to form aggregates below its pI at neutral pH in the presence of larger AuNPs without surface

modification, with consequent distortions in the structure of the protein (Zhang, Neumann *et al.* 2009).

In this study, we explore the impact on interactions with citrate-stabilized AuNPs by altering the surface character of our target proteins: lysozyme, α-lactalbumin, and myoglobin. Lysozyme is a 14 kDa globular protein with a pI of ~11.5 that has been used in forming aggregate structures with AuNP (Yang *et al.* 2007;Verma *et al.* 2005). α-Lactalbumin is of similar molecular weight and highly homologous to lysozyme in its three-dimensional structure but has a much lower pI at 4.5 (Acharya *et al.* 1989) and would therefore be expected to interact differently with the negatively charged surface of citrate- stabilized AuNP than lysozyme. Myoglobin, with a molecular weight of 17 kDa, is similar in its globular nature to lysozyme and α-lactalbumin, but this protein has an intermediate pI of 7.5 that suggests potentially different aggregation properties than either lysozyme or α-lactalbumin. These proteins have features that make them convenient choices for nanoparticle linkers (e.g., commercial availability, well-characterized, resistant to denaturation), but they also provide a model set for assessing the features that would contribute to forming a coronal layer. We have explored chemical modification, pH variation, and/or site-specific mutagenesis to alter these proteins and examine interactions with AuNP. The results presented demonstrate that positively charged residues on the protein surfaces drive interactions to cross-link AuNP into three-dimensional aggregates. Importantly, this aggregate formation can be tailored by chemically or genetically modifying the protein and altering solution pH. The chemical nature of the protein surface is shown to be a highly relevant factor in defining the architecture of bionanoconjugates. The data also indicate that chemical modifications in

vivo—phosphorylation, methylation, acetylation, glycosylation—have the potential to exert significant impact on nanoparticle–protein interaction. The methods presented can be generalized to other protein–nanoparticle interactions based primarily on protein surface charge (positive or negative) and can be used with any protein to selectively modulate protein–AuNP interaction.

Materials and methods

Materials

All chemicals and lyophilized powders of lysozyme (chicken egg white) and α-lactalbumin (bovine, type III, calcium depleted) were purchased from Sigma-Aldrich unless specified otherwise. Buffers utilized for the experiments were: pH 3.4, 20 mM sodium citrate/sodium chloride; pH 5, 10 mM sodium phosphate; pH 7.7, pH 8.1, pH 8.8, 18 mM sodium phosphate; pH 12, 10 mM KCl, 0.024 M NaOH or 10 mM sodium phosphate. Control measurements under each buffer condition were performed to ensure that free AuNPs did not aggregate across this broad pH range.

Gold nanoparticle synthesis

Gold nanoparticles were prepared according to methods described previously (Frens 1973; Calabretta, Jamison *et al.* 2005). Typically, 38.8 mM trisodium citrate dihydrate (Aldrich, 99%) was added to 50 ml of boiling 1 mM tetrachloroaurate trihydrate (ACS) (Aldrich). The color of the mixture changed from yellow to colorless, then to faint blue followed by deep red, indicating the formation of AuNPs. The suspension was allowed to heat for 10 min with stirring. AuNPs from this preparation are typically 13 nm in diameter, as measured by transmission electron microscopy (TEM).

Prepared AuNPs were stored at 4 ^{o}C for several months and used for experiments until visible aggregates formed. Nanoparticle concentrations were estimated by dividing the initial concentration of atomic gold (1 mM) by the number of gold particles formed:

$$[AuNP] = \frac{4}{3}\pi r^3 \frac{\rho_{gold}}{aw_{gtold}} A,$$

where r is the average radius of the particles from TEM data ρ_{gold} is the density of bulk gold (17 g/cm^3), A is Avogadro's number, and aw_{gold} is the atomic weight of gold (197.97 g/mol). This estimation assumes that all starting material is incorporated into spherical particles with the density of bulk gold (Frens 1973). Using a molar absorption coefficient of 2.5 x 10^8 M^{-1} cm^{-1} at 506 nm estimated from the analysis of Liu (Liu, Atwater *et al.* 2007), which itself has limitations, AuNP concentrations were within ~25% of the calculated value utilized in our experiments.

Ultraviolet and visible spectroscopy

For each experiment, proteins at the selected concentration were suspended in buffer at the appropriate pH. AuNPs were added to protein at molar ratios indicated in the individual experiments. The final concentration of gold particles was selected to provide absorbance within the linear range of the Varian Cary 50 spectrophotometer utilized in the experiments. Absorbance for each experiment was determined from 450 to 800 nm.

Circular dichroism spectroscopy

Circular dichroism spectra were measured at a protein concentration of 4–20 μM for lysozyme, α-lactalbumin, and myoblogin at each of the relevant experimental conditions and following chemical modification. Spectra were obtained on AVIV 62DS and JASCO J-815 spectrometers. The wavelength range was from 200 to 250 nm, and the step size and averaging time were 1 nm and 2 s, respectively. Each protein scan was repeated in triplicate.

Wild-type and K63C myoglobin

Myoglobin was expressed in *Escherichia coli* BL21 using pUC19 expression vectors. Cells were grown in 14 l batches in LB with 100 μg/ml of ampicillin for 16–18 h at 37 C and exposed to carbon monoxide for 20 min. Protein purification was carried out according to a variation of the protocol of Springer and Sligar (Springer and Sligar 1987). Following the collection of the pellets in a centrifuge, cells were resuspended in lysis mix and allowed to stir at 4 C overnight. The cell lysis mix was centrifuged, and 50% ammonium sulfate was added to the preserved supernatant, followed by another round of centrifugation in which the pellet was preserved, resuspended, mixed with 95% ammonium sulfate, and centrifuged. The resulting pellets were resuspended and dialyzed overnight in 20 mM Tris–HCl (pH 8.0), 1 mM EDTA, then concentrated and run through a diethyl aminoethyl cellulose anion exchange column, followed by a CM52 (carboxymethyl) cellulose cation exchange column. The protein was eluted from the CM52 column using a sodium phosphate gradient, ranging from 20 (pH 6.0) to 50 mM (pH 9.0), and concentrated. The final concentration of protein was determined with

ultraviolet–visible spectroscopy using an extinction coefficient of 187 nM-1 cm-1 at 423 nm.

Succinylation of lysozyme and myoglobin

Succinylation of lysozyme or wild-type myoglobin was achieved by adding at least a 20-fold molar excess of succinic anhydride (99%) to a solution of 400 μM lysozyme or to a solution of 4 μM for myoglobin, both in 10 mM sodium phosphate buffer (pH 8.3). The succinic anhydride was added gradually to the protein solutions over the course of an hour with constant stirring. The pH was maintained above 8with NaOH throughout the reaction to ensure complete succinylation. After the final addition, the reaction proceeded for 15 min before dialysis against 10 mM sodium phosphate (pH 8.3) for lysozyme and 10 mM sodium phosphate (pH 5) for myoglobin, to remove any non-reacted reagent.

Acetylation of lysozyme

Acetylation was performed based on a previously established protocol (1971). A stock solution of lysozyme was made at a concentration of 400 μM in 10 mM sodium phosphate (pH 8.3). A 20-molar excess of acetic anhydride (99.5%) was added to the protein solution with stirring on ice, and the reaction was allowed to proceed for 1 h. The pH was maintained above 7.0 for the entire reaction by the addition of NaOH. The modified protein was dialyzed into 10 mM sodium phosphate (pH 8.3).

Aminoalkylation of α-lactalbumin

Aminoalkylation was achieved in a manner similar to established methods (Hermanson 1996). A stock solution of 400 μM α-lactalbumin was made in 0.1 M sodium phosphate (pH 7.0). Ethylenediamine dihydrochloride (Thermo Scientific) was dissolved in the same buffer to a concentration of 1 M with stirring in an ice bath within a fume hood. An equal volume of the α-lactalbumin solution was added to the diamine solution with constant stirring. 1-Ethyl-3- (3-dimethylaminopropyl) carbodiimide hydrochloride (EDC) (Pierce, 98%) was added to a final concentration of 2 mg/ml. The reaction was then allowed to proceed for 2 h at room temperature, followed by dialysis in phosphate buffered saline (pH 7.4).

Characterization of modified proteins

SDS-polyacrylamide gel electrophoresis of modified proteins demonstrated that the chemical reactions to which the proteins were subjected did not alter molecular weight (i.e., no cross-linking occurred), and native gel electrophoresis demonstrated the anticipated shift in mobility based on altered pK. Circular dichroism spectra of the modified proteins were similar to the unmodified parent protein in the case of lysozyme and α-lactalbumin, with a small loss for the latter. These data indicate that no significant structural alterations were elicited by modification for these cases. Circular dichroism spectra for succinylated myoglobin displayed ~50% loss in secondar structure as compared to unmodified protein.

Conjugate formation

Lysozyme (~400 lM), α-lactalbumin (~400 lM), myoglobin (4 μM), or their modified versions were dissolved in buffer of the appropriate pH for the experiment, ranging from pH 3.4 to 12. A AuNP suspension was added to the proteins diluted to the concentrations specified in the experiments shown so that the final concentration of AuNPs (4 nM) was sufficiently dilute to decrease the plasmon absorbance to below 1 absorbance unit. Samples were allowed to conjugate at room temperature for the indicated times. UV–visible spectra of conjugates were recorded in a Varian Cary 50 spectrophotometer.

Transmission electron microscopy

Sample grids were prepared by drying 20 μl of bioconjugate suspensions on 400 mesh carbon/formvar coated copper mesh (Ted Pella). Images were obtained by using JEM-2010 and JEOL 1230 high contrast transmission electron microscopes operated at 200 and 120 kV, respectively. Size distribution data were obtained by counting a minimum of 750 nanoparticles using Image-Pro Plus 5.0 (Media Cybernetics, Inc., Silver Springs, MD).

Dynamic light scattering

Samples for dynamic light scattering (DLS) were prepared in 500 μl volumes. Prior to the measurement, 1 ml of corresponding buffer was added to each sample. Hydrodynamic diameter analyses (D_h) reported in Tables 1 and 2 were carried out with Brookhaven ZetaPALS DLS equipment with BI- 9000AT digital autocorrelator at 656 nm

wavelength. All studies were carried out in triplicate at a 90 scattering angle and temperature controlled at 25 C (McNeil-Watson, Tscharnuter *et al.* 1998). As colloidal particles undergo Brownian diffusion, the scattered light from these particles exhibits corresponding phase fluctuations, detected as time-dependent intensity variation. The rate of fluctuation is related to the diffusivity of the particles which can be converted to the hydrodynamic diameter through the Stokes–Einstein relation. A Laplace inverse program, NNLS, was utilized to determine the intensity-weighted aggregate particle size, D_h. Averages presented were derived from the D_h values calculated from three separate measurements. For confirmation, similar experiments were performed on a Malvern Zetasizer Nano Series; the measurements yielded similar dimensions for AuNP and smaller dimensions for aggregates formed, but the pattern of behavior for the conditions examined was identical.

Results and discussion

Influence of surface charge on AuNP–protein aggregate formation

Surface charge at a specific pH can vary significantly for different proteins as a function of pI. We explored the impact of pH for lysozyme (pI ~11.5), which has been used in the formation of aggregates with NP (Verma, Srivastava *et al.* 2005; Yang, Li *et al.* 2007; Zhang, Neumann *et al.* 2009), for α-lactalbumin, and for myoglobin to establish a baseline. UV–visible spectroscopy, TEM, and DLS were used to characterize aggregate formation.

Citrate-stabilized AuNPs that are unaggregated and unconjugated have a

characteristic absorbance maximum at approximately 520 nm due to surface plasmon resonance. Spectroscopic behavior for free AuNP was similar over the experimental range of pH, despite the requisite use of different buffer systems (detailed in ‘‘Materials and methods section). At pH greater than the pI for lysozyme (pH 12), the uncharged protein did not promote significant AuNP aggregation, as evidenced by only a slight change in the plasmon peak position, the dispersion of single AuNP in TEM,[2] and diameter (D_h) ranges similar to free AuNP by DLS (Fig. 1a, b, Table 1). (Note that at this pH, the circular dichroism spectrum indicates minimal loss in secondary structure.) In contrast, below the pI at pH 8, the positively charged surface of lysozyme promoted aggregation, as observed previously (Verma, Srivastava *et al.* 2005); this aggregation was reflected in a red shift and broadening in the plasmon peak position. Moreover, TEM analysis revealed aggregation of lysozyme: AuNP consistent with DLS data that showed a substantial increase inthe particle hydrodynamic diameter (Fig. 1a, b, Tables 1, 2).

In order to explore whether the impact of surface charge can be generalized to a protein with a highly similar tertiary structure, we examined α-lactalbumin, which has a much lower pI at ~4.5. We demonstrate similar behavior with AuNP to that observed for lysozyme above and below their respective pI values: A small shift in the plasmon peak position for AuNP in the presence of α-lactalbumin was observed at pH 5, indicating protein binding, but no aggregation. TEM and DLS results also indicate minimal aggregation (Fig. 1c, d, Table 1). Below the pI at pH 3.4, however, aggregation was indicated by a significant shift in the plasmon resonance peak, aggregate formation visualized by TEM, and increased average hydrodynamic diameter from 33 ± 3nm to

[2]Crystals were consistently present in all frames observed for the TEM experiments conducted at pH 12, presumably derived from buffer drying effects under these conditions (see Fig. 1 legend).

>1,000 nm by DLS (Fig. 1c, d, Table 1).

Myoglobin is a small globular protein of similar size but entirely distinct tertiary structure and displays a pI intermediate to lysozyme and α-lactalbumin. At pH values near recombinant sperm whale myoglobin's pI, only a small change was observed in the AuNP optical absorption spectrum (Fig. 1e). Under the same conditions, AuNP appeared well isolated by TEM a swell as DLS (33 ± 5 nm), reflecting minimal aggregation (Fig. 1f, Table 1). In contrast, below the pI at pH 5, where the protein has an overall positive charge, we observed a significant shift in plasmon resonance, indicating aggregation. This conclusion is supported by observations from TEM and DLS (Fig. 1f, Table 1). All three proteins, with significantly different pI values, follow a similar pattern of inducing AuNP aggregation only below their pI. Interestingly, the aggregates did not grow to very large sizes, but rather appeared self-limiting in their growth.

Table 1 Dynamic light scattering data for AuNP and AuNP– protein complexes

Sample composition and pH	Average hydrodynamic diameter (D_h) (nm)
AuNP (water)	35 ± 3
AuNP, pH 8	41 ± 3
Lysozyme–AuNP, pH 12	39 ± 3
Lysozyme–AuNP, pH 8	>1,000
Acetylated Lysozyme–AuNP, pH 8	36 ± 3
Succinylated Lysozyme–AuNP, pH 8	39 ± 1
α-Lactalbumin–AuNP, pH 5	33 ± 3
α-Lactalbumin–AuNP, pH 3.4	>1,000
Aminated α-Lactalbumin–AuNP, pH 5	>1,000
Myoglobin–AuNP, pH 7.7	33 ± 5
Myoglobin–AuNP, pH 5	>1,000
Succinylated Myoglobin–AuNP, pH 5	170 ± 10

DLS data were obtained as described in ''Materials and methods'' section. Samples were prepared at a protein:particle ratio in each case of 100:1, and buffers utilized are identified in ''Materials and methods section. The average hydrodynamic diameter (D_h) is derived from at least three separate measurements under the indicated conditions

Manipulating surface charge by chemical modification of amino acids

Amino acid functional groups can be modified using a variety of chemicals that alter side chain chemistry and result in different surface charges. The alterations can substantially change protein pI and therefore surface charge at a given pH. Succinylation converts the positively charged lysine amino groups into moieties that display carboxyl groups with low pK values, are negatively charged when ionized, and are neutral when not ionized. In contrast, acetylation blocks the amino group of lysine by forming an amide, resulting in a non-ionizable side chain and thus lowering the pI of the protein. These modifications can result in a substantial shift of the protein pK toward lower pH. In contrast, reaction with ethylenediamine alters the side chains of glutamate and aspartate, converting carboxylate groups via amid formation to a side chain that terminates with an amino group. This reaction converts these acidic residues into basic side chains that are positively charged when ionized and exhibit a high pK, thereby shifting the pI for the protein to a higher pH.

Table 2 Concentration-dependent dynamic light scattering data for AuNP and AuNP–protein complexes

Protein	Average hydrodynamic diameter (D_h) (nm)			
	Protein:AuNP, 5:1	**Protein:AuNP, 20:1**	**Protein:AuNP, 40:1**	**Protein:AuNP, 100:1**
Lysozyme, pH 8	200 ± 20	>1,000	>1,000	>1,000
α-Lactalbumin, pH 3	120 ± 8	~1,000	>1,000	>1,000
Myoglobin, pH 5	580 ± 110	>1,000	>1,000	>1,000

DLS data were obtained as described in ‘‘Materials and methods ’’ Samples were prepared at the indicated protein:particle ratio, and buffers utilized are identified in ‘‘Materials and methods’’ section. The average hydrodynamic diameter (D_h) is derived from at least three separate measurements under the indicated conditions.

Impact of chemical modification on lyzozyme–AuNP interaction

In order to establish whether chemical modification could be used to regulate AuNP aggregation, we utilized succinylation and acetylation to lower the pK of lysine residues in lysozyme and thereby lower the pI of this protein. Characterization with circular dichroism spectra and SDS-polyacrylamide gel electrophoresis demonstrated that these modifications did not significantly diminish protein folding or generate oligomer formation, and native polyacrylamide gel electrophoresis demonstrated the expected alteration in charge. We examined the effects of these chemical modifications on the visible spectra of protein–AuNP conjugates and on their diameters as measured with DLS. At pH 8 where lysozyme normally aggregates, Fig. 2a shows that succinylated lysozyme and acetylated lysozyme in the presence of AuNP at pH 8 generated minimal spectral alteration, indicating the absence of significant aggregation. This interpretation is further supported by DLS analysis, which yielded average hydrodynamic diameters of 39

± 1 and 36 ± 3 nm for succinylated lysozyme and acetylated lysozyme, respectively (Table 1).

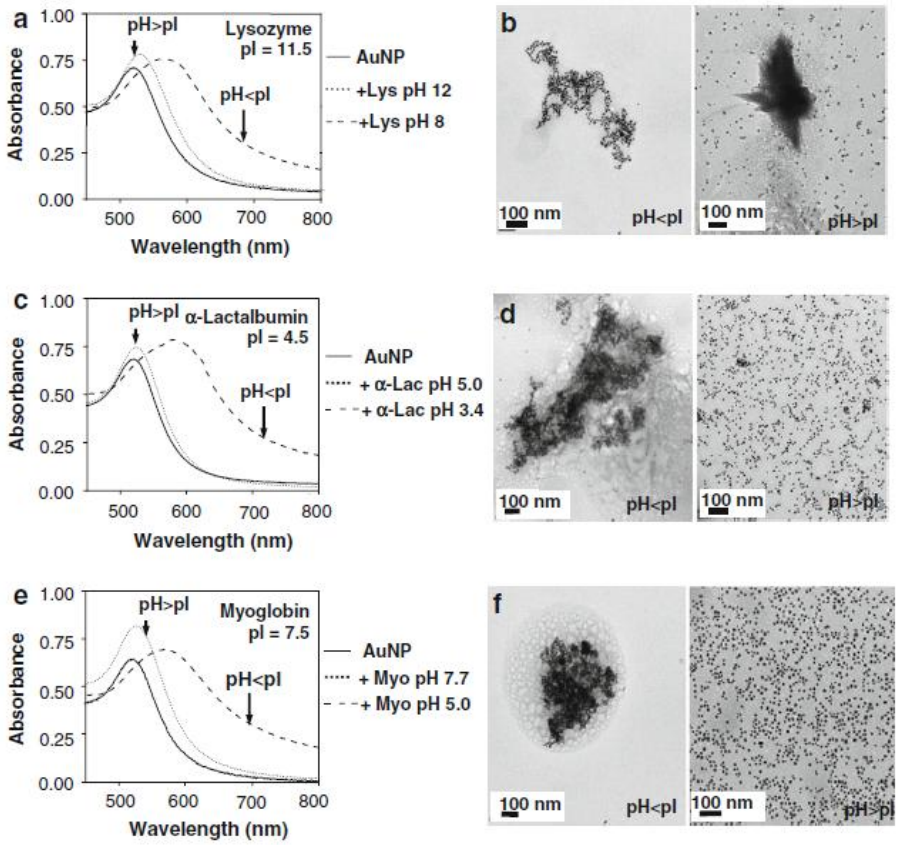

Fig. 1 Effect of solution pH on stability and aggregation of protein–AuNP conjugates. AuNP concentration was ~4 nM, and protein was present at 100-fold molar excess for these measurements. **a, b** Lysozyme; **c, d** α-lactalbumin; **e, f** myoglobin. **a,c,e** Visible spectra of unconjugated AuNP (solid line) and bionanoconjugates above (dotted line) and below (dashed line) the pI. **b, d, f** TEM images of bionanoconjugates below (left) and above (right) each protein's pI. Crystals were prevalent for the sample at pH 12 (panel b, right), presumably due to buffer drying effects; such effects can complicate image analysis in TEM, as noted for other systems e.g., (Ohara, Leff *et al.* 1995; Vossmeyer, Chung *et al.* 1998; Lu, Chen *et al.* 2008). Nonetheless, the TEM data provide a qualitative confirmation of the aggregation indicated by absorption spectroscopy and DLS data (Table 1). Aggregation is evident in bionanoconjugates below the pI, whereas data above the pI indicate dispersed bionanoconjugates. Buffers utilized are detailed in ''Materials and methods'' section, and AuNP spectra were acquired at the different pH values indicated for each of the proteins.

Impact of chemical modification on AuNP–α-lactalbumin interaction

In order to confirm the role of chemically altering pI in bioconjugate aggregation, we extended our examination of the effects of chemical modification to α- lactalbumin. Unmodified α-lactalbumin has an acidic pI at 4.5, and therefore interaction with AuNP does not result in a shifted plasmon peak at pH 5.0 (Fig. 2b). We generated aminated α-lactalbumin to increase the pI of the protein by converting carboxylate side chains to moieties that terminate with amino groups. This modification did not impact molecular weight by SDS gel electrophoresis and introduced a small decrease in the circular dichroism spectrum; altered mobility of modified protein in native polyacrylamide gel electrophoresis was consistent with modification. At pH 5.0, we observed aggregation of nanoparticles exposed to aminated α-lactalbumin based on the large shift in the plasmon peak (Fig. 2b) and DLS data, which yielded an average hydrodynamic diameter of >1,000 nm (Table 1).

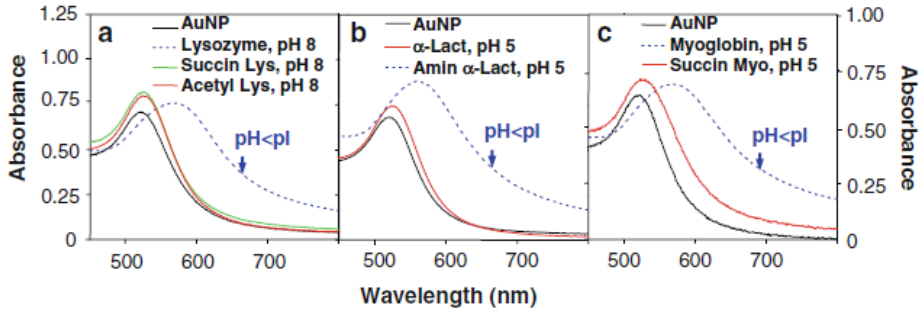

Fig. 2 The effects of chemical modification on the aggregation of protein–AuNP conjugates. Visible spectra at protein:AuNP ratios of 100:1. **a** Modified lysozyme–AuNP conjugates (succinylated—green and acetylated—red) are shown at pH 8 relative to unmodified lysozyme–AuNP conjugates (blue) and unconjugated AuNP (black). **b**Modifiedα-lactalbumin–AuNP conjugates at pH 5 (aminated—blue) relative to unmodified α-lactalbumin–AuNP conjugates (red) and unconjugated AuNP (black). **c** Modified myoglobin–AuNP conjugates at pH 5 (succinylated—red) relative to

unmodified myoglobin–AuNP conjugates (blue) and unconjugated AuNP (black). Buffers utilized are detailed in ‘‘Materials and methods’’ section.

Impact of chemical modification on AuNP–myoglobin interaction

Myoglobin is slightly larger than either lysozyme or α- lactalbumin, and its pI at pH ~8 is intermediate between the two other proteins. In order to explore the impact of surface charge alteration for wild-type myoglobin, we applied the succinylation reaction to convert lysine residues to side chains that terminate in carboxyl groups, thereby generating a lower pI. Gel electrophoresis demonstrated no change in molecular weight (SDS-gel) and the expected shift in the protein charge (native gel). In this case, modification resulted in circular dichroism spectra that indicated diminished tertiary and secondar structure. Nonetheless, although wild-type myoglobin formed aggregates at pH 5 (Fig.2c), succinylated myoglobin at the same pH exhibited only minor spectral changes, indicating a lower level of aggregation, an interpretation that wasconsistent with DLS data (Table 1).

These data collectively demonstrate that modifications to the protein surface that shift the pI of the protein change aggregation properties relative to the unmodified protein at the same pH. Of specific importance, the pH range for achieving stable, isolated bioconjugates can be expanded by these chemical modifications.

Concentration dependence and kinetics of aggregate formation

Aggregate formation can occur either through coverage of an AuNP surface by a protein and subsequent aggregation of the bio-nanocomplexes or through cross-linking of AuNP–protein complexes that initiates at low surface coverage. These distinct processes

result in very different aggregate morphology. Particularly in the first case, additional control over the extent and time-scale of aggregation may be derived by using proteins of different concentrations, sizes, shapes, or surface charge distribution. With AuNPs of 13 nm diameter, we estimate the surface area to be in the range of 530 nm^2 , and the maximum occupancy of the surface to be ~25–30 molecules of these small proteins (~3.5 nm diameter plus hydration sphere). We measured concentration dependence of the aggregation dynamics using the shift in λ_{max} as an indicator of aggregate formation. At pH below the pI, this shift initiates at protein:AuNP ratios ~5:1 (Fig. 3a, Table 2) and does not occur at all at pH greater than the pI. For succinylated and acetylated proteins, aggregation is not observed at pH where this process occurs for the unmodified protein, as anticipated with the reaction of lysine side chains and consequent pK decrease. For aminated α-lactalbumin, which would exhibit an increased pK from introducing amino groups for carboxyls, aggregation occurs at pH 5 (where the unmodified protein does not aggregate) but not at pH 7, consistent with the shift to higher pK. The level at which maximum aggregation occurs (near the ratio required for surface coverage) and the lower extent of aggregation at lower protein ratios (based on shift of λ_{max} and DLS data) suggest an assembly process that proceeds first by association of the protein with the nanoparticle surface, then aggregation of these protein-associated nanoparticles.

The time-dependence for aggregation above and below the pI for each of the three proteins is shown in Fig. 3b. Aggregation occurs only below the protein's pI and requires protein:AuNP ratios of $\geq$20:1 for maximum aggregation. Further incubation of AuNP: protein mixtures did not result in aggregation for the proteins above their respective pI. With the AuNP:protein ratio at 20:1, aggregation is quite rapid, with >75% of this process

occurring within the shortest time measurement of <1 min for all proteins examined. At lower AuNP:protein ratios, a modest increase in average particle diameter is observed for α-lactalbumin and lysozyme, whereas a larger increase is found for myoglobin (Table2). These results are consistent with the requirement for some level of protein–nanoparticle association prior to aggregate formation.

Using site-specific mutagenesis to alter surface orientation

Myoglobin, with no cysteine residues, presents an opportunity to compare charge-induced aggregation and conjugation that involves both the sulfhydryl of an exposed cysteine side chain and surface positive charges. Using site-specific mutagenesis to generate Mb63C at a surface-exposed site, we examined the aggregation of this protein with AuNP. The characteristic small shift in the plasmon peak at 100:1 protein:AuNP was observed above the pI, whereas below the pI both wild-type and Mb63C myoglobin exhibited the familiar large shift in the wavelength of the plasmon peak (Fig. 4) along with similar increases in hydrodynamic ratio. However, the maximum spectral shift for Mb63C occurred at a protein:particle ratio two fold higher (20:1) than myoglobin (more similar to the ratio observed for lysozyme and α-lactalbumin). This difference presumably derives from the requisite binding orientation conferred to Mb63C through its thiol linkage to the AuNP, which may impede optimal electrostatic interaction and hence requires higher ratios to achieve the spectral shift. Thus, introduction of a novel thiol side chain introduces an additional point of potential control in protein–nanoparticle interaction.

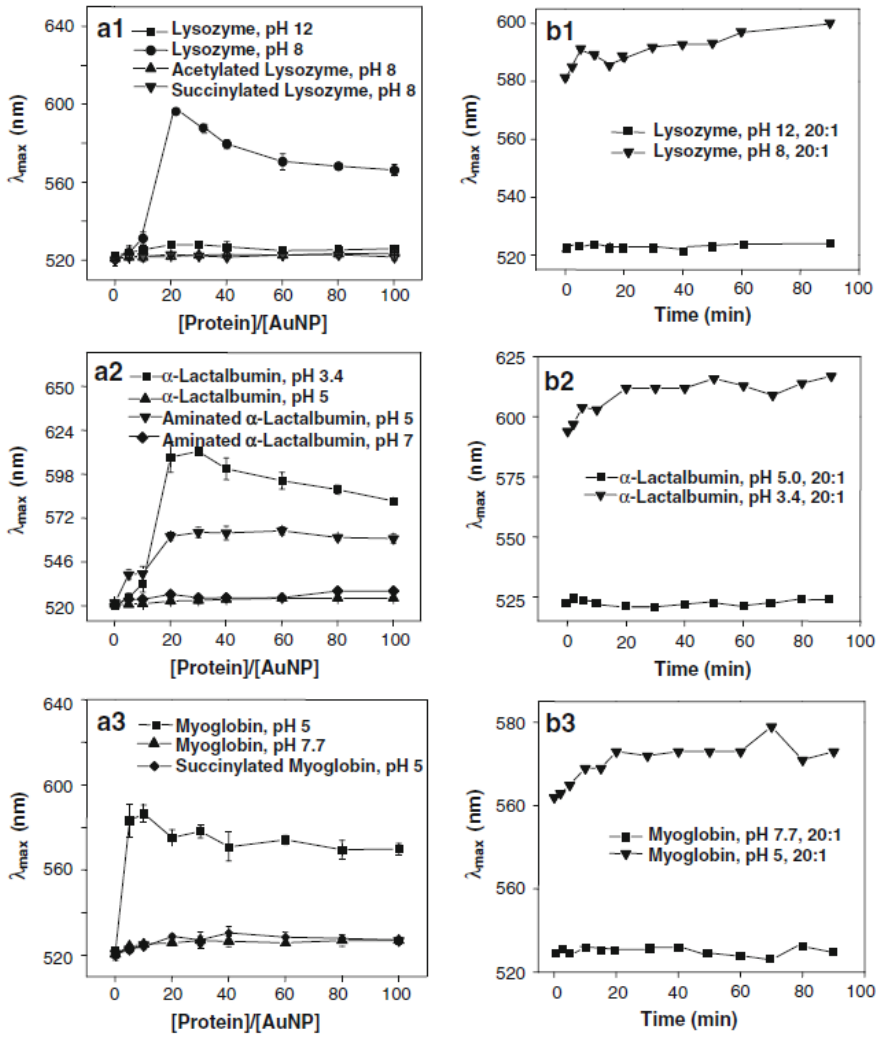

Fig. 3 The effect of protein concentration, pH, and time onλ_{max}.**a1–a3**Significant shift in AuNPλ_{max} initiates at protein:AuNP ratios of ~5–10-fold at pH values below the pK for the specific protein species and reaches maximum at a ratio of ~20. No spectral shift is observed above the pK or with chemical modifications that lower the pK. **b1–b3** Proteins at pH > pK do not exhibit spectral alterations within 90 min, and experiments of >6 h duration show no further spectral changes for proteins above the pK. At pH < pK, the spectral changes are rapid and reach a maximum within ~20 min. Buffers utilized are detailed in ‘‘Materials and methods’’ section

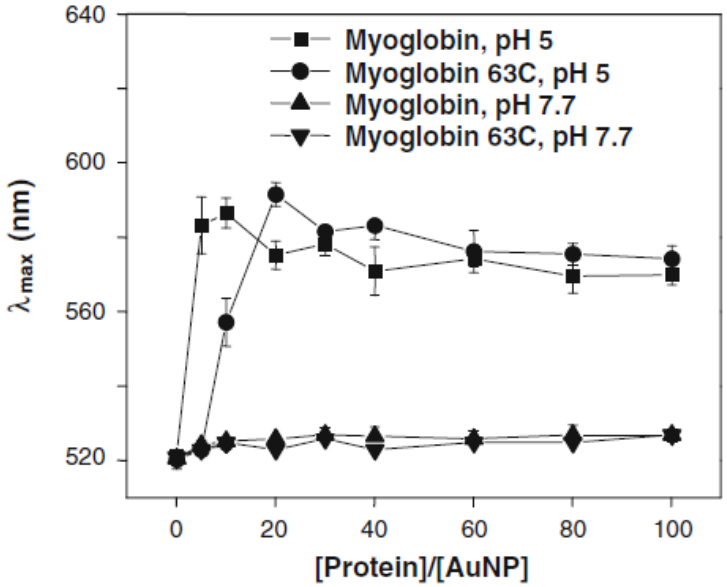

Fig. 4 The effect of protein concentration at multiple pH values on λ_{max} position for wild-type and mutant myoglobin. Myoglobin at pH 5 and myoglobin 63C at pH 5 exhibit typical shifts in their λ_{max} values, but note that the concentration required to achieve the maximal shift in the spectrum occurs at different protein concentrations. Myoglobin and myoglobin 63C at pH 7.7 both show nominal changes in λ_{max} with increasing protein concentration. Buffers utilized are detailed in ‘‘Materials and methods’’ section.

Conclusions

The experiments presented confirm that protein surface charge is the key feature for determining the interactions between proteins and citrate-stabilized AuNP in the absence of cysteine sulfhydryls. Consequently, the underlying assembly process is therefore a strong function of solution pH, and this property can be predicted based on protein pI (Fig.5). We demonstrate that significant differences in aggregation properties of a specific protein can be achieved using chemical modification to alter protein pI (and therefore charge at a given pH). The ability to vary surface charge selectively establishes a level of control in either limiting or promoting aggregate formation and expands the pH range that can be utilized. This feature maybe instrumental in designing materials

tailored to a variety of solution conditions. The distinct concentration-dependent aggregation observed for myoglobin versus its cysteine-containing variant at lower protein:AuNP ratios suggests that finer control of aggregation may be achieved with specific proteins by varying both pI and the presence and position of unique exposed cysteine side chains. Similarly, mutagenesis to alter charged surface side chains coupled with chemical modification and pH adjustments may allow design of proteins that promote selective assembly with nanoparticles. Interestingly, protein modification reactions in vivo may significantly alter the charge-based interaction of a protein with nanoparticles, and mechanisms that impact these modification reactions may provide a means to regulate the incorporation of a protein into the corona of a nanoparticle. Whereas significant attention has been devoted to strategies that modify nanoparticles to minimize or enhance association with proteins, this study demonstrates the utility of various mechanisms that alter the surface properties of the protein component of a bionanoconjugate to promote or mitigate aggregation.

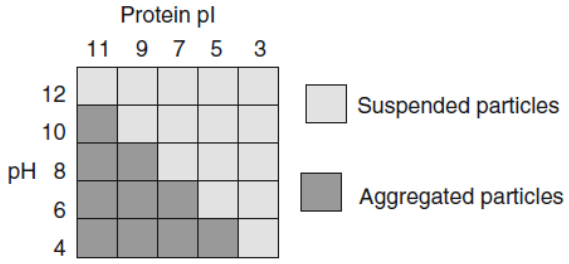

Fig. 5 Effect of pH on aggregation. The pH conditions under which formation of higher-order aggregates with citrate stabilized AuNP will occur can be predicted based on the pI of a specific protein, as indicated in the cartoon by dark gray shading. At pH above the pI, no aggregation will occur (light gray shading). Shifting the pI of the protein via chemical modification or genetic manipulation can alter the pH under which assembly will be observed. The process will also be influenced by introduction of cysteine(s) on

the protein surface that can orient the protein and impact the effective pI exposed to the AuNP

References

(1971). Acylating and similar reagents: acetic anhydride. Chemical modification of proteins. G. Means and R. Feeney. San Francisco, Holden-Day: 69-71.

Aggarwal, P., J. B. Hall, *et al.* (2009). "Nanoparticle interaction with plasma proteins as it relates to particle biodistribution, biocompatibility and therapeutic efficacy." Advanced Drug Delivery Reviews 61(6): 428-437.

Asuri, P., S. S. Bale, *et al.* (2006). "The protein-nanomaterial interface." Current Opinion in Biotechnology 17(6): 562-568.

Baudhuin, P., P. Van der Smissen, *et al.*, Eds. (1989).Molecular interactions between colloidal gold, proteins and living cells. Colloidal gold: principles, methods and applications. San Diego, Academic Press.

Brewer, S. H., W. R. Glomm, *et al.* (2005). "Probing BSA binding to citrate-coated gold nanoparticles and surfaces." Langmuir 21(20): 9303-9307.

Calabretta, M., J. A. Jamison, *et al.* (2005)."Analytical ultracentrifugation for characterizing nanocrystals and their bioconjugates." Nano Letters 5(5): 963-967.

Cedervall, T., I. Lynch, *et al.* (2007)."Understanding the nanoparticle-protein corona using methods to quantify exchange rates and affinities of proteins for nanoparticles." Proceedings of the National Academy of Sciences of the United States of America 104(7): 2050-2055.

Deroe, C., P. J. Courtoy, *et al.* (1987). "A Model of Protein Colloidal Gold Interactions." Journal of Histochemistry &Cytochemistry 35(11): 1191-1198.

Frens, G. (1973). "Controlled Nucleation for Regulation of Particle-Size in Monodisperse Gold Suspensions." Nature-Physical Science 241(105): 20-22.

Hermanson, G., Ed. (1996). Introduction of primary amine groups: modification of carboxylates with diamines. Bioconjugate techniques. San Diego, Academic Press.

Hu, M., L. Qian, *et al.* (2007). "Assembly of nanoparticle-protein binding complexes: From monomers to ordered arrays." Angewandte Chemie-International Edition 46(27): 5111-5114.

Iosin, M., F. Toderas, *et al.* (2009). "Study of protein-gold nanoparticle conjugates by fluorescence and surface-enhanced Raman scattering." Journal of Molecular Structure 924-26: 196-200.

Jiang, X., U. G. Jiang, *et al.* (2005). "Effect of colloidal gold size on the conformational changes of adsorbed cytochrome c: Probing by circular dichroism, UV-visible, and infrared spectroscopy." Biomacromolecules 6(1): 46-53.

Keating, C. D., K. M. Kovaleski, *et al.* (1998). "Protein : colloid conjugates for surface enhanced Raman scattering: Stability and control of protein orientation." Journal of Physical Chemistry B 102(47): 9404-9413.

Laaksonen, P., J. Kivioja, *et al.* (2009). "Selective Nanopatterning Using Citrate-Stabilized Au Nanoparticles and Cystein-Modified Amphiphilic Protein." Langmuir 25(9): 5185-5192.

Lacerda, S. H. D. P., J. J. Park, *et al.* "Interaction of Gold Nanoparticles with Common Human Blood Proteins." Acs Nano 4(1): 365-379.

Lim, S. I. and C.-J.Zhong (2009). "Molecularly Mediated Processing and Assembly of Nanoparticles: Exploring the Interparticle Interactions and Structures." Accounts of Chemical Research 42(6): 798-808.

Liu, X., M. Atwater, *et al.* (2007)."Extinction coefficient of gold nanoparticles with different sizes and different capping ligands." Colloids and Surfaces B-Biointerfaces 58(1): 3-7.

Lu, C., Z. Chen, *et al.* (2008). "Optimized conditions for the self-organization of CdSe-Au and CdSe-CdSe binary nanoparticle superlattices." Chemistry of Materials 20(11): 3594-3600.

Lundqvist, M., J. Stigler, *et al.* (2008). "Nanoparticle size and surface properties determine the protein corona with possible implications for biological impacts." Proceedings of the National Academy of Sciences of the United States of America 105(38): 14265-14270.

Lynch, I., T. Cedervall, *et al.* (2007). "The nanoparticle - protein complex as a biological entity; a complex fluids and surface science challenge for the 21st century." Advances in Colloid and Interface Science 134-35: 167-174.

Lynch, I. and K. A. Dawson (2008). "Protein-nanoparticle interactions." Nano Today 3(1-2): 40-47.

Lynch, I., A. Salvati, *et al.* (2009). "PROTEIN-NANOPARTICLE INTERACTIONS What does the cell see?" Nature Nanotechnology 4(9): 546-547.

McNeil-Watson, F., W. Tscharnuter, *et al.* (1998). "A new instrument for the measurement of very small electrophoretic mobilities using phase analysis light scattering (PALS)." Colloids and Surfaces a-Physicochemical and Engineering Aspects 140(1-3): 53-57.

Nakata, S., N. Kido, *et al.* (1996). "Chemisorption of proteins and their thiol derivatives onto gold surfaces: Characterization based on electrochemical nonlinearity." Biophysical Chemistry 62(1-3): 63-72.

Nel, A. E., L. Maedler, *et al.* (2009). "Understanding biophysicochemical interactions at the nano-bio interface." Nature Materials 8(7): 543-557.

Ofir, Y., B. Samanta, *et al.* (2008). "Polymer and biopolymer mediated self-assembly of gold nanoparticles." Chemical Society Reviews 37(9): 1814-1823.

Ohara, P. C., D. V. Leff, *et al.* (1995). "Crystallization of Opals from Polydisperse Nanoparticles." Physical Review Letters 75(19): 3466-3469.

Roecker, C., M. Poetzl, *et al.* (2009). "A quantitative fluorescence study of protein monolayer formation on colloidal nanoparticles." Nature Nanotechnology 4(9): 577-580.

Springer, B. A. and S. G. Sligar (1987)."High-Level Expression of Sperm Whale Myoglobin in Escherichia-Coli." Proceedings of the National Academy of Sciences of the United States of America 84(24): 8961-8965.

Srivastava, S., A. Verma, *et al.* (2005)."Controlled assembly of protein-nanoparticle composites through protein surface recognition." Advanced Materials 17(5): 617-621.

Verma, A., S. Srivastava, *et al.* (2005)."Modulation of the interparticle spacing and optical behavior of nanoparticle ensembles using a single protein spacer." Chemistry of Materials 17(25): 6317-6322.

Vossmeyer, T., S. W. Chung, *et al.* (1998). "Surprising superstructures: Rings." Advanced Materials 10(4): 351-353.

Wang, Z. and L. Ma (2009). "Gold nanoparticle probes." Coordination Chemistry Reviews 253(11-12): 1607-1618.

Yang, T., Z. Li, *et al.* (2007)."Synthesis, characterization, and self-assembly of protein lysozyme monolayer-stabilized gold nanoparticles." Langmuir 23(21): 10533-10538.

You, C.-C., A. Chompoosor, *et al.* (2007)."The biomacromolecule-nanoparticle interface." Nano Today 2(3): 34-43.

Zhang, D., O. Neumann, *et al.* (2009). "Gold Nanoparticles Can Induce the Formation of Protein-based Aggregates at Physiological pH." Nano Letters 9(2): 666-671.

APPENDIX 3: ONE-STEP REVERSE PRECIPITATION SYNTHESIS OF WATER-DISPERSIBLE SUPERPARAMAGNETIC MAGNETITE NANOPARTICLES

One-step reverse precipitation synthesis of water-dispersible superparamagnetic magnetite nanoparticles

Jieying Jing • Yu Zhang • Jiangyu Liang • Qingbo Zhang •Erika Bryant • Carolina Avendano • Vicki L. Colvin •Yiding Wang • Wenying Li • William W. Yu

Journal of Nanoparticle Research 14, 4, 827

J. Jing *W. Li*W. W. Yu
Key Laboratory of Coal Science and Technology of Shanxi Province and Ministry of Education, Taiyuan University of Technology, Shanxi 030024, China
e-mail: ying@tyut.edu.cn

W. W. Yu
e-mail: wyu6000@gmail.com

J. Jing * Q. Zhang * E. Bryant * C. Avendano * V. L. Colvin * W. W. Yu
Center for Biological and Environmental Nanotechnology, Department of Chemistry, Rice University, Houston, TX 77030, USA

Y. Zhang * Y. Wang * W. W. Yu
State Key Laboratory on Integrated Optoelectronics, College of Electronic Science and Engineering, Jilin University, Changchun 130012, China

J. Liang
Department of Mechanical Engineering, Worcester Polytechnic Institute, Worcester, MA 01609, USA

W. W. Yu
College of Material Science and Engineering, Qingdao University of Science and Technology, Qingdao 266042, China

Abstract

Hydrophilic functionalization of nanoparticle surface is essential for their biomedical applications. Herein, we report a facile one-step reverse precipitation method to synthesize water-dispersible, biocompatible, and carboxylate-functionalized superparamagnetic magnetite (Fe_3O_4) nanoparticles with the help of biocompatible sodium citrate salt. Transmission electron microscope (TEM), X-ray diffraction (XRD), Fourier transform infrared spectroscopy (FTIR), zeta potential measurement, dynamic light scattering (DLS), and superconducting quantum interference device (SQUID) were used to characterize the as-prepared magnetite nanoparticles. The size of the as-prepared magnetite nanoparticles was tuned from 27 ± 3.8 to 4.8 ± 1.9 nm by changing the sodium citrate concentration from 25 to 125 mM. The sodium citrate concentration also influenced the water-dispersible stability of the as-prepared magnetite nanoparticles, which was due to the electrostatic repulsion.

Keywords Magnetite * Water-dispersible * Nanoparticle * One-step reverse precipitation * Sodium citrate

Introduction

Magnetite (Fe_3O_4) nanoparticles are highly potential for biomedical applications, such as magnetic resonance imaging, drug delivery, and bioseparation because of their unique physical and chemical properties (Shukla, Patra *et al.*; Xiao, Li *et al.*; Gupta and Gupta 2005; Qiao, Yang *et al.* 2009; Tanaka, Shimazu *et al.* 2009; Teja and Koh 2009; Tung and Daoud 2009). High performance of magnetite nanoparticles in biomedical application requires them to possess a combination of properties including: (1) dispersibility in aqueous media and biocompatibility, (2) surface chemistry suitable for further functionalization, (3) suitable size with uniform dispersion that greatly influence their magnetic behaviors, and (4) high magnetization for effective signal enhancement. Hence, many strategies have been explored to synthesize highly water dispersible superparamagnetic magnetite nanoparticles with controllable sizes and desirable surface properties.

One common method to synthesize hydrophilic magnetite nanoparticles is to co-precipitate ferrous (Fe^{2+}) and ferric (Fe^{3+}) ions in a basic aqueous solution. This method is generally simple and it is easy to gain high yields and large quantities, but most of the reported aqueous syntheses suffer from poor crystallinity and polydispersity because the co-precipitation process is kinetically driven (formation of an insoluble precipitate being the driving force) and does not provide good control over crystallinity and size distribution of the as-prepared nanoparticles (Fang, Ma *et al.* 2007; Deng, Qi *et al.* 2008; Laurent, Forge *et al.* 2008; Yao, Peng *et al.* 2009; Wei, Wei *et al.* 2011). On the contrary, magnetite nanoparticles produced from organic thermal decomposition are monodisperse and have high crystallinity (Jana, Chen *et al.* 2004; Park, An *et al.* 2004;

Yu, Falkner *et al.* 2004); therefore, many ligand exchange approaches were developed to offer them hydrophilic surface for aqueous dispersibility (Qu, Caruntu *et al.*; Yu, Chang *et al.* 2006; Baldi, Bonacchi *et al.* 2007; Prakash, Zhu *et al.* 2009). However, these organic-based syntheses usually require complicated operations and sometimes expensive/toxic reagents that are not environment friendly. In recent years, some researchers have employed polyols to synthesize magnetic nanoparticles (Miguel-Sancho, Bomati-Miguel *et al.*; Ge, Hu *et al.* 2007; Ge, Hu *et al.* 2007; Cheng, Wen *et al.* 2009). Liquid polyols, such as ethylene glycol, was used as a reductive agent to partially reduce the precursor from its high valence (Fe^{3+}) to a lower valence (Fe^{2+}), and then the hydrophilic magnetic nanoparticles were synthesized in situ and might further simultaneously self-assemble to clusters with compact structures. However, because this polyol process is very sensitive to the concentration of water and alkalinity, it is still a challenge to control the diameter, surface property of the as-prepared magnetite nanoparticles through varying reaction parameters. Consequently, the preparation of water-dispersible magnetite nanoparticles with appropriate surface coating remains a hot topic for preparative nanotechnology.

In this study, a reliable and facile one-step reverse precipitation method is reported to synthesize water dispersible carboxylate-functionalized superparamagnetic magnetite nanoparticles with the help of biocompatible sodium citrate salt. In this method, a solution of metal salt is added to an alkaline solution to keep homogeneity of the reaction system during the formation process of the metal hydroxides. It uses commercial available, inexpensive, and environmentally acceptable raw reaction materials (water is the solvent), and represents an economic and green approach for the

controlled synthesis of magnetite nanoparticles. More importantly, the as-prepared magnetite nanoparticles exhibit high water-dispersible stability and superparamagnetic property with relatively high saturation magnetization at room temperature, which are key requirements for biomedical application.

Experimental section

Materials

Ferrous sulfate heptahydrate ($FeSO_4*7H_2O$), potassium nitrate (KNO_3), potassium hydroxide (KOH), sodium citrate, and sodium chloride (NaCl) were purchased from Sigma-Aldrich. Ultrapure water with resistivity of 18.2 MΩ cm from Milli-Q Plus, Millipore, was used for the preparation of all aqueous solutions. All chemicals are used as received.

Synthesis of water-dispersible magnetite nanoparticles

Water-dispersible magnetite nanoparticles were synthesized using one-step reverse precipitation method in the presence of sodium citrate (Sugimoto and Matijevic 1980; Cheng, Wen *et al.* 2009; Mizukoshi, Shuto *et al.* 2009). The magnetite nanoparticle formation is based on aging $Fe(OH)_2$ gels at 90 ^oC for 5 h in the presence of KNO_3 as an oxidizing agent. Typically, 0.83 ml 0.50-MKNO_3 was firstly added to 100 ml 0.10-M KOH solution, the obtained transparent solution was degassed with nitrogen for 30 min; then 200 ml of 25-mM $FeSO_4*7H_2O$ and a pre-determinate amount of sodium citrate solution were added to this solution under stirring of 600 rpm. After being stirred for 1 h, the resultant black solution was heated to 90 ^oC and maintained at this temperature for 5

h. The reaction was protected under nitrogen to avoid the uncontrollable oxidizing effect of air. After being cooled down to room temperature, the as-prepared magnetite nanoparticles were precipitated by acetone to remove the excessive sodium citrate, and then the as-prepared magnetite nanoparticles were collected with a permanent magnet and vacuum dried at 30 ^{o}C. The resulted powders were finally re-dispersed in ultrapure water. The water-dispersible magnetite nanoparticles obtained at sodium citrate concentrations of 0, 25, 50, 75, 100, and 125 mM were denoted asNP-0, NP-25, NP-50, NP-75, NP-100, and NP-125, respectively.

Characterization

Transmission electron microscopy (TEM) images and selected area electron diffraction (SAED) patterns were taken by a JEOL 2100 field emission TEM operating at 200 kV. A Rigaku Geigerflex X-ray diffractometer (XRD) with Cu Kα radiation (λ = 0.154 nm) was used to characterize the crystallographic structure of the as-prepared magnetite nanoparticles. A scan rate of 0.034 ^{o}/s was applied to record the pattern in the 2θ range of 20^{o}–80^{o}, and the accelerating voltage and current were 37.5 kV and 25 mA, respectively. Infrared spectra were collected on Nicolet Fourier transform infrared spectrometer (FTIR) using KBr pellets in the wavenumber range of 4,000 to 650 cm^{-1}. Zeta potential measurement was performed on a Malvern Zetasizer Nano ZEN 3600 at a 90^{o} scattering angle and a temperature of 25 ^{o}C. Samples were prepared in 10-mM NaCl, which should ensure that any changes in the zeta potential values obtained are not due to conductivity differences. All measured electrophoretic mobilities were converted into Zeta potential using Smoluchowski's formula. Dynamic light scattering (DLS) analysis

was also conducted on Malvern Zetasizer Nano ZEN 3600. The dispersion concentration for the measurement was approximately 0.03 mg/ml magnetite, which provides a measured count rate of around 200 kcps. Measurements were made during a period of 2 min at least three times on each sample. The magnetic measurements of the as-prepared magnetite nanoparticles were recorded on a superconducting quantum interference device (SQUID)magnetometer at 25 ^{o}C by cycling the field between -50 and 50 kOe.

Results and discussion

Water-dispersible properties of the as-prepared magnetite nanoparticles

Highly water-dispersible magnetite nanoparticles were synthesized by one-step reverse precipitation method in the presence of sodium citrate. Figure 1 shows the TEM images of the as-prepared magnetite nanoparticles with different sodium citrate concentrations. Without sodium citrate (NP-0, Fig. 1a), the resultant product was large in size (the mean diameter was 30 ± 8.6 nm) and the particles aggregated. Selected area electron diffraction (SAED) pattern displayed spotty diffraction rings (Fig. 2). Table 1 compared the experimental d values and the literature d values; correspondingly, the rings from inside to outside can be indexed to (220), (331), (400), (511), and (440) planes of spinel Fe_3O_4, respectively. As seen from Fig. 1a (bottom right inset), the magnetite nanoparticles tended to precipitate and actually visible sedimentation of the aqueous suspension could be seen after standing for 3 h, which was due to the absence of electrostatic stabilizer to reduce the surface energy. With the addition of sodium citrate, monodispersible and well water-dispersible magnetite nanoparticles were achieved and the size and morphology of the magnetite nanoparticles could be controlled by changing

the amount of sodium citrate. Figure 1b–f shows TEM images of magnetite nanoparticles synthesized with different sodium citrate concentrations. As the sodium citrate concentration increased from 25 to 125 mM, the size of the as-prepared magnetite nanoparticles decreased from 27 ± 3.8 to 4.8 ± 1.9 nm.

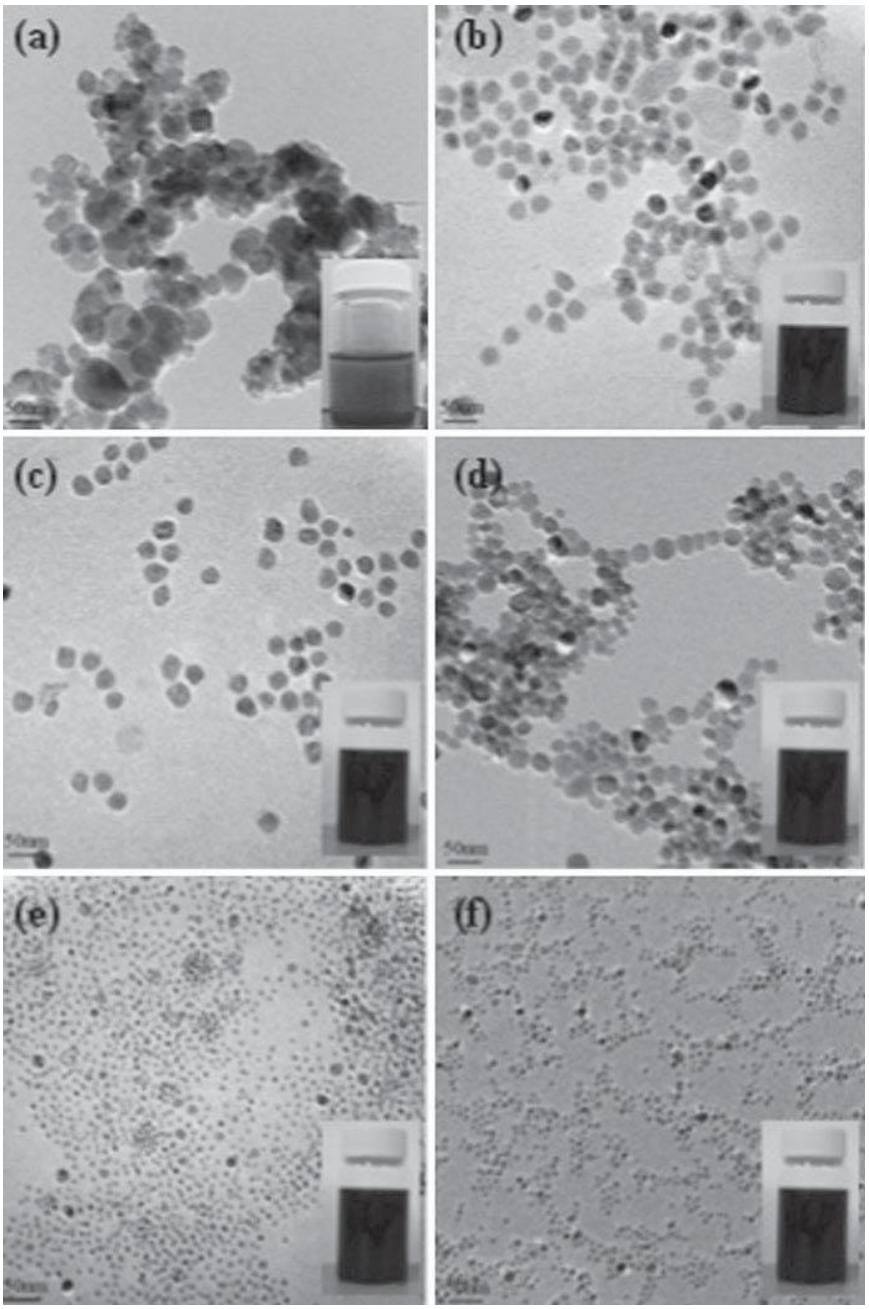

Fig. 1 TEM images of the as-prepared magnetite nanoparticles with different sodium citrate concentrations (mM). **a** 0 (NP-0, 30 ± 8.6 nm), **b** 25 (NP-25, 27 ± 3.8 nm), **c** 50 (NP-50, 23 ± 3.3 nm), **d** 75 (NP-75, 18 ± 2.9 nm), **e** 100 (NP-100, 7.3 ± 2.1 nm), and **f** 125 (NP-125, 4.8 ± 1.9 nm). The insets on the bottom right corner of each image are the resultant magnetite nanoparticle dispersions

Table 1 Experimental d-spacing from SAED (d(experiment)), d-spacing from PDF cards (d(literature)), and the corresponding crystal planes for as-prepared magnetite nanoparticles of NP-0

d (experiment, nm)	*d* (literature, nm)	Crystal plane
0.2966	0.2967	(220)
0.2539	0.2532	(311)
0.2104	0.2099	(400)
0.1615	0.1616	(511)
0.1487	0.1485	(440)

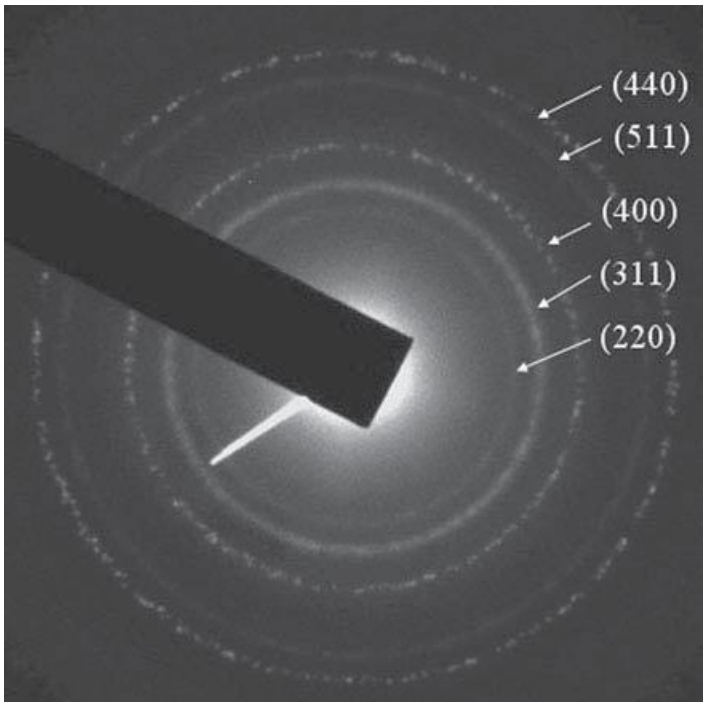

Fig. 2 Selected area electron diffraction (SAED) pattern of the as-prepared magnetite nanoparticle NP-0

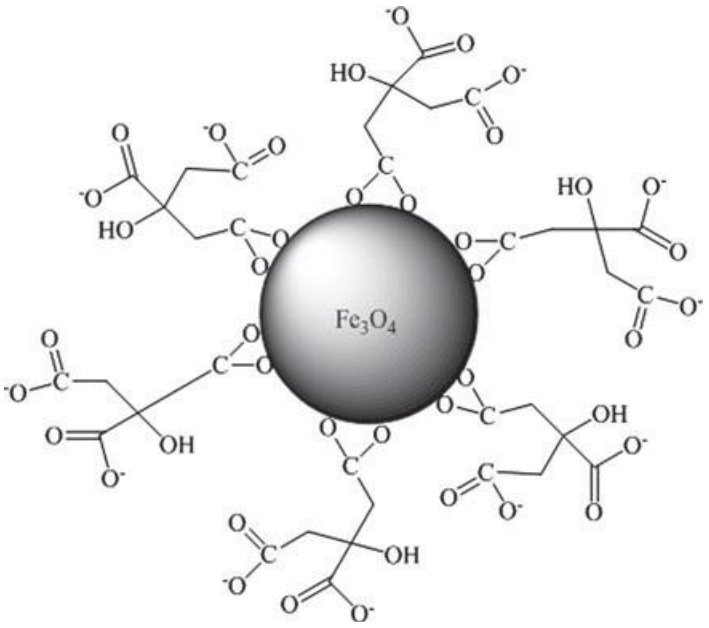

Fig. 3 Schematic illustration of the highly water-dispersible magnetite nanoparticles synthesis in the presence of sodium citrate. A fraction of carboxylate groups from sodium citrate bond to magnetite nanoparticle surfaces and the remaining fractions extend into the surrounding water, endowing the magnetite nanoparticles high water-dispersibility

It is well-known that sodium citrate is a chelating ligand with strong coordinating ability. It can coordinate with electron-poor iron ions to form stable complexes. The formation of complexes greatly reduces the availability of free iron ions in aqueous solution, resulting in a slow growth rate that is crucial for the formation of well dispersed spherical nanoparticles (Yu, Wang *et al.* 2003). In our one-step reverse precipitation method, the initial KOH solution created an alkaline atmosphere that was enough to fully hydrolyze the Fe^{2+} ions (the reaction can be described as Eqs. 1–4), so that both the nucleation and growth were relatively fast. With the addition of sodium citrate, the carboxylate groups coordinated to the iron ions. When the amount of sodium citrate increased, there were more carboxylate groups available to coordinate with iron ions, resulting in less free iron ions available in aqueous solution and therefore slowed down

the growth rate, contributed to the narrow size distribution of the resultant nanoparticles. On the other hand, with the addition of sodium citrate, some carboxylate groups of sodium citrate could strongly anchor on the surface of the produced magnetite nanoparticles to form a stable surface coating, while the uncoordinated carboxylate groups of sodium citrate extended into the aqueous solution, providing the particles a high degree of dispersibility in water (a simple illustration is presented in Fig. 3). In this process, the as-prepared magnetite nanoparticles were negatively charged, resulting in electrostatic repulsion between each particle and prevented the nanoparticles from aggregation. As the sodium citrate concentration increased, the electrostatic repulsion became stronger, offering the as-prepared magnetite nanoparticles better water dispersible stability.

$$Fe^{2+} + 2OH^- \rightarrow Fe(OH)_2 \quad (1)$$

$$3Fe(OH)_2 + NO_3^- \rightarrow Fe_3O_4 + NO_2^- + 3H_2O \quad (2)$$

$$3Fe(OH)_2 + NO_2^- \rightarrow Fe_3O_4 + NO + 2H_2O + 2OH^- \quad (3)$$

$$3Fe(OH)_2 + 2NO \rightarrow 5Fe_3O_4 + 2NH_3 + 12H_2O \quad (4)$$

(2) + (3) + (4), the reaction equation can be described as following:

$$12Fe(OH)_2 + NO_3^- \rightarrow 4Fe_3O_4 + NH_3 + 10H_2O + OH^- \quad (5)$$

X-ray diffraction (XRD) was employed to characterize the structures of the as-prepared magnetite nanoparticles. Figure 4 shows the XRD patterns of samples obtained from different sodium citrate concentration. It is found that the intensities and the d values of the peaks in the obtained XRD patterns match well with Fe_3O_4 (JCPDS no. 019-0629). The diffraction peak broadening suggests the small sizes of magnetite

nanoparticles. Based on the calculation from Scherrer's formula for the strongest diffraction peak (311), the crystal grain size of the magnetite particles decreased dramatically from 34.3 to 24.7 and to 5.4 nm when the initial sodium citrate concentration increased from 0 to 25 and to 125 mM, which is in good agreement with the average diameters measured from TEM. The accordant results about the domain size indicate the single crystalline nature of the nanoparticles.

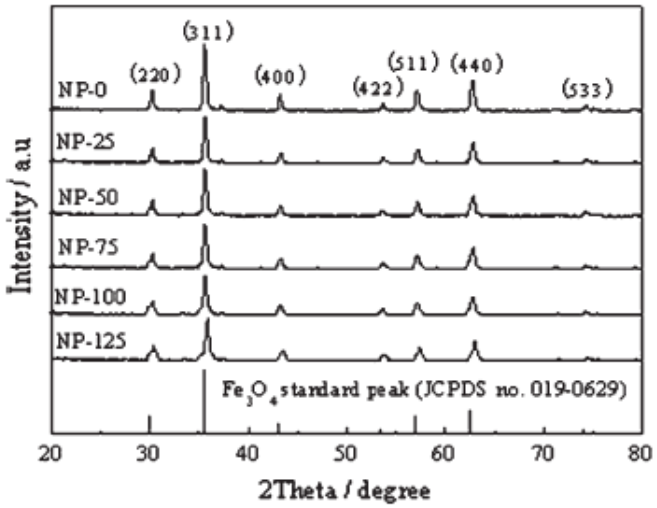

Fig. 4 X-ray diffraction patterns of the as-prepared magnetite nanoparticles with different sodium citrate concentration and an XRD pattern from the standard Fe_3O_4 powder diffraction data (JCPDS no. 019-0629). The crystal grain sizes calculated from Scherrer's formula for the strongest diffraction peak (311) are 34.3 (NP-0, 25 mM), 24.7 (NP-25, 25 mM), 20.3 (NP-50, 50 mM), 16.1 (NP-75, 75 mM), 8.7 (NP-100, 100 mM), and 5.4 nm (NP-125, 125 mM), respectively

The strong coordination of carboxylate groups ($–COO^-$) with surface iron ions contributes greatly to the surface coating of sodium citrate on the magnetite nanoparticles. To testify the adsorption of $–COO^-$ on magnetite surface, FTIR analysis of agnetite nanoparticles synthesized with different sodium citrate concentration was performed (Fig. 5). The bands at 1,589 and 1,381 cm^{-1} are associated with $–COO^-$

symmetric and antisymmetric stretchings, respectively. It is verified that sodium citrate covalently bond on the particle surface through the interaction between the $–COO^-$ of sodium citrate and the iron ions. The bands at 1,083 and 3,430 cm^{-1} area scribed to the C–H vibration and O–H vibration, respectively. Typical bands assigned to the Fe–O stretching are at around 700 cm^{-1}. For comparison, Fig. 5 also presents the FTIR spectra of pure sodium citrate and the magnetite nanoparticles without sodium citrate (NP-0). By comparing these spectra, a large amount of carboxylate groups obviously exist on the surface of the as-prepared magnetite nanoparticles.

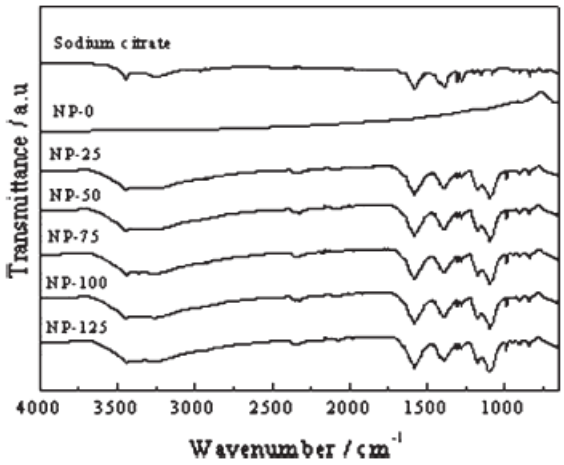

Fig. 5 FTIR spectra of pure sodium citrate and magnetite nanoparticles synthesized with different sodium citrate concentrations: NP-0 (0 mM), NP-25 (25 mM), NP-50 (50 mM), NP-75 (75 mM), NP-100 (100 mM), and NP-125 (125 mM)

Owing to the electrostatic repulsion effect, the magnetite nanoparticles synthesized with sodium citrate could be easily dispersed in water (Fig. 1b–f, insets). In contrast, magnetite particles obtained without sodium citrate show poor water-dispersibility (Fig. 1a inset). Figure 6 depicts zeta potentials of the as-prepared magnetite nanoparticles with different sodium citrate concentration. With the addition of sodium citrate, NP-25, NP-50, NP-75, NP-100, and NP-125 were highly negatively charged in

the range of pH 5–10. Furthermore, it also can be seen that zeta potentials of magnetite particles changed from -35.3 to -49.4 mV when the sodium citrate concentration increased from 25 to 125 mM at a pH 7. This endowed magnetite nanoparticles very stable water-dispersibility.

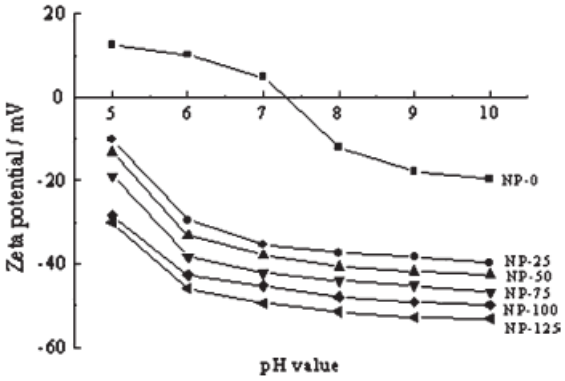

Fig. 6 Zeta potentials of magnetite nanoparticles synthesized with different sodium citrate concentrations: NP-0 (0 mM), NP-25 (25 mM), NP-50 (50 mM), NP-75 (75 mM), NP-100 (100 mM), and NP-125 (125 mM)

Hydrodynamic size variation of the as-prepared magnetite nanoparticles was investigated via dynamic light scattering (DLS) to further prove its water dispersible stability. In Fig. 7, it shows that hydrodynamic size of all the sodium citrate coating magnetite nanoparticles changed little even after 50-days staying. Take NP-125 as an example, the hydrodynamic size varied from 11.3 ± 2.4 to 12.8 ± 2.3 nm, which indicated that the magnetite nanoparticles dispersion exhibited well water-dispersible stability.

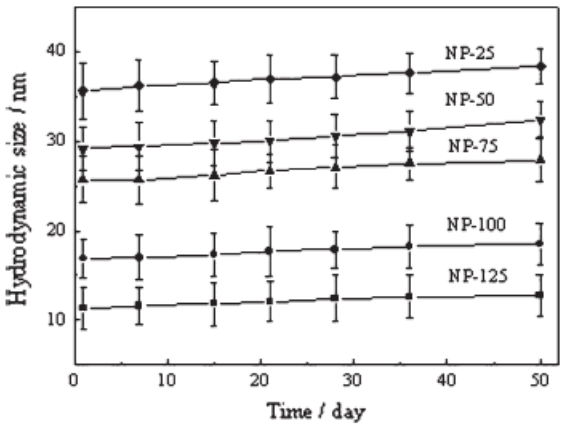

Fig. 7 Hydrodynamic size versus standing time of the magnetite nanoparticles synthesized with different sodium citrate concentrations: NP-25 (25 mM), NP-50 (50 mM), NP-75 (75 mM), NP-100 (100 mM), and NP-125 (125 mM)

For biomedical applications, the use of nanoparticles that possess superparamagnetic behavior at room temperature (no remanence along with a quickly varying magnetic state) is preferred. It is also known that magnetite nanoparticles smaller than approximately 20–30 nm in size contain a single magnetic domain with a single magnetic moment and exhibit superparamagnetism (Dave and Gao 2009). To evaluate the magnetic response of the as-prepared magnetite nanoparticles to an external field, the saturation magnetization (M_s) of the as-prepared magnetite nanoparticles was measured via a superconducting quantum interference device (SQUID) magnetometer. Figure 8 shows that NP-25 (27 ± 3.8 nm), NP-75 (18 ± 2.9 nm), and NP-125 (4.8 ± 1.9 nm) are superparamagnetic at room temperature. The saturation magnetization of NP-25, NP-75, and NP-125 was determined to be 55.75, 50.27, and 47.76 emu/g, respectively, which indicated that the saturation magnetization value decreased with the increase of the sodium citrate concentration. This phenomenon is consistent with that observed in magnetite nanoparticles coated with gluconic acid (Wei, Wei *et al.* 2011), poly(acrylic acid) (Ge, Hu *et al.* 2007), and poly(methacrylic acid) (Yu and Chow 2004). It was reported that the magnetic behavior of magnetite nanoparticles is very sensitive to

particles size (Yoon, Kotsmar *et al.* 2011). Thus, the decreased saturation magnetization values may be attributed to the decrease in the magnetite nanoparticles sizes or the high weight fraction of sodium citrate in small particles.

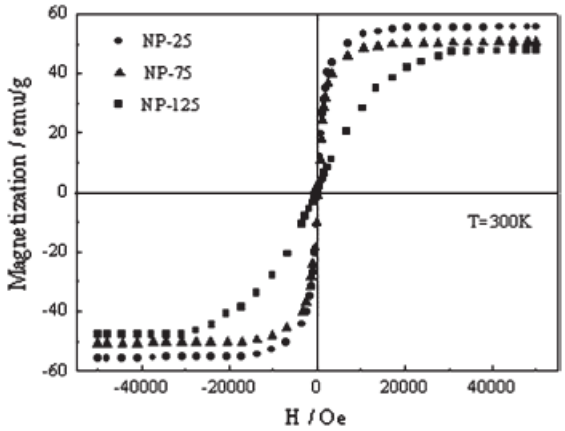

Fig. 8 Room temperature magnetization curves of magnetite nanoparticles synthesized with sodium citrate concentrations of 25 mM (NP-25), 75 mM (NP-75), and 125 mM (NP-125)

Conclusion

A facile one-step reverse precipitation method is developed for the controlled synthesis of water-dispersible, biocompatible, and carboxylate-functionalized superparamagnetic magnetite nanoparticles. Different sized magnetite nanoparticles can be obtained simply by varying the sodium citrate concentration. The sodium citrate concentration also influenced the water-dispersible stability of the as-prepared magnetite nanoparticles because of the electrostatic repulsion.

References

Baldi, G., D. Bonacchi, *et al.* (2007). "Synthesis and coating of cobalt ferrite nanoparticles: A first step toward the obtainment of new magnetic nanocarriers." Langmuir 23(7): 4026-4028.

Cheng, C., Y. Wen, *et al.* (2009). "Tunable synthesis of carboxyl-functionalized magnetite nanocrystal clusters with uniform size." Journal of Materials Chemistry 19(46): 8782-8788.

Dave, S. R. and X. Gao (2009). "Monodisperse magnetic nanoparticles for biodetection, imaging, and drug delivery: a versatile and evolving technology." Wiley Interdisciplinary Reviews-Nanomedicine and Nanobiotechnology 1(6): 583-609.

Deng, Y., D. Qi, *et al.* (2008). "Superparamagnetic high-magnetization microspheres with an Fe_3O_4@SiO_2 core and perpendicularly aligned mesoporous SiO_2 shell for removal of microcystins." Journal of the American Chemical Society 130(1): 28-29.

Fang, H., C.-y.Ma, *et al.* (2007)."Fabrication of monodisperse magnetic Fe_3O_4-SiO_2 nanocomposites with core-shell structures." Journal of Physical Chemistry C 111(3): 1065-1070.

Ge, J., Y. Hu, *et al.* (2007). "Superparamagnetic magnetite colloidal nanocrystal clusters." Angewandte Chemie-International Edition 46(23): 4342-4345.

Ge, J., Y. Hu, *et al.* (2007). "One-step synthesis of highly water-soluble magnetite colloidal nanocrystals." Chemistry-a European Journal 13(25): 7153-7161.

Gupta, A. K. and M. Gupta (2005)."Synthesis and surface engineering of iron oxide nanoparticles for biomedical applications." Biomaterials 26(18): 3995-4021.

Jana, N. R., Y. F. Chen, *et al.* (2004). "Size- and shape-controlled magnetic (Cr, Mn, Fe, Co, Ni) oxide nanocrystals via a simple and general approach." Chemistry of Materials 16(20): 3931-3935.

Laurent, S., D. Forge, *et al.* (2008). "Magnetic iron oxide nanoparticles: Synthesis, stabilization, vectorization, physicochemical characterizations, and biological applications." Chemical Reviews 108(6): 2064-2110.

Miguel-Sancho, N., O. Bomati-Miguel, *et al.* "Development of Stable, Water-Dispersible, and Biofunctionalizable Superparamagnetic Iron Oxide Nanoparticles." Chemistry of Materials 23(11): 2795-2802.

Mizukoshi, Y., T. Shuto, *et al.* (2009). "Preparation of superparamagnetic magnetite nanoparticles by reverse precipitation method: Contribution of sonochemically generated oxidants." Ultrasonics Sonochemistry 16(4): 525-531.

Park, J., K. J. An, *et al.* (2004)."Ultra-large-scale syntheses of monodisperse nanocrystals." Nature Materials 3(12): 891-895.

Prakash, A., H. Zhu, *et al.* (2009). "Bilayers as Phase Transfer Agents for Nanocrystals Prepared in Nonpolar Solvents." Acs Nano 3(8): 2139-2146.

Qiao, R., C. Yang, *et al.* (2009). "Superparamagnetic iron oxide nanoparticles: from preparations to in vivo MRI applications." Journal of Materials Chemistry 19(35): 6274-6293.

Qu, H., D. Caruntu, *et al.* "Water-Dispersible Iron Oxide Magnetic Nanoparticles with Versatile Surface Functionalities." Langmuir 27(6): 2271-2278.

Shukla, A., M. K. Patra, *et al.* "Preparation and Characterization of Biocompatible and Water-Dispersible Superparamagnetic Iron Oxide Nanoparticles (SPIONs)." Advanced Science Letters 3(2): 161-167.

Sugimoto, T. and E. Matijevic (1980)."Formation of Uniform Spherical Magnetite Particles by Crystallization from Ferrous Hydroxide Gels." Journal of Colloid and Interface Science 74(1): 227-243.

Tanaka, T., R. Shimazu, *et al.* (2009)."Preparation of spherical and uniform-sized ferrite nanoparticles with diameters between 50 and 150 nm for biomedical applications." Journal of Magnetism and Magnetic Materials 321(10): 1417-1420.

Teja, A. S. and P.-Y.Koh (2009)."Synthesis, properties, and applications of magnetic iron oxide nanoparticles." Progress in Crystal Growth and Characterization of Materials 55(1-2): 22-45.

Tung, W. S. and W. A. Daoud (2009). "New Approach Toward Nanosized Ferrous Ferric Oxide and Fe(3)O(4)-doped Titanium Dioxide Photocatalysts." Acs Applied Materials &Interfaces 1(11): 2453-2461.

Wei, X., Z. Wei, *et al.* (2011). "Highly water-soluble nanocrystal powders of magnetite and maghemite coated with gluconic acid: Preparation, structure characterization, and surface coordination." Journal of Colloid and Interface Science 354(1): 76-81.

Xiao, L., J. Li, *et al.* "Water-Soluble Superparamagnetic Magnetite Nanoparticles with Biocompatible Coating for Enhanced Magnetic Resonance Imaging." Acs Nano 5(8): 6315-6324.

Yao, K. F., Z. Peng, *et al.* (2009). "Preparation and Photocatalytic Property of TiO_2-Fe_3O_4 Core-Shell Nanoparticles." Journal of Nanoscience and Nanotechnology 9(2): 1458-1461.

Yoon, K. Y., C. Kotsmar, *et al.* "Stabilization of Superparamagnetic Iron Oxide Nanoclusters in Concentrated Brine with Cross-Linked Polymer Shells." Langmuir 27(17): 10962-10969.

Yu, S. and G. M. Chow (2004). "Carboxyl group (-CO2H) functionalized ferrimagnetic iron oxide nanoparticles for potential bio-applications." Journal of Materials Chemistry 14(18): 2781-2786.

Yu, W. W., E. Chang, *et al.* (2006). "Aqueous dispersion of monodisperse magnetic iron oxide nanocrystals through phase transfer." Nanotechnology 17(17): 4483-4487.

Yu, W. W., J. C. Falkner, *et al.* (2004). "Synthesis of monodisperse iron oxide nanocrystals by thermal decomposition of iron carboxylate salts." Chemical Communications (20): 2306-2307.

Yu, W. W., Y. A. Wang, *et al.* (2003). "Formation and stability of size-, shape-, and structure-controlled CdTe nanocrystals: Ligand effects on monomers and nanocrystals." Chemistry of Materials 15(22): 4300-4308.

APPENDIX 4: BILAYERS AS PHASE TRANSFER AGENTS FOR NANOCRYSTALS PREPARED IN NONPOLAR SOLVENTS

Bilayers as Phase Transfer Agents for Nanocrystals Prepared in Nonpolar Solvents

Arjun Prakash,† Huiguang Zhu,‡ Christopher J. Jones,‡ Denise N. Benoit,‡ Adam Z. Ellsworth,‡ Erika L. Bryant,‡ and Vicki L. Colvin†,‡,*

†Department of Chemical and Biomolecular Engineering and ‡Department of Chemistry, Rice University, Houston, Texas 77005

ACS Nano 3(8), 2139-2146

ABSTRACT

The effective water dispersion of highly uniform nanoparticles synthesized in organic solvents is a major issue for their broad applications. In an effort to overcome this problem, iron oxide and cadmium selenide nanocrystals were surrounded by lipid bilayers to create stable, aqueous dispersions. The core inorganic particles were originally generated in oleic acid and 1-octadecene. When these organic solutions were mixed with water and a sparing amount of excess fatty acid, up to 70% of the nanoparticles transferred into the aqueous phase. This simple approach was applied to two different nanocrystal types, and nanocrystal diameters ranging from 5 to 15 nm. In all cases, the resulting materials were stable, nonaggregated suspensions that retained their original magnetic and optical properties. The phase transfer efficiency is maximum when very little oleic acid is added (*e.g.* 0.2 w/w %). At higher concentrations, above the critical micelle concentration, the formation of micelles begins to compete with bilayer generation leading to less effective phase transfer. Unlike other approaches for water dispersion that rely on amphiphiles with significant water solubility, the fatty acids used in this work are only sparingly soluble in water. As a result, there is minimal dynamic

exchange between free and bound surface agents and the resulting aqueous solutions contain little residual free organic carbon. Thermogravimetric analysis (TGA) confirmed the presence of bilayers around the nanocrystal cores. The particle size, size distribution, process yield, and colloidal stability were found using a suite of methods including transmission electron microscopy, small angle X-ray scattering, dynamic light scattering, inductively coupled plasma-optical emission spectroscopy, and ultraviolet-visible spectroscopy. Bilayer-nanocrystal complexes possess many of the same size-dependent features as the original materials, and as such offer new avenues for exploring and exploiting the interface between nanocrystals and biology.

KEYWORDS: bilayer-nanocrystal · iron oxide · quantum dots · SAXS · fatty acid · nonpolar

The phase transfer of nanoparticles from nonpolar to polar suspensions remains an outstanding challenge for material chemists. The best quality nanocrystals, with respect to uniformity, size control, and crystallinity, are generally formed in organic solutions at elevated temperatures (Murray, Norris *et al.* 1993; Battaglia and Peng 2002; Dubertret, Skourides *et al.* 2002; Kim, Lim *et al.* 2004; Yu, Falkner *et al.* 2004). These synthetic methods produce nanomaterials as diverse as gold, cadmium selenide, and iron oxide which as a consequence of their formation conditions possess surfaces that terminate in organic, nonpolar moieties. However, to apply the unique optical and magnetic properties of these nanocrystals often requires surface modifications that yield well dispersed and nonaggregated materials stable in water (Shen, Laibinis *et al.* 1999; Woo and Hong 2005; De Palma, Peeters *et al.* 2007; Qin, Laurent *et al.* 2007). Nanoscale iron oxides, for example, in water purification as well as magnetic resonance imaging must be used in aqueous solutions (Kim, Wi *et al.* 2006; Yavuz, Mayo *et al.* 2006; Qin, Laurent *et al.* 2007). Quantum dots find enormous application as biological imaging agents, a technology that requires compact and isolated particles whose surfaces are compatible with a variety of biological fluids (Bruchez, Moronne *et al.* 1998; Chan and Nie 1998; Michalet, Pinaud *et al.* 2005). These and other uses for nanocrystals have sustained interest in this topic for nearly a decade; researchers have focused on methods that are both efficient in their transfer of nanocrystals and capable of preventing material aggregation and dissolution (Rembaum 1983; Veiga, Ryan *et al.* 2000; Dubertret, Skourides *et al.* 2002; Sun, Zeng *et al.* 2004; Yu, Chang *et al.* 2006; Lattuada and Hatton 2007; Chen, Thakar *et al.* 2008).

Many of the existing strategies for nanocrystal phase transfer use lipids as essential components of amphiphilic surface coatings (Wooding, Kilner *et al.* 1991; Shen, Laibinis *et al.* 1999; Dubertret, Skourides *et al.* 2002). One commercial quantum dot material reports the use of a proprietary PEG-lipid to create a stable and water-soluble material (Technologies). In these examples, the lipids-typically fatty acids-function as the nonpolar constituent of larger amphiphiles (*e.g.*, surfactants). Their hydrophobic tail interacts with the nanocrystal's nonpolar organic surface and leads to a full encapsulation of the core and its original coating. The hydrophilic end of the amphiphile is thus left to stabilize the new surface and renders the material polar and fully dispersed in water. This encapsulation approach ensures that the nanoparticle surfaces are never stripped of their original organic coatings. As a result, particle aggregation is minimized due to the presence of steric stabilization during the entire phase transfer process. Also, in the case of quantum dots, encapsulation is strongly preferred as it prevents degradation of the desirable optical properties (Aldana, Wang *et al.* 2001; Dubertret, Skourides *et al.* 2002). Nanocrystal encapsulation can be problematic in some circumstances as the size of the resulting core and surface treatment can be much larger than the starting organic material; moreover, it often requires expensive or customized copolymers and surfactants (De Palma, Peeters *et al.* 2007; Lattuada and Hatton 2007). Still there are good examples of phase transfer strategies that can produce nonaggregated and stable nanocrystal dispersions in water (Rembaum 1983; Veiga, Ryan *et al.* 2000; Yu, Chang *et al.* 2006; Lattuada and Hatton 2007; Yu, Chang *et al.* 2007; Chen, Thakar *et al.* 2008). These efforts include encapsulation using polymers (*e.g.*, polyacrylic acid, polyethylene glycol)

and ligand exchange using moieties such as bifunctional thiols (Xie, Chen *et al.* 2008; Choi, Ipe *et al.* 2009).

Whatever the surface agent selected to affect a phase transfer, it is generally desirable that the resulting nanocrystal suspensions contain little free surfactant or other organic species. Such a criterion is particularly important for biomedical and toxicological studies (Lacava, Azevedo *et al.* 1999; Hilger, Fruhauf *et al.* 2003; Pisanic, Blackwell *et al.* 2007). Conventional practice relies on sedimentation or filtration to concentrate and purify nanoparticles. These treatments can be intrinsically limited if nanocrystal surface coatings are themselves soluble in water. Unless cross-linked or otherwise irreversibly attached to the nanoparticle, most surface-bound amphiphiles will exist in equilibrium with their free form (Shen, Gleason *et al.* 2002). As a result, coatings can be removed if nanocrystals are repeatedly washed or diluted. Moreover, the dynamic exchange of the encapsulating agents can result in an adventitious adsorption of other materials, yielding a nanocrystal interface quite different from the one originally engineered (Linse, Cabaleiro-Lago *et al.* 2007). Perhaps the most significant consequence of labile surface coatings is that nanocrystal suspensions must necessarily contain some quantity of the soluble, free surfactant.

These issues motivated our interest in an alternative approach to nanoparticle phase transfer. Our goal was to form small, stable, and nonaggregated nanocrystals in water whose size-dependent properties were preserved; however, we wanted to achieve these features by using a surface coating that in its pure form would have extremely low water solubility. To achieve this end, we use a phase transfer process that generates a fatty acid bilayer at the nanoparticle interface (Figure 1B). The term “bilayer” in this

work is directed toward lipid bilayers, where both the layers are made up of the same moiety. We selected a fatty acid, oleic acid, whose monomer is highly insoluble in water. However, in its bilayer form it presents a stable and polar interface well suited for a variety of physiological environments. Our methods were inspired by efforts to sterically stabilize iron oxide colloids. For colloids formed in water, phase transfer due to bilayer formation is not the goal as it is in this work. Instead, bilayers are used to slow or reverse colloidal particle aggregation; many water soluble amphiphiles have been demonstrated for this purpose including SDBS (Shimoiizaka, Nakatsuka *et al.* 1980), dodecanoic acid (Khalafalla and Reimers 1980), alkanoic acids (Wooding, Kilner *et al.* 1991; Shen, Laibinis *et al.* 1999), phospholipids (Decuyper and Joniau 1988), and PLURONIC block copolymers (Morales, Jain *et al.* 2005). This literature provides an important conceptual foundation for this effort and offers highly relevant examples of bilayer-nanoparticle characterization.

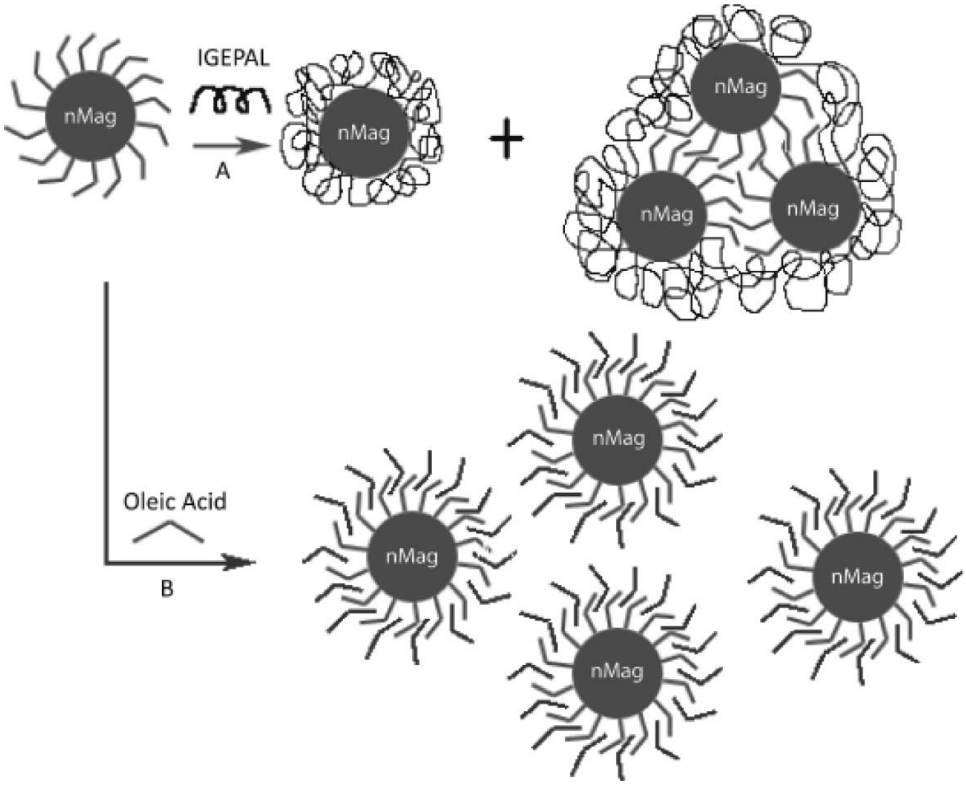

Figure 1 Illustration of the aqueous transfer of iron oxide nanoparticles (nMag) *via* both **(A)** addition of IGEPAL CO 630 surfactant; polymeric surfactants can result in the formation of clusters of nanoparticles in the final aqueous suspensions **(B)** bilayer formation.

Here we show the results of a versatile and simple approach to the generation of bilayer stabilized nanocrystals, entities that we term "bilayer-nanocrystal complexes". While most of the examples provided in this effort center on iron oxide nanocrystals, we also have explored the stabilization of quantum dots as illustrated in our study of phase transfer efficiency. The resulting materials possess small hydrodynamic sizes and are stable under a wide range of physiological conditions. SAXS indicates that in contrast to systems stabilized by polymeric surfactants, bilayer-nanocrystal complexes are nonaggregated in water. Little free fatty acid or other organic carbon is measurable in the nanocrystal aqueous suspensions, a result anticipated given the low aqueous solubility of

free oleic acid. Bilayer nanocrystal complexes retain their size dependent physical properties in water.

RESULTS AND DISCUSSION

This work focuses on a relatively unexplored avenue for creating stable aqueous suspensions of nanocrystals from organic solutions: namely, the generation of fatty acid bilayers around the original hydrophobic particles. Figure 1B illustrates the process studied in this work and contrasts it to the more conventional use of polymeric surfactants (Figure 1A) to affect nanocrystal phase transfer. Both methods use amphiphiles to change the interfacial chemistry of particles from nonpolar to polar. The standard approach relies on the hydrophobic blocks of amphiphilic polymers to wrap the nonpolar surfaces of particles or groups of particles. Of interest here is the application of molecular fatty acids, identical to those already present at quantum dot and iron oxide interfaces, as phase transfer agents. In the nonpolar nanocrystal solutions these fatty acids form dense and compact coatings with the hydrocarbon tail oriented toward the solution phase. We reasoned that if slightly more fatty acid is added, and the systems appropriately mixed, a second layer of fatty acid could be laid down on top of the original one. The process would result in the formation of a bilayer-nanocrystal complex that would present polar groups at the particle interface and subsequently lead to particle dispersion in water.

To explore this approach, oleic acid - a C18 unsaturated fatty acid - was added as a phase transfer agent to an oil/water mixture of iron oxide or cadmium selenide nanocrystals. The choice of oleic acid was motivated by several factors: its hydrophobic

tail is long enough to interact with existing hydrophobic coatings; it has poor micelle forming ability due to the presence of a double bond; and finally it is a simple choice as oleic acid is the native fatty acid used in the nanocrystal synthesis (Wooding, Kilner *et al.* 1991). Under the appropriate mixing conditions, for example probe sonication, the colored nanocrystals could be transferred from the organic to aqueous layers with high (>70%) efficiency. Several characterization methods were then applied to confirm that the surfaces of the nanoparticles in water were covered in bilayers; among these thermo-gravimetric analysis (TGA) is the most conclusive for these structures.

During controlled heating of sample residues, two distinct weight loss peaks can be observed. These correlate well in temperature to those reported for fatty acid double layers in a variety of environments (Figure 2) (Shen, Laibinis *et al.* 1999). The mass loss between 400 and 500 °C corresponds to the desorption of the outer layer of oleic acid; as expected, it occurs at a temperature slightly higher than the boiling point of neat oleic acid or 360 °C at 760 mm Hg (Young 2002; Young 20025). A second inflection point occurs between 650 and 800 °C. This feature arises from the loss of more tightly bound oleic acid. This inner layer of oleic acid is thought to be stabilized *via* a complex between iron(II) and the carboxylate groups of oleic acid (Shen, Laibinis *et al.* 1999; De Palma, Peeters *et al.* 2007). As a result, it can only be removed from the surface at higher temperatures. Also, we note that the weight loss difference between the outer and inner layers can be semiquantitatively attributed to the higher curvature of the smaller 10 nm particle in comparison with the bigger 17 nm particle. The coincidence of the TGA peak temperatures in these samples with that reported previously for bilayers, both on surfaces

and colloids, is strong evidence that under our process conditions the materials are stabilized by oleic acid bilayers (Landfester and Ramirez 2003).

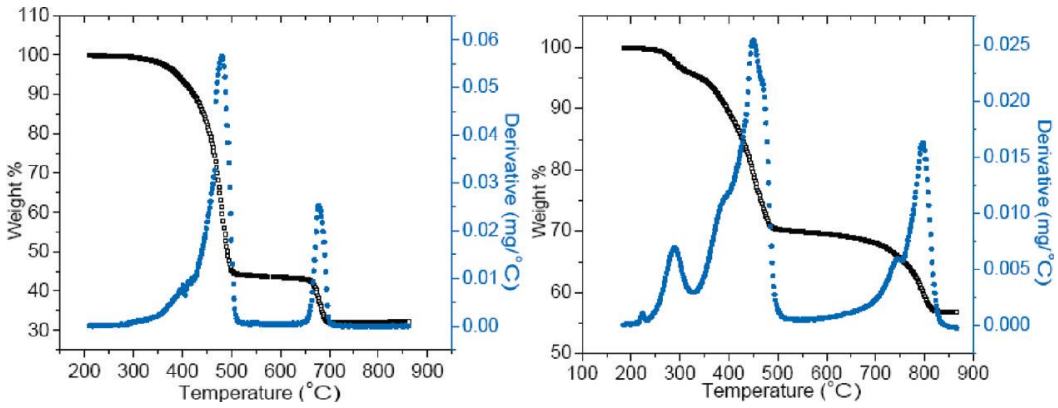

Figure 2 Thermo-gravimetric analysis (TGA) curves for 10 nm (left) and 17 nm (right) iron oxide nanocrystals. The black dots indicate the percent weight as a function of temperature and the weight loss derivative is indicated in blue. In both the cases, sample mass remained constant while cooling from 900 to 50 °C.

The formation of bilayers around the nanocrystal surfaces is also consistent with the strong sensitivity of process yield to fatty acid concentration (Figure 3). A striking feature of these data is the extremely low quantities of fatty acid required to obtain high phase transfer yields (Figure 3). For both quantum dots and iron oxide nanocrystals, over 70% of the material is transferred from hexanes to water after the addition of only 0.2 w/w% oleic acid. This is in stark contrast to particle stabilization with IGEPAL CO 630 which requires more than 10 w/w% for reasonable phase transfer yields (Yavuz, Mayo *et al.* 2006). This observation is likely due to the competition between oleic acid micelle and bilayer formation. At or near its critical micelle concentration (CMC), oleic acid can form micelles in water, and this process would remove bilayer material from the surface and reduce the solubility in water (Murakami, Chan *et al.* 1986; Jakubowski 2002). As a result, the optimal phase transfer efficiency is obtained near the CMC for oleic acid. This

observation may explain why reports of bilayer phase transfer methods for highly uniform nanocrystals are limited: conventional practice involves the addition of a vast excess of phase transfer agent to a suspension in order to ensure an efficient process. As apparent in Figure 3, such an approach would depress the transfer efficiencies substantially. In general, if bilayer formation is desired it is best to work with fatty acid concentrations (0.7-3.5mM for oleic acid) that are at or below the critical micelle concentration (Jakubowski 2002). At their highest transfer yields, the molar ratio of oleic acid to nanoparticles was found to be 90 for 10 nm iron oxide and 17 for 4 nm quantum dots. This observation between the two nanoparticle systems could be attributed to the order of magnitude difference in their surface areas.

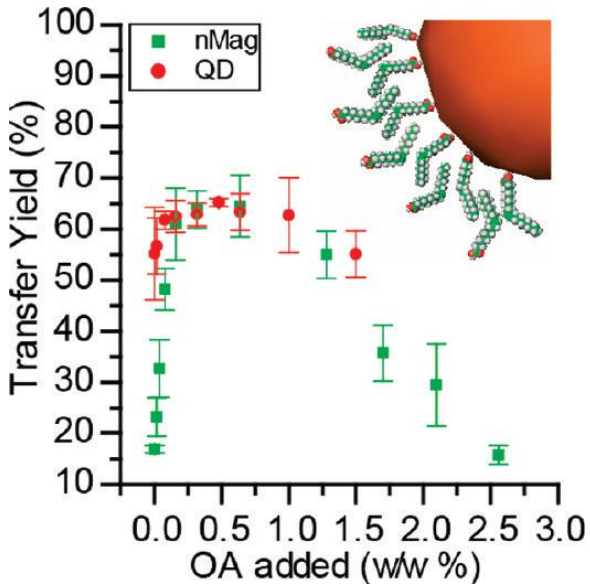

Figure 3 Variation of the transfer yield of iron oxide (nMAG) nanoparticles and quantum dots (QD) from hexanes into water as a function of oleic acid (OA) concentration. **Inset:** Scale depiction of a 10 nm diameter nanocrystal coated with a bilayer. Iron oxide concentration was obtained by ICP analysis and quantum dot concentration was obtained *via* absorbance

Also notable in Figure 3 is the similarity between the process yield for both quantum dots and iron oxide nanocrystals. Not only is the core composition different in these two cases, but the core diameters are also very different (*e.g.*, 4 nm diameter as opposed to 10 nm diameter). Still the behavior and optimization is comparable suggesting that as long as particles possess a hydrophobic surface, the addition of small amounts of fatty acid may be suitable for creating water stable dispersions.

The total organic carbon (TOC) found free in solution for the oleic acid stabilized nanoparticles is just 9 ppm, 3 orders of magnitude less than that found for equivalent polymer encapsulated (IGEPAL CO 630) materials. This observation can be explained by the different solubilities of oleic acid *versus* conventional phase transfer agents. Large amounts of polymeric surfactants like IGEPAL are required to affect nanoparticle phase separation because these materials alone have high solubility in water. An excess of free polymer in the aqueous suspensions ensures a complete and stable surface coating. In contrast, oleic acid is virtually insoluble in water (HLB value of 1) and once incorporated into a bilayer structure will not appreciably desorb from the surface (Khalafalla and Reimers 1980). The price paid for an insoluble surface stabilizing agent is the challenge associated with combining the original hydrophobic nanoparticles, free oleic acids, and water. Here we overcome this kinetic barrier by using a brief ultrasonication process which quickly mixes the various components and results in stable aqueous suspensions. While our phase transfer yields are quite high, on the order of 70%, they are not 100% effective, and this is likely due to the challenges of mixing the disparate starting materials (Figure 3). We note that it may also be possible to replace ultrasonication with elevated temperatures for more polar fatty acids and their salts (Shen, Laibinis *et al.* 1999).

An important concern for applications of nanocrystals in water is that the phase transfer process should preserve the original quality of the material as well as prevent particle aggregation. The first issue is of particular concern in this process as it relies on probe sonication to ensure adequate mixing of the insoluble fatty acids, nanocrystals, and water. The preparation of nanocrystals in organic media affords a great deal of control over nanocrystal nucleation and growth, and as a result the as-synthesized nanocrystals possess symmetric shapes, narrow size distributions, and high crystallinity (Figure 4A). These desirable features remain unchanged after the phase transfer process (Figure 4B). Most notably, each particle is well separated from its neighbors in the microscopy images, suggesting that an organic coating is associated with individual particles. Particle aggregation is not prevalent in the dried films. This observation is supported by the high clarity of the suspensions and their apparent lack of sedimentation over months (insets Figure 4).

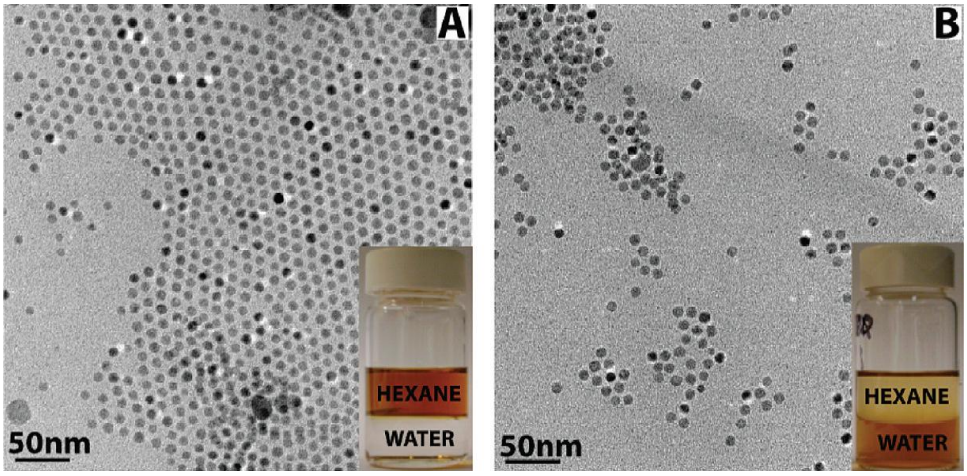

Figure 4 Transmission electron micrographs of iron oxide nanoparticles **(A)** in organics (9.6 ±1.0 nm), **(B)** phase transferred into water *via* bilayer formation (10±1 nm). Inset pictures show phase separated mixtures with water phase at the bottom and hexane phase at the top. As is clear the phase transfer efficiency is on the order of 70% as some color

remains in the organic phase. More than 1000 particles were measured to capture both the average size and the size distribution.

Direct evidence that bilayer-nanocrystal complexes are not aggregated is found in an analysis of their small angle X-ray scattering (SAXS) profiles. This method is sensitive to the presence of aggregates from 2-10 particles across, and complements well the visual observations and microscopic analysis in Figure 4 (Dabbousi, RodriguezViejo *et al.* 1997). Figure 5A,B presents the SAXS profiles for bilayer-coated iron oxide nanocrystals of 10 and 17 nm core diameters in water. The inverted scattering minima at low angles are very sensitive to the particle size distribution, and their appearance in the raw data confirm the finding from TEM that these are highly uniform samples. Models for X-ray scattering of small particles can be fit to these data to obtain more quantitative information, and these take as inputs the density, expected size, and size distribution of the particles (Rigaku-Corporation 2006). The best fits to the scattering data are shown as solid lines and the resulting overall size distributions are shown in the figure inset. As expected, the larger core sizes lead to greater diameters; moreover, the average sizes are representative of nonaggregated and fully isolated nanoparticles. These basic conclusions were confirmed by dynamic light scattering data (Table 1) which provides a semiquantitative measurement of the average hydrodynamic diameter of nanocrystals directly in suspension.

TABLE 1: Diameters of Iron Oxide Nanoparticles Dispersed in Water[a]

sample	A (nm)	B (nm))	C (nm)
TEM (core)	10.0±1.2	16.6±2.3	10.0±1.2
SAXS (core + shell)	14.3±1.8	21.5±2.6	49.0±4.8
DLS (hydrodynamic)	4.2±2.6	26.3±4.1	154.1±15.6

[a]Obtained by TEM (particle core), SAXS (particle core + shell) and DLS (hydrodynamic) for particles of size (A) 10 nm, bilayer coated; (B) 17 nm, bilayer coated; and (C) 10 nm, polymer coated.

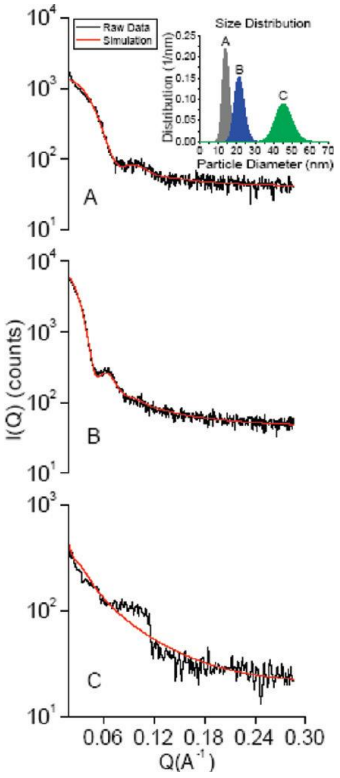

Figure 5 . Small angle X-ray scattering profiles (in black) with simulated fits (in red) for iron oxide nanoparticles in water: **(A)** 10 nm core (bilayer coated), **(B)** 17 nm core (bilayer coated), **(C)** 10 nm core (polymer coated). **Inset:** corresponding size distributions.

The hydrodynamic diameters of these materials are in good agreement with what is expected for an inorganic core surrounded by a fatty acid bilayer (Table 1). In this analysis, dimensions found from multiple characterization methods were compared to extract the effective thickness of the bilayers. TEM provides the inorganic core diameter; SAXS analysis provides a measure of the extent of the core and the dense organic coatings; and finally, DLS data reports the full hydrodynamic diameter of the bilayer-nanocrystal complex and associated hydration shell. The diameters obtained *via* SAXS and DLS for bilayer-nanocrystal complexes (sample A and sample B) are larger than the inorganic core as expected; the 4.6 nanometer difference (average of samples A and B

shell size) between the inorganic cores and the bilayer-nanoparticle complex can be attributed to the oleic acid bilayer. This corresponds to a surface coating thickness of about 2.3 nm which is comparable to the thickness of C-18 chain bilayers measured in other similar systems (Watanabe, Ono *et al.* 1985). Both in these systems, as well in other oleic acid bilayers, there is a large degree of interpenetration of the C-18 chains - a feature depicted schematically in Figure 3.7 Sample B corresponds to 17 nm core iron oxide particles coated with oleic acid bilayer. Similar bilayer dimensions were obtained *via* SAXS and DLS for this case, and these are consistent with that of the smaller sample A.

An important feature of bilayer-nanocrystal complexes highlighted by Table 1 is that they form compact structures in aqueous suspensions. Typically, the bilayer-nanocrystal complexes are only 4.6 nm larger than the core nanocrystal. Quantum dots stabilized by amphiphilic surfactants, for example, can possess hydrodynamic diameters nearly 5-10 times larger than their core diameter (Gao, Cui *et al.* 2004; Yu, Chang *et al.* 2007; Zhang, Yu *et al.* 2008).

Bilayers produced *via* oleic acid have remarkable chemical and thermal stability. The formation of a bilayer on the nanocrystal surface leads to a pH dependent charge stabilization confirmed by zeta potential measurements (-55 mV at a pH of 6.0). Figure 6 shows the visual appearance of bilayer-nanocrystal complex suspensions under different conditions of pH, ionic strength, and temperature. As expected for these systems, in acidic conditions the surface groups are protonated; above the p*K*a of oleic acid (~5.0); however, the nanocrystals are quite stable (Levasseur, Renard *et al.* 2006). The addition of salts to these suspensions can result in the precipitation of nanocrystal aggregates; the

middle panel of Figure 6 illustrates that above 250 mM the electrostatic repulsion is effectively shielded and interparticle aggregation becomes substantial. DLS confirms these visual observations. While the materials are somewhat sensitive to both charge and pH, they are remarkably stable over a variety of temperatures (bottom, Figure 6).

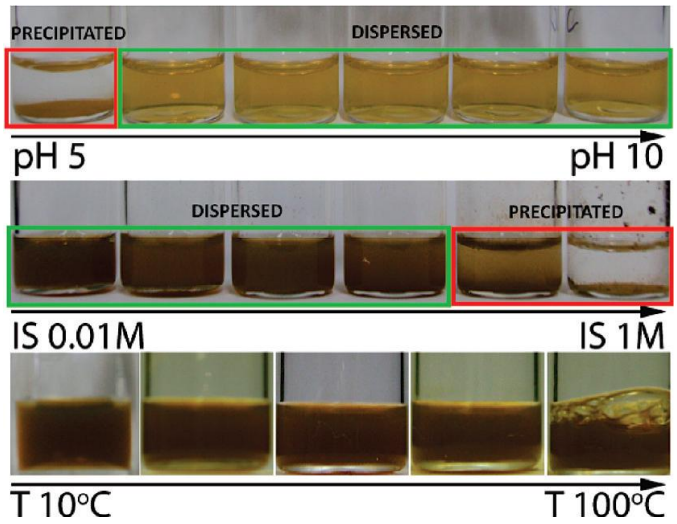

Figure 6 Iron oxide nanocrystal suspensions (10 nm core size) under varying solution phase conditions. Particles that were visibly sedimented or cloudy are surrounded by a red box; solutions with unchanged visual appearance are surrounded in green. These charge stabilized materials become unstable at low pH, when the fatty acid coatings are protonated (top panel) as well as at high ionic strengths in NaCl (middle panel). Temperature has remarkably little effect on the systems.

A delineation of the unique and valuable optical and magnetic properties of nanocrystals has been the subject of extensive prior work (Dubertret, Skourides *et al.* 2002; Michalet, Pinaud *et al.* 2005; Yavuz, Mayo *et al.* 2006; Travert-Branger, Dubois *et al.* 2008). Here, we simply confirm that the important physical properties of both of these model systems remain unchanged after transfer into water (Figure 7). Nanocrystalline iron oxide phase transferred into water can be captured by an external magnetic field; the time for capture and the overall efficiency of the process is unchanged

as would be expected given the physical characterization of the materials (Figure 4). Figure 7 also illustrates that the optical properties of quantum dots before and after bilayer stabilization are relatively unchanged. Most importantly, the quantum yield for these quantum dots systems remains within 20% of its original value after phase transfer. Complete analysis of the optical and magnetic properties of these complexes is the subject of future work. This data is presented here only to establish that the process does not significantly alter the core nanocrystal features.

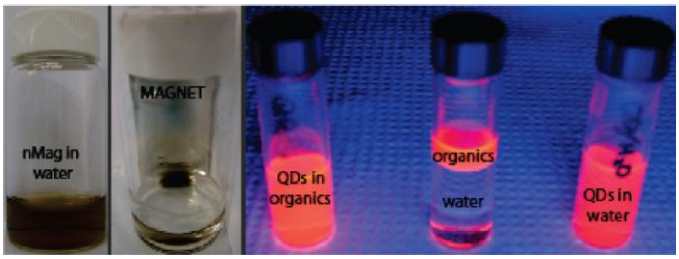

Figure 7 Optical and magnetic properties of bilayer-nanocrystal complexes are similar to the original materials. On the far left panels, a strong permanent magnet is able to concentrate the iron oxide materials (nMAG) much as is observed in hexanes. On the right panel, the fluorescence of quantum dots (QD) is relatively unchanged after the formation of a bilayer and the transfer of the material into water.

Finally, to identify the advantages of a bilayer stabilization approach we compare these results to those found using a conventional polymeric surfactant, IGEPAL CO 630. Figure 5C shows that these surfactants when applied to iron oxide nanocrystals result in particle aggregation; larger amphiphilic phase transfer agents have been reported to encapsulate multiple particles (Landfester and Ramirez 2003; Lattuada and Hatton 2007). This results in polydisperse groupings of iron oxide nanocrystals. Also, corresponding DLS diameters (Table 1, sample C) show a significant increase over the particle core size, indicating the presence of aggregates in polymer stabilized materials. These observations highlight the significant challenges faced in preventing aggregation of these

magnetic materials during phase transfer. The approach outlined in this paper, in contrast, is successful in generating isolated magnetic nanocrystals as well as quantum dots.

CONCLUSIONS

Lipid bilayers prepared from a water insoluble fatty acid can be generated around both iron oxide and cadmium selenide nanocrystals. These surface coatings form around nanoparticles after mixing hexane solutions of the materials, free fatty acids and water; thermogravimetric analysis confirms the existence of lipid bilayers. The bilayer thickness on a variety of nanocrystal cores was deduced from both dynamic light scattering and small-angle X-ray scattering; typical values of 2.2-2.5 nanometer are consistent with those reported for comparable immobilized bilayers. An interesting finding is that bilayer formation is only successful when a small amount (0.2 w/w %) of oleic acid is incorporated into the organic solutions. Phase transfer efficiencies may be depressed at higher concentrations due to the self-association of the fatty acids into micelles. An important advantage of using a highly insoluble fatty acid to affect nanocrystal phase transfer is the resulting purity of the aqueous suspension: once captured into a lipid bilayer around a nanoparticle, there is no driving force for the desorption of free fatty acid. Small angle X-ray scattering of the aqueous suspensions reveals that the materials are uniform and nonaggregated. The resulting bilayer-nanoparticle complexes are highly stable over a wide range of temperatures, ionic strength, and pH as expected for a moderately charged interface. Bilayer formation does

not change the essential size-dependent properties of nanocrystals and offers several advantages.

METHODS

Nanocrystal Synthesis

Iron oxy-hydrate (FeO(OH) iron(III) oxide, hydrated; catalyst grade, 30-50 mesh;), 1-octadecene (ODE 90%), cadmium oxide (CdO 99.99%), selenium powder (Se 100 mesh 99%), trioctylphosphine (TOP 99%), oleic acid (90%), and nitric acid (trace metal grade) were all purchased from SIGMAAldrich. The 1 μm PTFE AERODISC syringe filter was purchased from PALL LIFE SCIENCE and a 0.2 μm NYL syringe filter was purchased from WHATMAN.

Iron oxide nanoparticles were synthesized by the thermal decomposition of iron carboxylate salts (Hyeon, Lee *et al.* 2001; Yu, Falkner *et al.* 2004). A mixture of 0.178 g of FeO(OH), 2.26 g oleic acid, and 5.0 g of 1-octadecene was stirred and purged with nitrogen; moderate heating up to 280 °C in a three neck-flask led to the formation of an orange solution thought to contain iron carboxylates. Further heating to 320 °C led to a decomposition of this precursor and the generation of brown-black iron oxide nanocrystals. The reaction product was soluble in hexane because of the adsorption of oleic acid to the nanocrystal surface *via* polar, carboxylate groups.

The iron oxide nanocrystals were purified by repeated cycles of precipitation and sedimentation followed by dispersion in hexane. Reaction products were treated with a 1:1 volumetric amount of acetone and methanol leading to the formation of visible aggregates; these were collected *via* centrifugation in a pellet and could be dispersed back into hexanes. This procedure was repeated five times to remove unreacted iron salts, 1-ODE, or unbound oleic acid. Purified nanocrystal solutions in hexanes could be digested

by strong nitric acid and analyzed for their iron content with atomic emission spectroscopy (ICP-OES). Using the average diameter of the material obtained from TEM, and the density of iron oxide (5.17 g/cm3), the atomic concentration of iron could be converted into a nanoparticle concentration.

CdSe nanocrystals were prepared by heating a stirred mixture of 0.3 g of CdO and 2.7 g of oleic acid in a 100 mL three neck flask at 200 °C until a transparent liquid was obtained (Yu and Peng 2002). After cooling to room temperature, 15 g of oleic acid and 30 g of ODE were added and the mixture heated to 100 °C under vacuum for 40 min. The solution was then purged with ultrapure N_2 and heated to 300 °C. An injection solution, prepared by mixing 10.68 g of Se/TOP (10 wt %) and 4.13 g of ODE, was swiftly injected into the flask with a 20 mL syringe fitted with a large bore needle. After cooling to room temperature, the crude quantum dots were precipitated by the addition of acetone and methanol, in a fashion similar to that used for the iron oxide. These pellets could be isolated and purified after repeated centrifugation at 3500*g* followed by redispersion into hexanes. The final purified nanocrystal pellet was ultimately redispersed in hexane, filtered through 1 μm PTFE syringe filter, and stored in the dark. Quantum dot concentrations were estimated from absorbance data using methods published elsewhere (Yu, Qu *et al.* 2003).

Phase Transfer of Nanocrystals

Oleic acid was added in variable amounts (0.5-300 μL) to 1.0 mL of purified nanocrystal suspensions in hexanes (typically 1 g nanoparticle/L). The resulting solution was then sonicated in a bath for 1 min with no visible change in appearance (FS6

sonicator from FISCHER SCIENTIFIC). Next, 10 mL of ultrapure water (MILLIPORE, 18.2 MΩcm) was then added to the hexane solution resulting in an obvious phase separation between the clear water and colored nonpolar solution. To affect the transfer of material from hexanes into water, this solution was subjected to sonication *via* a probe (UP 50H probe sonciator from DR.HIELSCHER) for 5 min at 50% amplitude and full cycle. Care was taken to ensure that the tip of the probe, where the power is the highest, was located near the interfacial region between the hexanes and water phase. Immediately after sonication a cloudy and colored solution was obtained, but if left to sit undisturbed for 1 day the mixture phase separated with the colored nanoparticles appearing in the bottom, aqueous fraction. This layer was collected and the nanoparticles purified *via* centrifugation at 3500*g* for 15 min, followed by redispersion and filtration through a syringe filter (pore size of 0.2 μm, Whatman-NYL). The filtered product was a clear, colored suspension that could be further concentrated (typically 10x) *via* rotary evaporation. The above procedure was also used to phase transfer cadmium selenide nanocrystals. Methods to describe the phase transfer using IGEPAL CO 630 are described elsewhere.(Yavuz, Mayo *et al.* 2006)

Characterization of Nanocrystals

Small angle X-ray scattering (SAXS) profiles were obtained on a RIGAKU SMARTLAB system operating in transmission mode with a line collimation setup. A capillary tube (0.8 mm diameter) was filled with a sample, and the low angle scattering was collected from 2θ values of 0.15-4 degrees with a Cu Kα X-ray beam of wavelength 1.54 Å. The X-rays were generated at 40 kv and 44 mA. Typical data collection times

were on the order of 2 h. The raw scattering data was analyzed using Rigaku's NANOSOLVER software using a split interval of 30 with low slit correction factor.

Dynamic light scattering (DLS) data was collected using a BROOKHAVEN instrument equipped with a BI-9000AT digital autocorrelator using a monitoring wavelength of 656 nm. Standard 1.5 mL poly methacrylate cuvettes were used as sample holders and each sample was analyzed for 4 min to obtain a minimum intensity of 200,000 cps. A histogram of the particle diameter distribution was obtained *via* a "Contin" fit to the raw autocorrelation data.

Transmission electron microscopy (TEM) was carried out using JEOL 2100 field emission gun TEM at 200 kV with a single tilt holder using 300 mesh copper grids with holey carbon from Ted Pella Inc. Thermogravitmetric analysis (TGA) was carried out using TA INSTRUMENTS SDT 2960 simultaneous DSC-TGA instrument with sample deposited in a platinum pan. Samples were maintained at 150 °C for 5 h for removal of any associated solvent/moisture before further heating. The samples were then heated to 900 °C at the rate of 50 °C/min. UV-visible spectroscopy was carried out using Cary 5000 VARIAN UV-vis-NIR spectrophotometer with 1.5 mL polymethacrylate cuvettes used as sample holders. All sizing data with respective significant figures were reported with error bars representing their standard deviation. Inductively coupled plasma (ICP) analysis was carried out using PERKIN ELMER ICP-OES instrument equipped with autosampler. Total organic carbon content of the supernatant was computed using SHIMADZU TOC analyzer after sedimentation of particle suspension (1 mL of 1 μM) (BECKMAN-COULTER OPTIMAL-80XP ultracentrifuge) at 118,000 g for 4 h at 25 °C.

References

(1971). Acylating and similar reagents: acetic anhydride. Chemical modification of proteins. G. Means and R. Feeney. San Francisco, Holden-Day: 69-71.

Abbaszadegan, M., M. Lechevallier, *et al.* (2003). "Occurrence of viruses in US groundwaters." Journal American Water Works Association 95(9): 107-120.

Adams, M. H. (1959). Bacteriophages. New York, Interscience Publishers, Inc.

Agency, E. P. (2006a). National Primary Drinking Water Regulations: Long Term 2 Enhanced Surface Water Treatment Rule; Final Rule, Federal Register. 40: 654-786.

Agency, E. P. (2006b). National Primary Drinking Water Regulations: Ground Water Rule; Final Rule. Federal Register, Federal Register. 40: 65574-65659.

Agency, E. P. (2006c). National Primary Drinking Water Regulations: Stage 2 Disinfectants and Disinfection Byproducts Rule; Final Rule, Federal Register. 40: 387-493.

Aggarwal, P., J. B. Hall, *et al.* (2009). "Nanoparticle interaction with plasma proteins as it relates to particle biodistribution, biocompatibility and therapeutic efficacy." Advanced Drug Delivery Reviews 61(6): 428-437.

Aldana, J., Y. A. Wang, *et al.* (2001). "Photochemical instability of CdSe nanocrystals coated by hydrophilic thiols." Journal of the American Chemical Society 123(36): 8844-8850.

Asuri, P., S. S. Bale, *et al.* (2006). "The protein-nanomaterial interface." Current Opinion in Biotechnology 17(6): 562-568.

Badireddy, A. R., E. M. Hotze, *et al.* (2007). "Inactivation of Bacteriophages via photosensitization of fullerol nanoparticles." Environmental Science & Technology 41(18): 6627-6632.

Baldi, G., D. Bonacchi, *et al.* (2007). "Synthesis and coating of cobalt ferrite nanoparticles: A first step toward the obtainment of new magnetic nanocarriers." Langmuir 23(7): 4026-4028.

Battaglia, D. and X. G. Peng (2002). "Formation of high quality InP and InAs nanocrystals in a noncoordinating solvent." Nano Letters 2(9): 1027-1030.

Baudhuin, P., P. Van der Smissen, *et al.*, Eds. (1989). Molecular interactions between colloidal gold, proteins and living cells. Colloidal gold: principles, methods and applications. San Diego, Academic Press.

Belhacova, L., J. Krysa, *et al.* (1999). "Inactivation of microorganisms in a flow-through photoreactor with an immobilized TiO_2 layer." Journal of Chemical Technology and Biotechnology 74(2): 149-154.

Benabbou, A. K., Z. Derriche, *et al.* (2007). "Photocatalytic inactivation of Escherischia coli - Effect of concentration of TiO_2 and microorganism, nature, and intensity of UV irradiation." Applied Catalysis B-Environmental 76(3-4): 257-263.

Brewer, S. H., W. R. Glomm, *et al.* (2005). "Probing BSA binding to citrate-coated gold nanoparticles and surfaces." Langmuir 21(20): 9303-9307.

Bruchez, M., M. Moronne, *et al.* (1998). "Semiconductor Nanocrystals as Fluorescent Biological Labels." Science 281: 2013-2016.

Butkus, M. A., M. P. Labare, *et al.* (2004). "Use of aqueous silver to enhance inactivation of coliphage MS-2 by UV disinfection." Applied and Environmental Microbiology 70(5): 2848-2853.

Calabretta, M., J. A. Jamison, *et al.* (2005). "Analytical ultracentrifugation for characterizing nanocrystals and their bioconjugates." Nano Letters 5(5): 963-967.

Cedervall, T., I. Lynch, *et al.* (2007). "Understanding the nanoparticle-protein corona using methods to quantify exchange rates and affinities of proteins for nanoparticles." Proceedings of the National Academy of Sciences of the United States of America 104(7): 2050-2055.

Chan, W. C. W. and S. M. Nie (1998). "Quantum dot bioconjugates for ultrasensitive nonisotopic detection." Science 281(5385): 2016-2018.

Chen, B., M. Liu, *et al.* (2011). "Polyethylenimine-functionalized graphene oxide as an efficient gene delivery vector." Journal of Materials Chemistry 21(21): 7736-7741.

Chen, Y., R. Thakar, *et al.* (2008). "Imparting nanoparticle function with size-controlled amphiphilic polymers." Journal of the American Chemical Society 130(12): 3744-+.

Cheng, C., Y. Wen, *et al.* (2009). "Tunable synthesis of carboxyl-functionalized magnetite nanocrystal clusters with uniform size." Journal of Materials Chemistry 19(46): 8782-8788.

Cho, M., H. M. Chung, *et al.* (2005). "Different inactivation Behaviors of MS-2 phage and Escherichia coli in TiO_2 photocatalytic disinfection." Applied and Environmental Microbiology 71(1): 270-275.

Choi, H. S., B. I. Ipe, *et al.* (2009). "Tissue- and Organ-Selective Biodistribution of NIR Fluorescent Quantum Dots." Nano Letters 9(6): 2354-2359.

Choi, W. Y., A. Termin, *et al.* (1994). "The Role of Metal-Ion Dopants in Quantum-Sized TiO_2 - Correlation between Photoreactivity and Charge-Carrier Recombination Dynamics." Journal of Physical Chemistry 98(51): 13669-13679.

Chung, D. D. L. (2002). "Review graphite." Journal of Materials Science 37(8): 1475-1489.

Cotton, F. A., G. Wilkinson, *et al.* (1999). Advanced Inorganic Chemistry. New York, Wiley-Interscience.

Dabbousi, B. O., J. RodriguezViejo, *et al.* (1997). "(CdSe)ZnS core-shell quantum dots: Synthesis and characterization of a size series of highly luminescent nanocrystallites." Journal of Physical Chemistry B 101(46): 9463-9475.

Dave, S. R. and X. Gao (2009). "Monodisperse magnetic nanoparticles for biodetection, imaging, and drug delivery: a versatile and evolving technology." Wiley Interdisciplinary Reviews-Nanomedicine and Nanobiotechnology 1(6): 583-609.

De Palma, R., S. Peeters, *et al.* (2007). "Silane ligand exchange to make hydrophobic superparamagnetic nanoparticles water-dispersible."Chemistry of Materials 19(7): 1821-1831.

Decuyper, M. and M. Joniau (1988). "Magnetoliposomes - Formation and Structural Characterization." European Biophysics Journal with Biophysics Letters 15(5): 311-319.

Deng, Y., D. Qi, *et al.* (2008). "Superparamagnetic high-magnetization microspheres with an Fe_3O_4@SiO_2 core and perpendicularly aligned mesoporous SiO_2 shell for removal of microcystins." Journal of the American Chemical Society 130(1): 28-29.

Deroe, C., P. J. Courtoy, *et al.* (1987). "A Model of Protein Colloidal Gold Interactions." Journal of Histochemistry & Cytochemistry 35(11): 1191-1198.

Dubertret, B., P. Skourides, *et al.* (2002). "In vivo imaging of quantum dots encapsulated in phospholipid micelles." Science 298(5599): 1759-1762.

Elechiguerra, J. L., J. L. Burt, *et al.* (2005). "Interaction of silver nanoparticles with HIV-1." Journal of Nanobiotechnology 3(6).

Fang, H., C.-y.Ma, *et al.* (2007). "Fabrication of monodisperse magnetic Fe_3O_4-SiO_2 nanocomposites with core-shell structures." Journal of Physical Chemistry C 111(3): 1065-1070.

Feng, L., S. Zhang, *et al.* (2011). "Graphene based gene transfection." Nanoscale 3(3): 1252-1257.

Feng, Q. L., J. Wu, *et al.* (2000). "A mechanistic study of the antibacterial effect of silver ions on Escherichia coli and Staphylococcus aureus." Journal of Biomedical Materials Research 52(4): 662-668.

Frens, G. (1973). "Controlled Nucleation for Regulation of Particle-Size in Monodisperse Gold Suspensions." Nature-Physical Science 241(105): 20-22.

Gao, X. H., Y. Y. Cui, *et al.* (2004). "In vivo cancer targeting and imaging with semiconductor quantum dots." Nature Biotechnology 22(8): 969-976.

Ge, J., Y. Hu, *et al.* (2007). "Superparamagnetic magnetite colloidal nanocrystal clusters." Angewandte Chemie-International Edition 46(23): 4342-4345.

Ge, J., Y. Hu, *et al.* (2007). "One-step synthesis of highly water-soluble magnetite colloidal nanocrystals." Chemistry-a European Journal 13(25): 7153-7161.

Gupta, A. K. and M. Gupta (2005). "Synthesis and surface engineering of iron oxide nanoparticles for biomedical applications." Biomaterials 26(18): 3995-4021.

Haick, H. and Y. Paz (2003). "Long-range effects of noble metals on the photocatalytic properties of titanium dioxide." Journal of Physical Chemistry B 107(10): 2319-2326.

Hamza, I. A., L. Jurzik, *et al.* (2009). "Detection of human viruses in rivers of a densly-populated area in Germany using a virus adsorption elution method optimized for PCR analyses." Water Research 43(10): 2657-2668.

He, S., B. Song, *et al.* (2010)."A Graphene Nanoprobe for Rapid, Sensitive, and Multicolor Fluorescent DNA Analysis." Advanced Functional Materials 20(3): 453-459.

Hermanson, G., Ed. (1996). Introduction of primary amine groups: modification of carboxylates with diamines. Bioconjugate techniques. San Diego, Academic Press.

Hilger, I., S. Fruhauf, *et al.* (2003). "Cytotoxicity of selected magnetic fluids on human adenocarcinoma cells." Journal of Magnetism and Magnetic Materials 261(1-2): 7-12.

Hoffmann, M. R., S. T. Martin, *et al.* (1995). "Environmental Applications of Semiconductor Photocatalysis." Chemical Reviews 95(1): 69-96.

Hu, M., L. Qian, *et al.* (2007). "Assembly of nanoparticle-protein binding complexes: From monomers to ordered arrays." Angewandte Chemie-International Edition 46(27): 5111-5114.

Hyeon, T., S. S. Lee, *et al.* (2001). "Synthesis of highly crystalline and monodisperse maghemite nanocrystallites without a size-selection process." Journal of the American Chemical Society 123(51): 12798-12801.

Iliev, V., D. Tomova, *et al.* (2006). "Photocatalytic properties of TiO_2 modified with platinum and silver nanoparticles in the degradation of oxalic acid in aqueous solution." Applied Catalysis B-Environmental 63(3-4): 266-271.

Iosin, M., F. Toderas, *et al.* (2009). "Study of protein-gold nanoparticle conjugates by fluorescence and surface-enhanced Raman scattering." Journal of Molecular Structure 924-26: 196-200.

Jakubowski, H. (2002). Biochemistry Online: An Approach Based on Chemical Logic.

Jana, N. R., Y. F. Chen, *et al.* (2004). "Size- and shape-controlled magnetic (Cr, Mn, Fe, Co, Ni) oxide nanocrystals via a simple and general approach."Chemistry of Materials 16(20): 3931-3935.

Jiang, X., U. G. Jiang, *et al.* (2005). "Effect of colloidal gold size on the conformational changes of adsorbed cytochrome c: Probing by circular dichroism, UV-visible, and infrared spectroscopy." Biomacromolecules 6(1): 46-53.

Jones, M. (2005).Organic Chemistry. New York, W. W. Norton & Company, Inc.

Jou, W. M., M. Ysebaert, *et al.* (1972). "Nucleotide sequence of gene coding for bacteriophage MS2 coat protein."Nature 237(5350): 82-88.

Kaneko, M. and I. E. Okura, Eds. (2002). Photocatalysis: Science and Technology. New York, Springer.

Keating, C. D., K. M. Kovaleski, *et al.* (1998). "Protein : colloid conjugates for surface enhanced Raman scattering: Stability and control of protein orientation." Journal of Physical Chemistry B 102(47): 9404-9413.

Khalafalla, S. E. and G. W. Reimers (1980)."Preparation of Dilution-Stable Aqueous Magnetic Fluids."Ieee Transactions on Magnetics 16(2): 178-183.

Kikuchi, Y., K. Sunada, *et al.* (1997). "Photocatalytic bactericidal effect of TiO_2 thin films: Dynamic view of the active oxygen species responsible for the effect." Journal of Photochemistry and Photobiology a-Chemistry 106(1-3): 51-56.

Kim, J.-P., I.-H.Cho, *et al.* (2006). "Manufacturing of anti-viral inorganic materials from colloidal silver and titanium oxide." Revue Roumaine De Chimie 51(11): 1121-+.

Kim, S. and W. Choi (2002). "Kinetics and mechanisms of photocatalytic degradation of $(CH_3)_nNH_{4-n}+$ $(0 \leq n \leq 4)$ in TiO_2 suspension: The role of OH radicals." Environmental Science & Technology 36(9): 2019-2025.

Kim, S., Y. T. Lim, *et al.* (2004). "Near-infrared fluorescent type II quantum dots for sentinel lymph node mapping." Nature Biotechnology 22(1): 93-97.

Kim, S. J., H. S. Wi, *et al.* (2006). "Encapsulation of CdSe nanoparticles inside liposome suspended in aqueous solution." Journal of the Korean Physical Society 49: S684-S687.

Koizumi, Y. and M. Taya (2002). "Kinetic evaluation of biocidal activity of titanium dioxide against phage MS2 considering interaction between the phage and photocatalyst particles." Biochemical Engineering Journal 12(2): 107-116.

Kondo, M. M. and W. F. Jardim (1991). "Photodegradation of Chloroform and Urea Using Ag-Loaded Titanium Diode as Catalyst." Water Research 25(7): 823-827.

Laaksonen, P., J. Kivioja, *et al.* (2009). "Selective Nanopatterning Using Citrate-Stabilized Au Nanoparticles and Cystein-Modified Amphiphilic Protein." Langmuir 25(9): 5185-5192.

Lacava, Z. G. M., R. B. Azevedo, *et al.* (1999). "Biological effects of magnetic fluids: toxicity studies." Journal of Magnetism and Magnetic Materials 201: 431-434.

Lacerda, S. H. D. P., J. J. Park, *et al.* "Interaction of Gold Nanoparticles with Common Human Blood Proteins." Acs Nano 4(1): 365-379.

Landfester, K. and L. P. Ramirez (2003). "Encapsulated Magnetite Particles for Biomedical Application." Journal of Physics: Condensed Matter 15: S1345-S1361.

Lattuada, M. and T. A. Hatton (2007). "Functionalization of monodisperse magnetic nanoparticles." Langmuir 23(4): 2158-2168.

Laurent, S., D. Forge, *et al.* (2008). "Magnetic iron oxide nanoparticles: Synthesis, stabilization, vectorization, physicochemical characterizations, and biological applications." Chemical Reviews 108(6): 2064-2110.

Levasseur, B., B. Renard, *et al.* (2006). "Catalytic wet air oxidation of oleic acid on ceria-supported platinum catalyst. Effect of pH." Reaction Kinetics and Catalysis Letters 87(2): 269-279.

Liang, J. L., E. J. Dziuban, *et al.* (2006). "Surveillance for Waterborne Disease and Outbreaks Associated with Drinking Water and Water not Intended for Drinking -- United States, 2003--2004." Surveillance Summaries 55(SS12): 31-58.

Liberti, L., M. Notarnicola, *et al.* (2003). "Advanced treatment for municipal wastewater reuse in agriculture. UV disinfection: parasite removal and by-product formation." Desalination 152(1-3): 315-324.

Lim, S. I. and C.-J.Zhong (2009). "Molecularly Mediated Processing and Assembly of Nanoparticles: Exploring the Interparticle Interactions and Structures." Accounts of Chemical Research 42(6): 798-808.

Linse, S., C. Cabaleiro-Lago, *et al.* (2007)."Nucleation of protein fibrillation by nanoparticles."Proceedings of the National Academy of Sciences of the United States of America 104(21): 8691-8696.

Liu, S., M. Lim, *et al.* (2008). "TiO2 photocatalysis of natural organic matter in surface water: impact on trihalomethane and haloacetic acid formation potential." Environmental Science & Technology 42(16): 6218-6223.

Liu, X., M. Atwater, *et al.* (2007)."Extinction coefficient of gold nanoparticles with different sizes and different capping ligands."Colloids and Surfaces B-Biointerfaces 58(1): 3-7.

Liu, Z., J. T. Robinson, *et al.* (2008). "PEGylated nanographene oxide for delivery of water-insoluble cancer drugs."Journal of the American Chemical Society 130(33): 10876-10877.

Lu, C.-H., J. Li, *et al.* (2010). "Increasing the Sensitivity and Single-Base Mismatch Selectivity of the Molecular Beacon Using Graphene Oxide as the "Nanoquencher"." Chemistry – A European Journal 16(16): 4889-4894.

Lu, C.-H., C.-L.Zhu, *et al.* (2010). "Using graphene to protect DNA from cleavage during cellular delivery." Chemical Communications 46(18): 3116-3118.

Lu, C., Z. Chen, *et al.* (2008). "Optimized conditions for the self-organization of CdSe-Au and CdSe-CdSe binary nanoparticle superlattices." Chemistry of Materials 20(11): 3594-3600.

Lundqvist, M., J. Stigler, *et al.* (2008). "Nanoparticle size and surface properties determine the protein corona with possible implications for biological impacts." Proceedings of the National Academy of Sciences of the United States of America 105(38): 14265-14270.

Lydakis-Simantiris, N., D. Riga, *et al.* (2010). "Disinfection of spring water and secondary treated municipal wastewater by TiO_2 photocatalysis." Desalination 250(1): 351-355.

Lynch, I., T. Cedervall, *et al.* (2007). "The nanoparticle - protein complex as a biological entity; a complex fluids and surface science challenge for the 21st century." Advances in Colloid and Interface Science 134-35: 167-174.

Lynch, I. and K. A. Dawson (2008). "Protein-nanoparticle interactions." Nano Today 3(1-2): 40-47.

Lynch, I., A. Salvati, *et al.* (2009). " Protein-nanoparticle interactions: What does the cell see?" Nature Nanotechnology 4(9): 546-547.

Mackey, E. D., T. M. Hargy, *et al.* (2002). "Comparing Cryptosporidium and MS2 bioassays - implications for UV REACTOR validation." Journal American Water Works Association 94(2): 62-69.

McNeil-Watson, F., W. Tscharnuter, *et al.* (1998). "A new instrument for the measurement of very small electrophoretic mobilities using phase analysis light scattering (PALS)." Colloids and Surfaces a-Physicochemical and Engineering Aspects 140(1-3): 53-57.

Merlic, C. A. (2000).WebSpectra, UCLA Department of Chemistry and Biochemistry.

Michalet, X., F. F. Pinaud, *et al.* (2005). "Quantum dots for live cells, in vivo imaging, and diagnostics." Science 307(5709): 538-544.

Miguel-Sancho, N., O. Bomati-Miguel, *et al.* "Development of Stable, Water-Dispersible, and Biofunctionalizable Superparamagnetic Iron Oxide Nanoparticles."Chemistry of Materials 23(11): 2795-2802.

Mintzer, M. A. and E. E. Simanek (2008). "Nonviral Vectors for Gene Delivery." Chemical Reviews 109(2): 259-302.

Mizukoshi, Y., T. Shuto, *et al.* (2009). "Preparation of superparamagnetic magnetite nanoparticles by reverse precipitation method: Contribution of sonochemically generated oxidants." Ultrasonics Sonochemistry 16(4): 525-531.

Morales, M. A., T. K. Jain, *et al.* (2005). "Magnetic Studies of Iron Oxide Nanoparticles Coated with Oleic Acid and Pluronic (R) Block Copolymer." Journal of Applied Physics 97(10): 10Q905-10Q905-3.

Morones, J. R., J. L. Elechiguerra, *et al.* (2005). "The bactericidal effect of silver nanoparticles."Nanotechnology 16(10): 2346-2353.

Mu, W., J. M. Herrmann, *et al.* (1989). "Room-Temperature Photocatalytic Oxidation of Liquid Cyclohexane into Cyclohexanone over Neat and Modified TiO_2." Catalysis Letters 3(1): 73-84.

Murakami, K., S. Y. Chan, *et al.* (1986). "Protein-Kinase-C Activation by Cis-Fatty Acid in the Absence of Ca^{2+} and Phospholipids." Journal of Biological Chemistry 261(33): 5424-5429.

Murray, C. B., D. J. Norris, *et al.* (1993). "Synthesis and Characterization of Nearly Monodisperse Cde (E = S, Se, Te) Semiconductor Nanocrystallites." Journal of the American Chemical Society 115(19): 8706-8715.

Nakata, S., N. Kido, *et al.* (1996). "Chemisorption of proteins and their thiol derivatives onto gold surfaces: Characterization based on electrochemical nonlinearity." Biophysical Chemistry 62(1-3): 63-72.

Naumkin, A. V., A. Kraut-Vass, *et al.* (2006). NIST X-ray Photoelectron Spectroscopy Database, Measurement Services Division of the National Institute of Standards and Technology.

Nel, A. E., L. Maedler, *et al.* (2009). "Understanding biophysicochemical interactions at the nano-bio interface." Nature Materials 8(7): 543-557.

Nolf, F. A., J. S. Vandekerckhove, *et al.* (1977). "Sequence of A-protein of coliphage-MS2.1. Isolation of A-protein, determination of NH2-terminal and COOH-terminal sequences, isolation and amino-acid sequence of tryptic peptides." Journal of Biological Chemistry 252(21): 7752-7760.

Ofir, Y., B. Samanta, *et al.* (2008). "Polymer and biopolymer mediated self-assembly of gold nanoparticles." Chemical Society Reviews 37(9): 1814-1823.

Ohara, P. C., D. V. Leff, *et al.* (1995). "Crystallization of Opals from Polydisperse Nanoparticles." Physical Review Letters 75(19): 3466-3469.

Page, K., R. G. Palgrave, *et al.* (2007). "Titania and silver-titania composite films on glass-potent antimicrobial coatings." Journal of Materials Chemistry 17(1): 95-104.

Park, J., K. J. An, *et al.* (2004). "Ultra-large-scale syntheses of monodisperse nanocrystals." Nature Materials 3(12): 891-895.

Penrod, S. L., T. M. Olson, *et al.* (1996). "Deposition kinetics of two viruses in packed beds of quartz granular media." Langmuir 12(23): 5576-5587.

Pisanic, T. R., II, J. D. Blackwell, *et al.* (2007). "Nanotoxicity of iron oxide nanoparticle internalization in growing neurons." Biomaterials 28(16): 2572-2581.

Prakash, A., H. Zhu, *et al.* (2009). "Bilayers as Phase Transfer Agents for Nanocrystals Prepared in Nonpolar Solvents." Acs Nano 3(8): 2139-2146.

Qiao, R., C. Yang, *et al.* (2009). "Superparamagnetic iron oxide nanoparticles: from preparations to in vivo MRI applications." Journal of Materials Chemistry 19(35): 6274-6293.

Qin, J., S. Laurent, *et al.* (2007). "A high-performance magnetic resonance imaging T-2 contrast agent." Advanced Materials 19(14): 1874-1878.

Qu, H., D. Caruntu, *et al.* "Water-Dispersible Iron Oxide Magnetic Nanoparticles with Versatile Surface Functionalities." Langmuir 27(6): 2271-2278.

Rembaum, A. (1983). U. S. P. Specification. 4267234.

Rigaku-Corporation (2006). Particle/Pore Size Analysis Software Instruction Manual. Nanosolver, version 3.4. Woodlands, Rigaku-Corporation: Manual.

Roecker, C., M. Poetzl, *et al.* (2009). "A quantitative fluorescence study of protein monolayer formation on colloidal nanoparticles." Nature Nanotechnology 4(9): 577-580.

Sclafani, A., M. N. Mozzanega, *et al.* (1997). "Influence of silver deposits on the photocatalytic activity of titania." Journal of Catalysis 168(1): 117-120.

Sclafani, A., M. N. Mozzanega, *et al.* (1991). "Effect of Silver Deposits on the Photocatalytic Activity of Titanium-Dioxide Samples for the Dehydrogenation or Oxidation of 2-Propanol." Journal of Photochemistry and Photobiology a-Chemistry 59(2): 181-189.

Seery, M. K., R. George, *et al.* (2007). "Silver doped titanium dioxide nanomaterials for enhanced visible light photocatalysis." Journal of Photochemistry and Photobiology a-Chemistry 189(2-3): 258-263.

Shen, A. Q., B. Gleason, *et al.* (2002). "Fiber coating with surfactant solutions." Physics of Fluids 14(11): 4055-4068.

Shen, L. F., P. E. Laibinis, *et al.* (1999). "Bilayer surfactant stabilized magnetic fluids: Synthesis and interactions at interfaces." Langmuir 15(2): 447-453.

Shimoiizaka, J., K. Nakatsuka, *et al.* (1980). "Sink-Float Separators Using Permanent-Magnets and Water Based Magnetic Fluid." Ieee Transactions on Magnetics 16(2): 368-371.

Shukla, A., M. K. Patra, *et al.* "Preparation and Characterization of Biocompatible and Water-Dispersible Superparamagnetic Iron Oxide Nanoparticles (SPIONs)." Advanced Science Letters 3(2): 161-167.

Sobsey, M. D., T. Fuji, *et al.* (1988). "Inactivation of Hepatitis-a Virus and Model Viruses in Water by Free Chlorine and Monochloramine." Water Science and Technology 20(11-12): 385-391.

Sommer, R., W. Pribil, *et al.* (2001). "Inactivation of bacteriophages in water by means of non-ionizing (UV-253.7 nm) and ionizing (gamma) radiation: A comparative approach." Water Research 35(13): 3109-3116.

Sordo, C., R. Van Grieken, *et al.* (2010). "Solar photocatalytic disinfection with immobilised TiO2 at pilot-plant scale." Water Science and Technology 61(2): 507-512.

Springer, B. A. and S. G. Sligar (1987). "High-Level Expression of Sperm Whale Myoglobin in Escherichia-Coli. "Proceedings of the National Academy of Sciences of the United States of America 84(24): 8961-8965.

Srivastava, S., A. Verma, *et al.* (2005). "Controlled assembly of protein-nanoparticle composites through protein surface recognition." Advanced Materials 17(5): 617-+.

Stewart, S. and P. M. Fredericks (1999). "Surface-enhanced Raman spectroscopy of peptides and proteins adsorbed on an electrochemically prepared silver surface." Spectrochimica Acta Part a-Molecular and Biomolecular Spectroscopy 55(7-8): 1615-1640.

Sugimoto, T. and E. Matijevic (1980). "Formation of Uniform Spherical Magnetite Particles by Crystallization from Ferrous Hydroxide Gels." Journal of Colloid and Interface Science 74(1): 227-243.

Sun, S. H., H. Zeng, *et al.* (2004). "Monodisperse MFe_2O_4 (M = Fe, Co, Mn) nanoparticles." Journal of the American Chemical Society 126(1): 273-279.

Sun, Y. F. and J. J. Pignatello (1995). "Evidence for a Surface Dual Hole - Radical Mechanism in the Tio2 Photocatalytic Oxidation of 2,4-Dichlorophenaxyacetic Acid." Environmental Science & Technology 29(8): 2065-2072.

Sung-Suh, H. M., J. R. Choi, *et al.* (2004). "Comparison of Ag deposition effects on the photocatalytic activity of nanoparticulate TiO_2 under visible and UV light irradiation." Journal of Photochemistry and Photobiology a-Chemistry 163(1-2): 37-44.

Tanaka, T., R. Shimazu, *et al.* (2009). "Preparation of spherical and uniform-sized ferrite nanoparticles with diameters between 50 and 150 nm for biomedical applications." Journal of Magnetism and Magnetic Materials 321(10): 1417-1420.

Technologies, E. "Cdse/Zns Evitags, Type 1 and Type 2-MP MSDS V1.1. "Retrieved January, 2006, from http://www.evidenttech.com/assets/docs/MSDS/CdSe-ZnS-T1-T2-EviTags-MSDS-v2.pdf.

Teja, A. S. and P.-Y.Koh (2009). "Synthesis, properties, and applications of magnetic iron oxide nanoparticles." Progress in Crystal Growth and Characterization of Materials 55(1-2): 22-45.

Travert-Branger, N., F. Dubois, *et al.* (2008). "Oligomeric PEG-phospholipids for solubilization and stabilization of fluorescent nanocrystals in water." Langmuir 24(7): 3016-3019.

Tree, J. A., M. R. Adams, *et al.* (2003). "Chlorination of indicator bacteria and viruses in primary sewage effluent." Applied and Environmental Microbiology 69(4): 2038-2043.

Tung, W. S. and W. A. Daoud (2009). "New Approach Toward Nanosized Ferrous Ferric Oxide and $Fe_{(3)}O_4$-doped Titanium Dioxide Photocatalysts." Acs Applied Materials & Interfaces 1(11): 2453-2461.

Vamathevan, V., R. Amal, *et al.* (2002)."Photocatalytic oxidation of organics in water using pure and silver-modified titanium dioxide particles."Journal of Photochemistry and Photobiology A: Chemistry 148(1-3): 233-245.

Veiga, V., D. H. Ryan, *et al.* (2000). "Formation and characterization of superparamagnetic cross-linked high amylose starch." Carbohydrate Polymers 42(4): 353-357.

Verma, A., S. Srivastava, *et al.* (2005). "Modulation of the interparticle spacing and optical behavior of nanoparticle ensembles using a single protein spacer." Chemistry of Materials 17(25): 6317-6322.

Vossmeyer, T., S. W. Chung, *et al.* (1998). "Surprising superstructures: Rings." Advanced Materials 10(4): 351-353.

Wang, Z. and L. Ma (2009). "Gold nanoparticle probes." Coordination Chemistry Reviews 253(11-12): 1607-1618.

Watanabe, J., H. Ono, *et al.* (1985). "Thermotropic Polypeptides .2. Molecular Packing and Thermotropic Behavior of Poly(L-Glutamates) with Long Normal-Alkyl Side-Chains." Macromolecules 18(11): 2141-2148.

Watts, R. J., S. H. Kong, *et al.* (1995). "Photocatalytic Inactivation of Coliform Bacteria and Viruses in Secondary Waste-Water Effluent." Water Research 29(1): 95-100.

Wei, C., W. Y. Lin, *et al.* (1994). "Bactericidal Activity of TiO_2 Photocatalyst in Aqueous-Media - toward a Solar-Assisted Water Disinfection System." Environmental Science & Technology 28(5): 934-938.

Wei, X., Z. Wei, *et al.* (2011). "Highly water-soluble nanocrystal powders of magnetite and maghemite coated with gluconic acid: Preparation, structure characterization, and surface coordination." Journal of Colloid and Interface Science 354(1): 76-81.

Wong, M., L. Kumar, *et al.* (2009). "Evaluation of public health risks at recreational beaches in Lake Michigan via detection of enteric viruses and a human-specific bacteriological marker." Water Research 43(4): 1137-1149.

Woo, K. and J. W. Hong (2005). "Surface modification of hydrophobic iron oxide nanoparticles for clinical applications." Ieee Transactions on Magnetics 41(10): 4137-4139.

Wooding, A., M. Kilner, *et al.* (1991). "Studies of the Double Surfactant Layer Stabilization of Water-Based Magnetic Fluids." Journal of Colloid and Interface Science 144(1): 236-242.

Xiao, L., J. Li, *et al.* "Water-Soluble Superparamagnetic Magnetite Nanoparticles with Biocompatible Coating for Enhanced Magnetic Resonance Imaging." Acs Nano 5(8): 6315-6324.

Xie, R., K. Chen, *et al.* (2008). "InAs/InP/ZnSe Core/Shell/Shell Quantum Dots as Near-Infrared Emitters: Bright, Narrow-Band, Non-Cadmium Containing, and Biocompatible." Nano Research 1(6): 457-464.

Xin, B. F., L. Q. Jing, *et al.* (2005). "Effects of simultaneously doped and deposited ag on the photocatalytic activity and surface states of TiO_2." Journal of Physical Chemistry B 109(7): 2805-2809.

Yang, T., Z. Li, *et al.* (2007). "Synthesis, characterization, and self-assembly of protein lysozyme monolayer-stabilized gold nanoparticles." Langmuir 23(21): 10533-10538.

Yang, X., X. Zhang, *et al.* (2008)."High-Efficiency Loading and Controlled Release of Doxorubicin Hydrochloride on Graphene Oxide."The Journal of Physical Chemistry C 112(45): 17554-17558.

Yao, K. F., Z. Peng, *et al.* (2009). "Preparation and Photocatalytic Property of TiO_2-Fe_3O_4 Core-Shell Nanoparticles." Journal of Nanoscience and Nanotechnology 9(2): 1458-1461.

Yates, M. V., J. Malley, *et al.* (2006). "Effect of adenovirus resistance on UV disinfection requirements: A report on the state of adenovirus science." Journal American Water Works Association 98(6): 93-106.

Yavuz, C. T., J. T. Mayo, *et al.* (2006). "Low-field magnetic separation of monodisperse Fe_3O_4 nanocrystals." Science 314(5801): 964-967.

Yoder, J., V. Roberts, *et al.* (2008). "Surveillance for Waterborne Disease and Outbreaks Associated with Drinking Water and Water not Intended for Drinking --- United States, 2005--2006." Surveillance Summaries 57(SS09): 39-62.

Yoon, K. Y., C. Kotsmar, *et al.* (2011). "Stabilization of Superparamagnetic Iron Oxide Nanoclusters in Concentrated Brine with Cross-Linked Polymer Shells."Langmuir 27(17): 10962-10969.

You, C.-C., A. Chompoosor, *et al.* (2007). "The biomacromolecule-nanoparticle interface." Nano Today 2(3): 34-43.

Young, A. J. (2002). "Oleic Acid, Chemical Laboratory Information Profile." Journal of Chemical Education 79(1): 24.

Yu, S. and G. M. Chow (2004). "Carboxyl group ($-CO_2H$) functionalized ferrimagnetic iron oxide nanoparticles for potential bio-applications." Journal of Materials Chemistry 14(18): 2781-2786.

Yu, W. W., E. Chang, *et al.* (2007). "Forming biocompatible and nonaggregated nanocrystals in water using amphiphilic polymers." Journal of the American Chemical Society 129(10): 2871-2879.

Yu, W. W., E. Chang, *et al.* (2006). "Aqueous dispersion of monodisperse magnetic iron oxide nanocrystals through phase transfer."Nanotechnology 17(17): 4483-4487.

Yu, W. W., J. C. Falkner, *et al.* (2004). "Synthesis of monodisperse iron oxide nanocrystals by thermal decomposition of iron carboxylate salts." Chemical Communications(20): 2306-2307.

Yu, W. W. and X. G. Peng (2002). "Formation of high-quality CdS and other II-VI semiconductor nanocrystals in noncoordinating solvents: Tunable reactivity of monomers." Angewandte Chemie-International Edition 41(13): 2368-2371.

Yu, W. W., L. H. Qu, *et al.* (2003). "Experimental determination of the extinction coefficient of CdTe, CdSe, and CdS nanocrystals." Chemistry of Materials 15(14): 2854-2860.

Yu, W. W., Y. A. Wang, *et al.* (2003). "Formation and stability of size-, shape-, and structure-controlled CdTe nanocrystals: Ligand effects on monomers and nanocrystals." Chemistry of Materials 15(22): 4300-4308.

Zhang, D., O. Neumann, *et al.* (2009). "Gold Nanoparticles Can Induce the Formation of Protein-based Aggregates at Physiological pH." Nano Letters 9(2): 666-671.

Zhang, L., J. Xia, *et al.* (2010). "Functional Graphene Oxide as a Nanocarrier for Controlled Loading and Targeted Delivery of Mixed Anticancer Drugs." Small 6(4): 537-544.

Zhang, L. W., W. W. Yu, *et al.* (2008). "Biological interactions of quantum dot nanoparticles in skin and in human epidermal keratinocytes." Toxicology and Applied Pharmacology 228(2): 200-211.

Zhang, L. Z., J. C. Yu, *et al.* (2003). "Ambient light reduction strategy to synthesize silver nanoparticles and silver-coated TiO_2 with enhanced photocatalytic and bactericidal activities." Langmuir 19(24): 10372-10380.

APPENDIX 5: INTRADUCTAL DELIVERY OF NANO-THERAPUETICS AND IMAGING AGENTS

Intraductal delivery of nano-therapuetics and imaging agents

M. X. Pulikkathara
Chemistry Department, Rice University, 6100 Main Street
Houston, Texas 77005, USA
mpulikkathara@slb.com

E. Bryant
Chemistry Department, Rice University, 6100 Main Street
Houston, Texas 77005, USA
Elb4799@rice.edu

ABSTRACT

Intraductal approach is a relatively new research area and will be described in the following chapter. Breast cancer, from it's evolution of altered tight junctions to nanoparticle delivery of anticancer therapeutics via intraducts will be discussed and some aspects of nanocarriers will be broadly addressed.

INTRODUCTION

Breast cancer is only second to lung as the predominant type of cancer in adult women (Haley and Frenkel 2008). To understand how it functions, we must study the structure of the tumor and it's environment, and use the knowledge gained in the treatment. Tumors that can progress from anti-angiogenic (non-blood vessel forming state) to an angiogenic state (blood vessel forming state) after the tumor has reached a size of 2 mm^3 (Haley and Frenkel 2008; Danhier, Feron, *et al.* 2010), are able to form new vasculature from one that already exist, thereby providing a blood/energy supply to the tumor. Tumor blood vessels are identified by having an increased amount of

proliferating endothelial cells which have a pore size of 10-1000nm. (Danhier, Feron, *et al.* 2010) breasts have several ductal systems that emerge to the surface, where epithelial cells that line the ductal-lobular junctions, and is understood to be where tumors originate from, refer to the figure below. Biomarkers indicating cancer progression such as DLX2 in human breast cancer line MDA-MB-231 was studied by Morini et. al. (Morini, Astigiano *et al.* 2010) and was found to serve as definite prognastic markers, to identify these markers and their affiliation with tumors, we must understand how cancer cells spread.

Cancer can be spread into the body by directly seeding organ surfaces/body cavities, through the lymph system, or through hematogenous spread. Intraductal spread of breast carcinoma has been studied by Jing *et al.* (1999) and had found that intraductal spread had been involved in more cases with vascular invasion, and that the particular spread of intraductal carcinoma can lead to increased tumor volume, extend penetratingly into the breast, and form islands of carcinoma which can lead to reoccurance of breast disease.

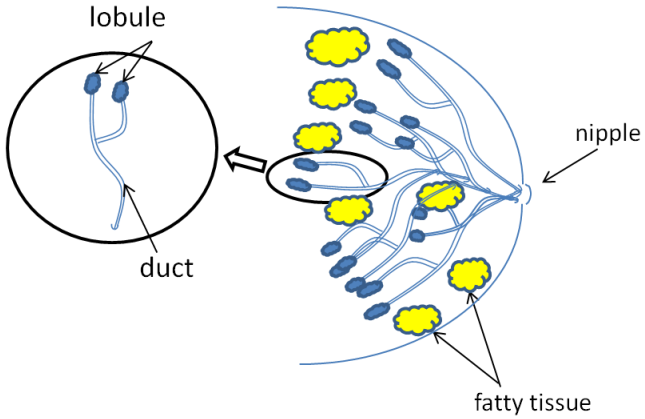

Figure 1. Depiction of breast with ducts/lobes.

Early intraductal research had involved nipple aspiration fluid (NAF) and abnormal cells were found through this method, however, long term studies had shown that this procedure had led to a risk of two to five times of developing cancer than those who did not offer any NAF. Yet NAF offers information on growth, development of tumors, and this had led to understanding biomarkers in breast fluid (King, Love *et al.* 2005). Ductal lavage, which uses a microcatheder, is able to obtain larger amount of cells from the ends of the mammary branches for various studies.

In studying the different types of cancerous tumors in the breast, it was found that apoptosis, cell death, occurs differently and more often in intraductal carcinoma when compared to infiltrating duct carcinoma and is related to an altered gene p53 expression (Harn, Shen *et al.* 1997). This has made the understanding of intraductal approach critical for breast cancer research.

Intraductal approach

Intraductal approach has been utilized in three areas, for study of potential prescreening for breast cancer biomarkers (King, Love *et al.* 2005); as a route to introduce and induce growth of intraductal lesions for research (Terada, Uchide *et al.* 1995), and as a route for intraductal injection of nanoparticle anti cancer agents (Murata, Kominisky *et al.* 2006). To understand these areas, it is important to note how the epithelial cells forming the structure of the intraducts themselves give rise to cancer implications.

TIGHT JUNCTIONS AND DUCTAL CARCINOMAS

The breasts' ducts and lobules are lined with barrier-forming epithelial cells that are composed of sheets which are assembled by cell-cell adhesion, otherwise known as tight junctions TJ (King, Love *et al.* 2005). The role of these TJ's can influence the beginning and progress of breast cancer. The TJ's have basically three types of proteins, integral membrane proteins, such as occludin; scaffolding proteins, such as zona occludens which are associated with MAGUK portion of scaffolding proteins and; signaling proteins, such as cingulin. Loss or gain of these proteins could lead to tumor growth/decrease.

These TJ's have various roles, for example, gate and fence function, in which the gate function controls the access of ions and solutes through epithelial sheets in a precise manner, allowing specificity of organs. TJ's also regulate adhesion and migration of cells, in a response to an injury for example. Another biological function of tight junctions is to regulate the polarity and differentiation of epithelial by overseeing the construction of the main polarity complexes. Any alteration of these biological roles for the tight junctions or imbalance of the proteins mentioned can lead to cancer progression.

INDUCE GROWTH OF INTRADUCTAL LESIONS FOR RESEARCH

Chemotherapeutics are commonly introduced via i.v. injections, but since more than 95% of breast cancers originate from the epithelial cells that construct the ductal system and gland lobules, this would be a more direct route of drug administration and sidestep the adverse systemic effects, in a study investigating ductal access for therapy, Murata, et. al. (2006), had used pegylated liposomal doxorubicin (PLD) and 4-hydroxytamoxifen in the treatment of breast cancer using rat N-methyl-N"-nitrosurea-

induced and spontaneous HER-2/neu transgenic mouse (neu-N) models of breast cancer. By using intraductal injection, the data had shown to have regression of present tumors with higher local and lower systemic effects of the drugs.

Ductal carcinomas in situ (DCIS) comprise 80% of noninvasive breast lesions. To understand the diversity of human noninvasive breast cancer, human in mouse (HIM) intraductal research was carried out by Behod et. al (2009). The advantages of their HIM model included closely mimicked how DCIS would grow in humans, and the growth and progression of cancer cells to finally invade the stroma was able to be studied. However, a disadvantage of this and other human models of noninvasive breast cancers, is that there may be artificial interaction with the cancer cells because of the compromised immune system.

NANOPARTICLES IN MEDICINE

INTRODUCTION

Nanoparticles which are particles of any composition and a few examples of nanoparticles that have served in research for cancer treatment/imaging are shown in the figure below.

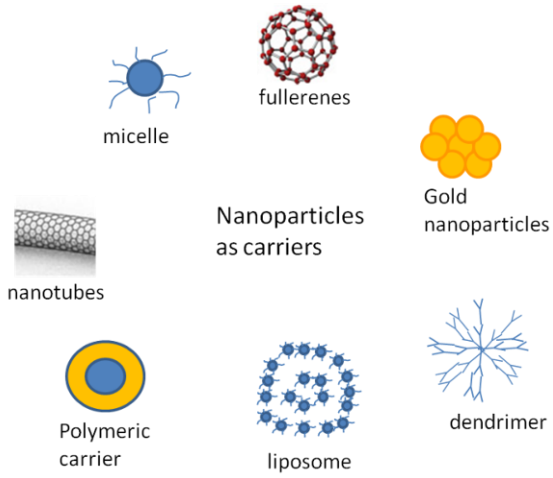

Figure 2. Examples of nanocarriers.

Nanoparticles (NP) can be delivered to the body in a passive or active process. Passive drug delivery involves transporting nanoparticles through leaky fenestrations into the tumor interstitium. The tumor intersitium consists of a collagen network and fluidic gel which has interstitial pressure high enough to deflect any inward gradient of molecules (Murata, Kominisky *et al.* 2006).

This pressure is higher in the tumor center than at the edges and considering particle size, configuration, hydrophobic/hydrophilicity, and electrical surface charge, and the fact that they lack a good draining lymphatic system, it would be difficult for microsized particles to enter. If it were able to do, it would have access and retention time in the interstitium, and this is referred to as enhanced permeability and retention (EPR) (Behbod, Kittrell *et al.* 2009).

Without adequate coating and targeting applied to the surface of these nanparticles, the NP would be tagged by opsonins which would make the NP easier to locate by the macrophages upon entry into the bloodstream. Recognition by the reticulo-

endothelial system (RES) would decrease time circulating in the blood stream, and reduce it's effectiveness against tumors. Once it is identified as a foreign object, the cells defenses come into play. Once the opsonization occurs, phagocytosis ensues in various steps. Adhesion and ingestion of the NP followed by phagosome formation and phagosolysosome formation.

Non-phagocytic pathways, include endocytosis, "cell drinking" involves a series of pathways as well, including macropinocytosis, clathrin-mediated endocytosis (CME), and caveolae-mediated endocytosis (CvME), this elimination and uptake of NP from the system is carefully described by Hillaireau et. al. (2009) and of characteristics of nanocarriers and their effectiveness in drug delivery (Hillaireau, Couvreur *et al.* 2009). Certain characteristics of the nanoparticles effect their ability to serve as nanocarriers of chemotherapeutics, such as size, surface coating, surface charge, and shape, which will be explained in the following.

SIZE RELATED BEHAVIOR

Various sizes of the nanoparticles have preferential absorption into different types of cells lines, and into elimination protocols as well. For example, NP smaller than 200 nm were found to by internalized via CME and larger NP were internalized via CvME. A few examples of nano particles are described below in Table 1.

Table 1. Size related preference (Hillaireau, Couvreur *et al.* 2009)

Nanocarrier	size	Preferential size absorption
Polystyrene	20-100nm	Hepa 1-6 hepatoma,HepG2 human hepatocyte cell lines
Polystyrene	20-600nm	KLN 205 squamous carcinoma cell line
Poly(lactic-co-glycoilc acid)	100nm	Caco-2 cell line of the gastrointestinal epithelium

SURFACE COATING OF NANOCARRIERS FOR CHEMOTHERAPEUTICS

There are a variety of nanocarriers used in nanomedicine research today. In order to make these nanocarriers effective, modification of their surfaces must achieved as to avoid the RES and their elimination from the system as described above. The surface of tumors have integrins which are transmembrane adhesion receptors which are involved with cell attachment, differentiation, migration and survival, of the family of integrins, the most critical has been $\alpha_v\beta_{3,}$ which has been studied on the surface of malignant breast tumors. This integrin has been shown to attach successively to a variety of proteins matrices such as vitronectin, fibrinogen, osteopntin, to name a few. This attachment has been through Arg-Gly-Asp (RGD) tripeptide sequence, which has been shown to decrease breast tumors (Murata, Kominisky *et al.* 2006).

The successful coating of nanoparticles with these appropriate ligands can then target and bind with the surface of these tumors and reduce their size by interrupting the activity of these $\alpha_v\beta_3$ integrins. A few examples of nanocarriers are shown in Table 1 below.

Table 2. Variety of nanocarriers (Chen 2010; Qiao, Wang *et al.* 2010)

Nanocarrier	Application potential
Polymeric nanoparticle	Paclitaxel loaded NP with galactosamine reduced liver tumors [< 1 micron]
Micelles	Hydrophilic shell can avoid uptake by RES and stay in circulation longer[< 100 nm], useful for transporting water soluable drugs in a hydrophobic central core.
Dendrimers	Multivalency is exploited to covalently attach various moieties, have shown specific binding.
Carbon nanotubes/Fullerenes	Carbon cages can be filled with molecules, the outer surface can be modified with appropriate ligands for attachment to receptors. Nanothermal therapy kill cancer cells via hyperthermia.
Nanofiber	Fibrous scaffold able to deliver sustained drug release to treat tumor
Liposomes	Lipid layers that can encapsulate water soluable drugs, can use polyethylene glycol or antibodies or ligands to escape RES and stay in system

Some NP studies have shown toxic effects by inhalation to lungs and result in local inflammation (Yacobi, Fazllolahi *et al.* 2011), these NP which are <100 nm could traverse the air-blood barrier and deposit in end organs such as liver, pancreas, kidney, spleen, and the myocardium. However, this could also be a potential method to treat cancers in those areas.

Current nanoparticles being used in treatment include liposomal drugs such as Doxil, DaunoXome, and Myocet and clinical trials involving pegylated liposomal doxorubicin for treatment of breast cancer are ongoing (Danhier, Feron *et al.* 2010).

NANOCARRIERS FOR IMAGING

Some NP can also be used for imaging of tumors. For example, quatum dots are inorganic fluorescent semiconductor materials that can have 10-50 atoms and have a range of 2-10nm. Their size and shape effect absorption and emission in a very

controlled manner. They have energy levels of 1-5 eV and can absorb high energy photons and can cause localized and targeted damage to surface tumors as seen in Yacobi et. al. (2011) work.

Another class of materials which have been studied by Serda et. al. (2010) were porous silicon multi stage particles. These particles have been surface modified with amino propyl tri ethoxy silane and filled with super paramagnetic iron oxide nanoparticles (SPION) as a secondary particle which has been shown to be useful in imaging.

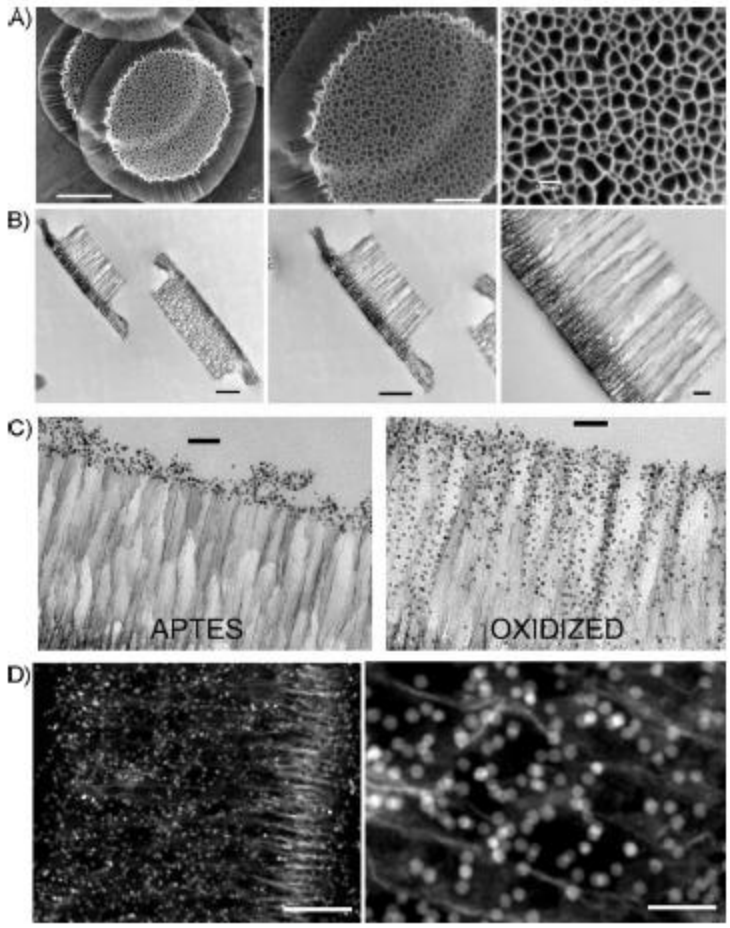

Figure 3. SPION loaded porous silicon particles (Serda, Mack *et al.* 2010).

Methotrexate (MTX) modified superparamagnetic nanoparticles were studied by Kohler et. al. (2005) in intracellular uptake into cancer cells, these NP were conjugated with folic acid which have been known to target tumors specifically. Various types of cancer cells including breast, ovarian, endometrial, have membranes in which folic receptors are overly expressed. Antibodies are bulky compared to the shorter chains of folic acid and can promote the internalization of NP. TEM images of Human breast cancer cells (MCF-7) had shown internalization of the MTX –nanoparticle conjugates proving this NP to be effective for imaging.

Metastases of breast cancer can also be detected by using SPIONs modified with lutening hormone releasing hormone (LHRH) and chronic gonadotropin , Leuschner et. al. (2006), showed that with use of the modified SPIONs in the MDA-MB-435S. luc cell line had a saturation of iron accumulation of 452.6 pg Fe/cell. Even the design of spacers can make a difference in the uptake of these SPION into breast cancer cells, Kumar et. al. (2007) found that the inclusion of glutaric acid in between SPION and lutening hormone releasing hormone had higher efficiency for intracellular uptake to breast cancer cells; this space increased intracellular iron uptake from 165 to 223.3 pg/cell, $p<0.001$.

NANOPARTICLES AND BREAST CANCER

The use of NP for imaging in breast cancer cells was discussed earlier, a study by Prabha et. al. (2004) had demonstrated sustained antiproliferated activity in breast cancer cells using poly(D,L-lactide-co-glycolide) PLGA nanoparticle-mediated wild type p53 and had shown a slow release of DNA from NP localized in the cells. The magnitude of the antiproliferative effect only increased with incubation time. Colombo et. al. (2010)

had reviewed various types of NP that were conjugated with anti human epidermal growth factor receptor 2 (HER2) (1) monoclonal antibody referred to trastuzumab.

Other types of nanoparticles, such as those studied by Gradishar et. al. (2005), composed of albumin bound Paclitaxel showed higher efficacy when compared to polethylated castor oil based Paclitaxel and had a lower incidence of grade 4 neutropenia. Binding concentration of modified nanoshells were examined by Fu et. al. (2008) and had shown that for anti-HER2/nanoshell bioconjugates, there were 800-1600 nanoshells bound per cell vs. 100 nanoshells bound per cell for anti-IgG/nanoshell bioconjugates.

SUMMARY

An overview of intraductal research was discussed. The roles of tight junctions was explored. Examples of nanoparticles and their application in therapeutic and diagnostic application was discussed.

REFERENCES

Behbod, F., F. S. Kittrell, H. LaMarca, D. Edwards, S. Kerbawy, J. C. Heestand, E. Young, P. Mukhopadhyay, H. Yeh, D. C. Allred, M. Hu, K. Polyak, J. Rosen, and D. Medina (2009). "An intraductal human-in-mouse transplantation model mimics the subtypes of ductal carcinoma in situ. Breast cancer research." 11(5): R66.

Chen, Z. (2010). "Small-molecule delivery by nanoparticles for anticancer therapy." Trends in Molecular Science. 16(12): 594-602.

Colombo, M., F Corsi, D. Foschi, E. Mazzantini, S. Mazzuccelli, C. Morasso, E. Occhipinti, L. Polito, D. Prosperi, S. Ronchi, and P. Verderio (2010). "HER2 targeting as a two-sided strategy for breast cancer diagnosis in nanomedical approaches." Pharmacological Research 52: 150-165.

Danhier, F., O. Feron, and V. Preat (2010). "To exploit the tumor microenvironment: Passive and active tumor targeting of nanocarriers for anto-cancer delivery." Journal of controlled release 148: 135-146.

Fu, K., J. Sun, L. Bickford, A. W. H. Lin, N. Halas, T. Yu, and R. Drezek (2008). "Measurement of immunotargeted plasmonic nanoparticles' cellular binding: a key factor in optimizing diagnostic efficacy." Nanotechnology 045103.

Gradishar, W. J., S. Tjulandin, N. Davidson, H. Shaw, N. Desai, P. Bhar, M. Hawkins, and J. O'Shaughnessy (2005). "Phase III trial of nanoparticle albumin-bound pacliaxel compared with polyethylated castor oil-based paclitaxel in women with breast cancer." Journal of clinical oncology 23(31): 7794-7803.

Haley, B., adn E. Frenkel (2008). "Nanoparticles for drug delivery in cancer treatment." Urologic oncology 26(1): 57-64.

Harn, H., K. L. Shen, K. C. Yueh, L. I. Ho, J. C. Yu, S. C. Chiu, and W. H. Lee (1997). "Apoptosis occurs more frequently in intraductal carcinoma than in filtering duct carcinoma of human breast cancer and correlates with altered p53 expression: detected by terminal-deoxynucleotidyl-transferase-mediated dUTP-FITC nick end labelling (TUNEL)." Histopathology (6): 534-539.

Hillaireau, H., and P. Couvreur (2009). "Nanocarriers' entry into the cell: relevance to drug delivery." Cell.Mol. Life Sci. 66:2873-2896.

Jing, X., K. Kakudo, M. Murakami, Y. Nakamura, M. Nakamura, T. Yokoi, Q. Yang, S. Oura, and T. Sakurai (1999). "Intraductal spread of invasive breast carcinoma has a positive correlation with c-erb B-2 overexpression and vascular invasion." Cancer 86:3: 439-448.

King, B., S. M. Love, S. Rochman, and J. A. Kim (2005). "The fourth international symposium on the intraductal approach to breast cancer, Santa Barbara, California, 10-13 March 2005." Breat Cancer Research 7(5).

Kohler, N., C. Sun, J. Wang, and M. Zhang (2005). "Methotrexate-modified superparamagnetic nanoparticles and their intracellualr uptake into human cancer cells." Langmuir 21: 8858-8864.

Kumar, C., C. Leuschner, M. Urbina, and J. Hormes (2007). "Glutaric acid as a spacer facilitates improved intracellular uptake of LHRH-SPION into human breast cancer cells." Internatioanl journal of nanomedicine 2(2): 175-179.

Leuschner, C., C. Kumar, W. Hansel, W. Soboyejo, J. Zhou, and J. Hormes (2006). "LHRH-conjugated mafnetic iron oxides nanoparticles for detection of breast cancer metastases." Breast cancer research and treatment 99: 163-176.

Morini, M., S. Astigiano, Y. Gitton, L. Emionite, V. Mirisola, G. Levi, and O. Barbieri (2010). "Mutually exclusive expression of DLX2 and DLX5/6 is associated with metastatic potential of the human breast cancer cell line MDA-MB-231." BMC Cancer 10(649).

Murata, S., S. Kominisky, M. Vali, Z. Zhang, E. Garrett-Mayer, D. Korz, D. Huso, S. D. Baker, J. Barber, and E. Jaffee (2006). "Ductal access for prevention and therapy of mammary tumors." Cancer Res 66(2): 638-645.

Prabha, S. and V. Labhasetwar (2004). "Nanoparticle-mediated wild type p53 gene delivery results in sustained antiproliferative activity in breast cancer cells." Molecular pharmaceutics 1(3): 211-219.

Qiao, W., B. Wang, Y. Wang, L. Yang, L. Zhang, and P. Shao (2010). "Cancer therapy based on nanomaterials and nanocarrier systems." Journal of nanomaterials. article ID 796303 ; 9 pages.

Serda, R., A. Mack, M. X. Pulikkathara, A. M. Zaske, C. Chiappini, J. R. Fakhoury, D. Webb, B. Godin, J. L. Conyers, X. W. Liu, J. A. Bankson, and M. Ferrari (2010). "Cellular association and assembly of multistage delivery system." Small 6(12): 1329-1340.

Terada, S., K. Uchide, N. Suzuki, and K. Akasofu (1995). "Nishida, E. Induction of ductal carinomas by intraductal administration of 7,12-dimethylbenz(a)anthracene in Wistar rats." Breast Cancer Research and Treatment 34: 35-43.

Yacobi, N. R., F. Fazllolahi, Y. H. Kim, A. Sipos, Z. Borok, K. Kim, and E. D. Crandall (2011). "Nanomaterial interactions with and trafficking cross the lung alveolar epithelial barrier: implications for helath effects of air-pollution particles." Air Qual Atmos Health 4:65-78.